

**UNIVERSIDADE FEDERAL DE SÃO CARLOS
CENTRO DE CIÊNCIAS EXATAS E DE TECNOLOGIA
PROGRAMA DE PÓS-GRADUAÇÃO EM CIÊNCIA E
ENGENHARIA DE MATERIAIS**

**DEVELOPMENT OF IONIC CONDUCTIVE CELLULOSE MAT BY
SOLUTION BLOW SPINNING AND LASER-INDUCED GRAPHENE
FROM PINEAPPLE NANOCELLULOSE FOR USE IN FLEXIBLE
ELECTRONIC DEVICES**

Pedro Ivo Cunha Claro

São Carlos-SP
2021

**UNIVERSIDADE FEDERAL DE SÃO CARLOS
CENTRO DE CIÊNCIAS EXATAS E DE TECNOLOGIA
PROGRAMA DE PÓS-GRADUAÇÃO EM CIÊNCIA E
ENGENHARIA DE MATERIAIS**

**DEVELOPMENT OF IONIC CONDUCTIVE CELLULOSE MAT BY
SOLUTION BLOW SPINNING AND LASER-INDUCED GRAPHENE
FROM PINEAPPLE NANOCELLULOSE FOR USE IN FLEXIBLE
ELECTRONIC DEVICES**

Pedro Ivo Cunha Claro

Doctoral thesis conducted under *cotutelle* agreement presented to the Graduate Program in Materials Science and Engineering as a partial requirement to obtain the title of DOCTOR IN MATERIALS SCIENCE AND ENGINEERING conferred by the Federal University of Sao Carlos (UFSCar) and the title of DOCTOR IN NANOTECHNOLOGIES AND NANOSCIENCE conferred by the Nova University Lisbon (UNL)

Adviser: Professor Luiz Henrique Capparelli Mattoso - UFSCar

Professor Elvira Maria Correia Fortunato - UNL

Co-adviser: Professor José Manoel Marconcini

Funding agency: CAPES/Embrapa – Code: 88882.157024/2017 01

ERC – Code: 787410 -DIGISMART

São Carlos-SP

2021

DEDICATION

To my mother, Giovanna, who has always encouraged me to study since I was little, and to my stepfather, Edival, who besides playing the role of my father, is a good friend.

VITAE

Bachelor of Science in Materials Engineering, Federal University of Sao Carlos (2014); Master of Science in Materials Engineering, Federal University of Sao Carlos (2017).



UNIVERSIDADE FEDERAL DE SÃO CARLOS

Centro de Ciências Exatas e de Tecnologia
Programa de Pós-Graduação em Ciência e Engenharia de Materiais

Folha de Aprovação

Defesa de Tese de Doutorado do candidato Pedro Ivo Cunha Claro, realizada em 26/02/2021.

Comissão Julgadora:

Prof. Dr. Luiz Henrique Capparelli Mattoso (EMBRAPA)

Prof. Dr. Leonardo Bresciani Canto (UFSCar)

Prof. Dr. Francys Kley Vieira Moreira (UFSCar)

Prof. Dr. Fernando Josepetti Fonseca (POLI)

Profa. Dra. Elvira Maria Correia Fortunato (UNL)

Prof. Dr. Luís Miguel Nunes Pereira (UNL)

Prof. Dr. Pedro Miguel Cândido Barquinha (UNL)

Profa. Dra. Verónica Cortés de Zea Bermudez (UTAD)

O presente trabalho foi realizado com apoio da Coordenação de Aperfeiçoamento de Pessoal de Nível Superior - Brasil (CAPES) - Código de Financiamento 001.

O Relatório de Defesa assinado pelos membros da Comissão Julgadora encontra-se arquivado junto ao Programa de Pós-Graduação em Ciência e Engenharia de Materiais.

ACKNOWLEDGEMENTS

First of all, I thank God - the basis of my faith.

I am especially grateful to my advisers in Brazil: professor Luiz Mattoso, for his greatness as a researcher and, at the same time, his simplicity as an advisor, for teaching and supporting me richly in all my dreams, and to professor José Marconcini, for his teachings since my internship period until the conclusion of this doctoral project, for showing me that it is impossible to conduct excellence research without consolidated knowledge of basic science.

I am also especially grateful to my adviser in Portugal, professor Elvira Fortunato, for fulfilling my dream of working with the researcher who revolutionized the electronic paper field in the world, together with professor Rodrigo Martins, who for me are examples of dedicated researchers of excellence. I extend my special thanks to professor Luís Pereira, for having me in his research team, for the weekly meetings that brought out brilliant ideas for the development of this project, and for the good times of fraternization with his group.

I would like to thank my friends and research colleagues in Brazil, who directly and indirectly supported this project with ideas or good times and were indispensable in my trajectory: Adriana Campos, Carol Corrêa, Vanessa Bolzan, Bruno Luchesi, Ana Paula, Jhony Silva, Alfredo Sena, Lina Bufalino, Luiz Silva, Kelvin Miranda, Rafaella Takehara, Paulinho, Kel, Thalita, Liliane, prof. Chu, Anderson, among others. I also would like to thank the technicians, researchers, and employees at Embrapa Instrumentation: Adriana Tomazi, Alice Raabe, Luiz Matteo, Marcelo Simões, Márcio, Maria Alice, Cauê, Paulo Lasso, Silviane, Viviane, among others.

I am grateful to PPGCEM for the excellent graduate studies program in materials science and engineering offered, to the graduate studies coordinator professor Leonardo Canto, and Marcelo, for being constantly helpful and to Geraldo, who was key to the drafting of the cotutelle agreement. I would like to thank the rector of USFCar and the SRinter, in particular Marcelo Pecenin, who was always very helpful in resolving doubts and issues related to the

cotutelle agreement. I thank DEMa and all the teachers and students at UFSCar who have supported me since my undergraduate course.

I would like to thank the thesis committee members for supporting me far beyond the traditional ideas and suggestions: professor Hernane Barud (for the countless cellulose acetate samples provided), professor Fernando Fonseca (for the many conversations and encouragement and support to visit Portugal), and professor Francys Kley (for the teaching internship).

I thank my Portuguese and Brazilian friends and colleagues who were, directly and indirectly, the foundation to the realization of this work in Portugal: Cristina Gaspar, Inês Cunha, Jenny Boane, Carolina Marques, Helder, Emanuel, Joana Figueira, Joana Pinto, Diana Gaspar, Paul Grey, Adriana, Neusmar, Rafaela Raupp, Marci, Lucas Roxo, Tiago Rio, among others, who I hope to see soon in Portugal.

I am also grateful to professor Pedro Barquinha (PDNN coordinator), the secretaries at CENIMAT (Valéria, Lúcia, among others) and CEMOP (Luís Milhano), and to the colleagues and technicians at CENIMAT who supported the development of this project (Daniela Gomes, Rita Branquinho, Jonas Deuermeier, Ana Pimentel, Alexandra, and Sónia Pereira).

My special thanks to Embrapa Instrumentation, for all the infrastructure, human and financial resources devoted to this work, and to CENIMAT and CEMOP, for providing the infrastructure to manufacture and characterize the electronic devices.

I thank the European Research Council (ERC) 787410 - DIGISMART and CAPES/Embrapa (grant no. 88882.157024/2017 01) for the scholarships, and the financial support provided by National Council for Scientific and Technological Development (CNPq) (grant no. 402287/2013-4), SisNANO/MCTI, Financier of Studies and Projects (FINEP), and the AgroNano research network of the Brazilian Agricultural Research Corporation (Embrapa).

This study was financed in part by the Coordenação de Aperfeiçoamento de Pessoal de Nível Superior - Brasil (CAPES) - Finance Code 001.

ABSTRACT

In the face of environmental issues and aiming at electronic devices of rapid production at low cost, this doctoral thesis proposed two new and innovative approaches to obtain substrates, dielectrics, and electrodes from a single biopolymer: cellulose. In a first moment, a simple approach to produce low-cost flexible ionic conductive cellulose mats (ICCMs) using solution blow spinning (SB-Spinning) is reported. The electrochemical properties of the ICCMs were adjusted through infiltration with alkali hydroxides (LiOH, NaOH, or KOH), which enabled of ICCMs application as dielectric and substrate in oxide-based field effect transistors (FETs) and pencil-drawn resistor-loaded inverters. The FETs showed good electrical performance under operating voltage <2.5 V, which was strictly associated with the type of alkali ion incorporated, presenting satisfactory performance for the ICCM infiltrated with K^+ ion. The inverters with K^+ ions also presented good dynamic performance, with a gain close to 2. Regarding the cellulose-based electrodes, a second innovative approach is reported to synthesize laser-induced graphene (LIG) structures from carboxymethyl cellulose (CMC)-based ink containing LIG obtained from cellulose nanocrystals (CNCs) extracted from pineapple leaf fibers (PALFs). To prove this concept, zinc oxide ultraviolet (ZnO UV) sensors were designed varying the amount of LIG from CNCs. Sensor obtained from LIG written directly on paper substrate were also performed. The ZnO UV sensors designed with CMC-based ink showed responsivity 40-fold higher than that of paper direct-written LIG, as well as excellent electrical performance under flexion. These findings may open new promising possibilities for low-consumption wearable electronics, allowing the use of concepts such as the "Internet of Things" and opening the possibility of generating 100% organic cellulose-produced electronic devices.

Keywords: solution blow spinning; electrolyte-gated circuitry; pineapple cellulose nanocrystals; laser-induced graphene; UV sensor; flexible electronics.

RESUMO

DESENVOLVIMENTO DE MANTA CONDUTORA IÔNICA VIA FIAÇÃO POR SOPRO EM SOLUÇÃO E GRAFENO VIA LASER, AMBOS A PARTIR DE CELULOSE, PARA TRANSISTORES, INVERSORES E SENSORES FLEXÍVEIS

Frente às questões ambientais e visando dispositivos eletrônicos de rápida produção e baixo custo, este projeto de pesquisa de doutorado propôs duas abordagens inovadoras para a obtenção de substratos, materiais dielétricos e eletrodos a partir de um único biopolímero: a celulose. Em um primeiro momento relata-se uma abordagem simples para produzir mantas condutoras iônicas de celulose (ICCM) flexíveis aplicando fiação por sopro em solução (SB-Spinning) seguido da infiltração com hidróxidos alcalinos (LiOH, NaOH ou KOH), permitindo sua aplicação como dielétrico e substrato em transistores e inversores com resistor desenhado a lápis. Os transistores exibiram um bom desempenho sob tensão de operação abaixo de 2,5 V, apresentando desempenho satisfatório para as mantas infiltradas com K^+ , além do inversor apresentar um ganho próximo de dois. Visando também eletrodos oriundos da celulose, este projeto relatou uma abordagem inovadora para sintetizar grafeno induzido por laser (LIG) a partir de tinta à base de carboximetilcelulose (CMC) contendo LIG obtido de nanocristais de celulose (CNCs) do abacaxi. Como prova de conceito, sensores de ZnO UV foram projetados variando a quantidade de LIG dos CNCs na tinta a base de CMC, assim como sensores obtidos por escrita direta de LIG em substrato de papel. Os sensores de ZnO UV flexíveis formulados com tinta apresentaram responsividade 40 vezes maior que os sensores contendo LIG direto do papel. Essas descobertas podem inaugurar uma nova Era na geração de eletrônicos vestíveis de baixo consumo, permitindo conceitos como "*Internet das Coisas*", e abrindo a possibilidade de dispositivos 100% orgânicos oriundos da celulose.

PALAVRAS-CHAVE: fiação por sopro em solução; circuitos eletrolíticos; nanocristais de celulose de abacaxi; grafeno induzido por laser; sensor de UV; eletrônica flexível.

PUBLICATIONS

- CLARO, P.I.C.C.; CUNHA, I.I.F.N.F.; PASCHOALIN, R.T.; GASPAR, D.F.P.; MIRANDA, K.W.E.; OLIVEIRA JR., O. N.; MARTINS, R.F.P.; PEREIRA, L.M.N.; MARCONCINI, J. M.; FORTUNATO, E. M. C.; MATTOSO, L.H.C. Ionic conductive cellulose mats by solution blow spinning as substrate and dielectric interstrate layer for flexible electronics. **ACS Applied Materials Interfaces**, v. 13, n. 22, p. 26237–26246, 2021.

CLARO, P.I.C.C.; CUNHA, I.I.F.N.F.; GASPAR, D.F.P.; MARCONCINI, J. M.; PEREIRA, L.M.N.; MARTINS, R.F.P.; MATTOSO, L.H.C; FORTUNATO, E. M. C. Cellulose mat by solution blow spinning as dielectric interstrate layer for flexible electronics. In: MATERIAIS 2019 - XIX CONGRESSO DA SOCIEDADE PORTUGUESA DE MATERIAIS AND X INTERNATIONAL SYMPOSIUM ON MATERIALS. Lisbon, Portugal. April, 2019

CLARO, P.I.C.C.; MARQUES, A.C.C.; CUNHA, I.I.F.N.F.; MARTINS, R.F.P.; PEREIRA, L.M.N.; MARCONCINI, J. M.; MATTOSO, L.H.C.; FORTUNATO, E. M. C. Tuning the electrical properties of cellulose nanocrystals through laser-induced graphitization for UV photodetectors. **ACS Applied Nano Materials**, 2021.

SUMMARY

	Pag.
FOLHA DE APROVAÇÃO.....	i
ACKNOWLEDGEMENTS.....	iii
ABSTRACT	v
RESUMO.....	vii
PUBLICATIONS	ix
SUMMARY	xi
LIST OF TABLES	xv
LIST OF FIGURES.....	xvii
SYMBOLS AND ABBREVIATIONS.....	xxiii
1 INTRODUCTION.....	1
2 LITERATURE REVIEW.....	3
2.1 Fundamental concepts.....	3
2.1.1 Lignocellulosic fibers, cellulose nanostructures, cellulose molecule, and cellulose derivatives	3
2.1.2 Pineapple leaf fibers (PALFs).....	7
2.1.3 Solution blow spinning (SB-Spinning)	8
2.1.4 Field effect transistor (FET) and inverters	9
2.1.5 Laser-assisted processing and laser-induced graphene (LIG).....	17
2.1.6 Zinc oxide ultraviolet (ZnO UV) sensors.....	20
2.2 State-of-the-art in cellulose as substrate and dielectric for flexible transistors and inverters	23
2.3 State-of-the-art of cellulose as a precursor of LIG electrode for flexible sensors.....	25
3 MATERIALS AND METHODS	29
3.1 ICCMs obtained by SB-Spinning as substrate and dielectric for flexible electronics	29
3.1.1 Materials	29
3.1.2 Preparation of CA-based mats by SB-Spinning	29
3.1.3 Characterization of CA-based mats	32
3.1.4 Preparation of ICCMs.....	33

3.1.5	Characterization of ICCMs	33
3.1.6	Fabrication of FETs and inverters	35
3.1.7	Characterization of the dielectric FETs and inverters	35
3.2	LIGE from pineapple CNCs and CMC-based ink for ZnO UV sensors.....	36
3.2.1	Materials	36
3.2.2	Delignification pretreatment of PALFs and CNCs extraction from PALFs .	36
3.2.3	Fabrication of ZnO UV sensors with interdigital LIGE	37
3.2.4	Characterization of ZnO UV sensors.....	39
4	RESULTS AND DISCUSSIONS	41
4.1	ICCM by SB-Spinning as substrate and dielectric “interstrate” layer for flexible electronics	41
4.1.1	Design and engineering of CA-based mats by SB-Spinning	41
4.1.2	Characterization of ICCMs	48
4.1.3	Electrical performance of ICCMs as dielectric and substrate in oxide-based FETs.....	55
4.1.4	Electrical performance of ICCMs as dielectric and substrate in pencil-drawn resistor-loaded inverters	60
4.2	LIGE from pineapple CNCs and CMC-based ink for flexible ZnO UV sensor	62
4.2.1	LIG obtained from pineapple CNCs	62
4.2.2	LIGE obtained from CMC-based ink containing LIG from PALFs.....	67
4.2.3	DLIGE on tracing paper surface.....	73
4.2.4	Electrical performance of ZnO UV sensors	75
5	CONCLUSIONS.....	81
5.1	ICCM by SB-Spinning as substrate and dielectric “interstrate” layer for flexible electronics	81
5.2	LIGE from pineapple CNCs and CMC-based ink for flexible ZnO UV sensor	81
6	SUGGESTIONS FOR FUTURE STUDIES	83
7	BIBLIOGRAPHIC REFERENCES.....	85
	APPENDIX A.....	107

APPENDIX B..... 109

LIST OF TABLES

	Pag.
Table 3.1 - Boiling point and vapor pressure of solvents and Hansen solubility parameters of solvents and CA	30
Table 3.2 - Detailed information of the prepared samples, and respective nomenclature depending of CA and PEO composition as well as SB-Spinning parameters	30
Table 4.1 - Type of CA-based sample formed after SB-Spinning and the respective CA-PEO fiber diameter with PEO mass variation.....	42
Table 4.2 - Detailed information on the thickness, R and R_o of each ICCM	54
Table 4.3 - Electrical parameters of GIZO FETs fabricated on distinct ICCMs applied as “interstrate” layer. The values show the mean and respective standard error of the mean obtained from ten devices.	57

LIST OF FIGURES

	Pag.
Figure 2.1 - (a) Structure of lignocellulosic fibers that compose the PALFs; (b) Chemical structure of cellulose. Images adapted from Correio da Amazônia [25]; Postek et al. [26], and Butchosa Robles [27].	3
Figure 2.2 - Main cellulose functionalizing reactions: (a) Cellulose acetylation to obtain CA; (b) Cellulose oxidation to obtain CMC. Reprinted with permission from El Barkany, S. et al. [47] and Isogai A. et al. [45].	6
Figure 2.3 - Illustrative image of the pineapple curaua cultivar with emphasis on the fruit and crown involved in PALFs. Reprinted from Correio da Amazônia [25].	8
Figure 2.4 - Illustration of the solution blow spinning (SB-Spinning) system. Reprinted with permission from Oliveira et al. [58] and Medeiros et al. [59].	8
Figure 2.5 - Schematic representation of the different types of transistors.	10
Figure 2.6 - (a) Schematic representation of a NMOS FET; (b) Symbolic representation of a NMOS in a circuit. Adapted from Ferreira [64].	11
Figure 2.7 - Representation of the three operating regions of a FET in relation to (a) drain current variation (I_D) as a function of drain and source voltage (V_{DS}) and in relation to (b) drain current variation (I_D) as a function of gate and source voltage (V_{GS}). Adapted from Ferreira [64].	12
Figure 2.8 - Schematic representation of a FET model in the triode mode. Adapted from Ferreira [64].	13
Figure 2.9 - Schematic representation of a FET model in the saturation mode. Adapted from Ferreira [64].	14
Figure 2.10 - (a) Schematic representation of a FET with paper as substrate and gate dielectric; (b) the first paper FET using oxide as semiconducting material; (c) CMOS on paper. Adapted with permission from Gaspar et al. [72], Fortunato et al. [74] and Martins et al. [77].	15
Figure 2.11 - (a) Schematic representation of EDL formation on cellulose fibers; (b) capacitance and phase angle as a function of the frequency applied on paper and the respective polarization regimes that occur on cellulose fibers. Reprinted with permission from Gaspar et al. [73].	16

Figure 2.12 - Inverter models. (a) Image of a CMOS on paper with a schematic representation of the inverter circuit. (b) Resistor-loaded inverter using a poly(3,4-ethylenedioxythiophene) polystyrene sulfonate (PEDOT:PSS) gate transistor with a schematic representation of the inverter circuit highlighted V_{OUT} vs. V_{IN} curve and V_{OUT} and V_{IN} as a function of time at 1 kHz. Reprinted with permission from Martins et al. [77] and Cho et al. [78].	17
Figure 2.13 - Schematic representation of a CO ₂ laser with highly coherent infrared generation and specific wavelength. Reprinted from Photonics Marketplace [92].	18
Figure 2.14 - Schematic representation of LIG synthesis on PI substrate. Reproduced with permission [96]. Copyright 2014, Macmillan Publishers Limited.	19
Figure 2.15 - One of the possible formation mechanisms of the graphitic aromatic chain from the cellulose molecule. Reprinted with permission from [105]. Copyright 2018 American Chemical Society.	20
Figure 2.16 - Schematic representation of the photodetection process of ZnO under UV radiation. Reprinted with permission from Jacobs et al. [108].	21
Figure 2.17 – (a) Schematic representation of a ZnO UV sensor production. (b) ZnO UV sensor on paper under UV radiation. (c) ZnO UV sensor responsivity under UV on/off radiation by ZnO nanostructures obtained from microwave and oven. Reprinted with permission from Pimentel et al. [114]. Copyright 2014. American Chemical Society.	23
Figure 3.1 - Hansen parameters describing the CA solubility range in formic and acetic acids.	32
Figure 3.2 – Schematic illustration about fabrication of FETs on ICCMs.	35
Figure 3.3 - Overview of the new approach proposed to obtain interdigital LIGE from pineapple CNCs and CMC-based ink by varying the laser focus, laser power and tip speed parameters.	38
Figure 4.1 - SEM micrographs evaluating the effect of PEO on CA fiber formation and flow rate during the SB-Spinning process: (a) Neat CA_3.5; (b) Neat CA_7.0; (c) Neat CA_10.0; (d) CA_PEO 0.04_3.5; (e) CA_PEO 0.04_7.0; (f) CA_PEO 0.04_10.0; (g) CA_PEO 0.08_3.5; (h) CA_PEO 0.08_7.0; (i)	

CA_PEO 0.08_10.0; (j) CA_PEO 0.24_3.5; (k) CA_PEO 0.24_7.0; (l) CA_PEO 0.24_10.0; (m) CA_PEO 0.40_3.5; (n) CA_PEO 0.40_7.0; and (o) CA_PEO 0.40_10.0.	41
Figure 4.2 - a) Schematic representation of the SB-Spinning technique. b) SEM image of CA-PEO fibers. c) Possible interactions between CA and PEO during fiber formation, whose strength may vary according to spin hypotheses.	43
Figure 4.3 - FTIR spectra for PEO groups and CA groups that interact with PEO: (a) C-O-C from D-glucopyranose ring; (b) C-O-C from glycosidic bond; (c) C-O-C from acetate group; (d) C=O from acetate group; (e) arrangement of the groups in the cellobiose monomer.	45
Figure 4.4 - Rheological diagrams of CA and CA_PEO solutions: (a) storage modulus (G')/loss modulus (G''); (b) complex viscosity (η^*). Rheological diagrams of PEO and solvents: (c) G'/G'' ; (d) η^*	46
Figure 4.5 - Micrographs of pure PEO spun: (a) PEO 0.24_3.4; (b) PEO 0.24_7.0; (c) PEO 0.24_10.0; (d) PEO 0.40_3.5; (e) PEO 0.40_7.0; and (f) PEO 0.40_10.0.	47
Figure 4.6 - FTIR spectra of CA-PEO mat before and after deacetylation using LiOH, KOH, and NaOH.	48
Figure 4.7 - TGA and derivative thermal gravimetry (DTG) of the CA-PEO mat before the deacetylation process and of the ICCMs after deacetylation using LiOH, KOH, and NaOH.	49
Figure 4.8 - XRD diagrams of CA-PEO mat before and after deacetylation using LiOH, KOH, and NaOH in ethanol solution.	50
Figure 4.9 - SEM micrographs of CA-PEO fibers before and after water immersion: (a) CA_PEO 0.24_before; (b) CA_PEO 0.24_after; (c) CA_PEO 0.40_before; (d) CA_PEO 0.40_after.	51
Figure 4.10 - Influence of the alkali hydroxides on the surface properties of the ICCMs: (a) SEM images of (a) LiOH_mat, (d) NaOH_mat, and (g) KOH_mat. (b) XPS of LiOH_mat. EDS mapping, where purple is carbon, blue is oxygen, and yellow is the metallic ions of (e) NaOH_mat and (h) KOH_mat. 3D profile for (c) LiOH_mat, (f) NaOH_mat, and (i) KOH_mat with color scale bar roughness intensity.	52

Figure 4.11 - (a) Schematic representation of the electrochemical cell with the ICCM. (b) Capacitance and phase angle vs. frequency for the LiOH, NaOH and KOH cellulose mats and their respective (c) Nyquist plots (inset: ionic conductivity for each ICCM). (d) Cyclic voltammetry (CV) measurements of the LiOH, NaOH and KOH cellulose mats from -3 to 3 V at 400 mV/s.	53
Figure 4.12 - (a) Optical photomicrograph of a transistor. ICCM as "interstrate" layer in a FET: (b) photograph and (c) schematic illustration. (d) Influence of salt ions on cyclic transfer characteristic curves of the FETs, where solid and dashed lines correspond to drain (I_{DS}) and leakage (I_{GS}) currents, respectively. The output curves with purple arrows represent the sweep direction for each ionic salt: (e) LiOH; (f) NaOH, and (g) KOH.....	55
Figure 4.13 - Influence of ICCM in- and out-plane bending radius on the cyclic transfer characteristic curves of FETs, where solid and dashed lines correspond to drain (I_{DS}) and leakage (I_{GS}) currents, respectively: (a) 45 mm, (b) 25 mm, and (c) 15 mm.	59
Figure 4.14 - Influence of ICCM in- and out-plane bending radius on the electrical parameters of the GIZO FETs: (a) $I_{on/off}$ and μ_{Sat} and (b) V_{ON} , S_S and g_m	59
Figure 4.15 - IZO-covered ICCM: (a) flat mode and (b) bending mat at 15 mm radius with IZO cracks indicated by white circles.	60
Figure 4.16 - (a) Photograph of ICCM as dielectric and substrate in pencil-drawn resistor-loaded inverters. (b) Schematic representation and photograph of KOH_mat as "interstrate" layer in an inverter. (c) Voltage transfer curve of the inverter on KOH_mat with a schematic representation of the circuit. Dynamic electrical characterization of the inverter on KOH_mat at 0.2 Hz using two resistances: (d) 1.5 M Ω and (e) 600 k Ω	61
Figure 4.17 - LIG obtained from pineapple CNC tablet. (a) Photograph of CNC tablet before laser passing and photographs of several LIG on CNC tablet, varying laser focus, laser power, and tip speed. (b) CNC "whiskers" before laser passing and circular LIG nanoparticles after laser passing.	63
Figure 4.18 - Raman spectra of LIG synthesized from CNC tablet, varying laser focus, tip speed (S), and laser power (P).	64

- Figure 4.19 - (a) I_G/I_D and I_{2D}/I_G ratios with laser focus (\square/\square +1.1 mm, \triangle/\triangle at focus, \bigcirc -1.1 mm) (\star/\star +1.1 mm), laser speed, and laser power. (b) FWHM values for the G band in relation to with laser focus (\square +1.1 mm, \triangle at focus, \bigcirc -1.1 mm) (\star +1.1 mm), laser speed, and laser power. 65
- Figure 4.20 - LIG obtained from pineapple CNC tablet. Sheet resistance of LIG as a function of (a) tip speed and laser focus at constant laser power, and (b) laser power at constant laser focus and tip speed..... 66
- Figure 4.21 - LIGE synthesized from CMC-based ink containing LIG from CNC. (a) Photographs of LIG_0, LIG_0.6 and LIG_1.2 before and after laser passing, varying laser focus, tip speed, and laser power. (b) Photomicrographs of LIG_0, LIG_0.6 and LIG_1.2 before and after laser passing (white scale bar of 100 μm). 68
- Figure 4.22 - LIGE synthesized from CMC-based ink containing LIG from CNC. Raman spectra of LIGE, varying laser focus, tip speed (S) and laser power (P), from the following LIG compositions: (a) LIG_0, (b) LIG_0.6, and (c) LIG_1.2. 69
- Figure 4.23 – I_G/I_D and I_{2D}/I_G ratios with laser focus (\square/\square +1.1 mm, \triangle/\triangle at focus, \bigcirc/\bigcirc -1.1 mm) (\star/\star +1.1 mm), laser speed, and laser power from the following LIG compositions: (a) LIG_0; (b) LIG_0.6 and (c) LIG_1.2. FWHM values for the G band in relation to laser focus (\square +1.1 mm, \triangle at focus, \bigcirc -1.1 mm) (\star +1.1 mm), laser speed, and laser power from the following LIG composition: (d) LIG_0; (e) LIG_0.6 and (f) LIG_1.2. 70
- Figure 4.24 - Sheet resistance of LIGE as a function of tip speed and laser focus at constant laser power: (a) LIG_0, (b) LIG_0.6, and (c) LIG_1.2. Sheet resistance as a function of laser power at constant laser focus and tip speed: (d) LIG_0, (e) LIG_0.6, and (f) LIG_1.2. 71
- Figure 4.25 - LIG on tracing paper surface: (a) paper sheet resistance before laser passing and DLIGE sheet resistance as a function of the number of laser passes at 2.4 W laser power, 5.8 cm/s tip speed, and +1.1 mm defocus. The photographs highlight the DLIGE squares drawn from the first (Paper_P1) and second (Paper_P2) laser passes; (b) Raman spectra of DLIGE from each laser

pass; and (c) I_G/I_D and I_{2D}/I_G ratios and FWHM values of the G band in relation to the laser passes.	73
Figure 4.26 - Photograph of the DLIGE squares according to the number of laser passes, showing the partial destruction of the paper substrate after the third laser pass.	74
Figure 4.27 - Photomicrographs of oxidized tracing paper microstructure before and after laser incidence, varying the number of laser passes (15 μm white bar scale).....	74
Figure 4.28 - Photographs of the ZnO UV sensors: (a) LIGE and (b) DLIGE (2 cm white bar scale). Photocurrent curve responses during ON/OFF UV radiation of the ZnO UV sensors: (c) LIGE_0.6, LIGE_1.2, and (d) DLIGE highlighted in zoom on the curve.....	76
Figure 4.29 – Cross-sectional photomicrography of LIG/tracing paper interface of (a) LIGE and (b) DLIGE (20 μm white bar scale). LIG gap of (c) LIGE and (d) DLIGE (5 mm black bars scale).....	77
Figure 4.30 - Photographs of the CMC ZnO UV sensors with LIGE under (a) outward (OUT) and (b) inward (IN) bending tests (2 cm black bar scale). Influence of the in- and out-plane bending radii on the electrical performance of ZnO UV sensors: (a) LIGE_0.6 and (b) LIGE_1.2.	79
Figure A.1 - Dynamic response of the ICCM inverter, varying the frequency and resistance: (a) $f = 0.1 \text{ Hz} / R = 1.5 \text{ M}\Omega$; (b) $f = 0.1 \text{ Hz} / R = 600 \text{ k}\Omega$; (c) $f = 0.5 \text{ Hz} / R = 1.5 \text{ M}\Omega$; (d) $f = 0.5 \text{ Hz} / R = 600 \text{ k}\Omega$; (e) $f = 1.0 \text{ Hz} / R = 1.5 \text{ M}\Omega$; (f) $f = 1.0 \text{ Hz} / R = 600 \text{ k}\Omega$; (g) $f = 2.0 \text{ Hz} / R = 1.5 \text{ M}\Omega$; (h) $f = 2.0 \text{ Hz} / R = 600 \text{ k}\Omega$; (i) $f = 3.0 \text{ Hz} / R = 1.5 \text{ M}\Omega$ and (j) $f = 3.0 \text{ Hz} / R = 600 \text{ k}\Omega$	107
Figure B.1 - Photomicrographs of CMC-based ink microstructure formulated with LIG from CNC (LIG_0.6 and LIG_1.2) before and after laser passing, varying laser focus at 8.2 cm/s laser speed and 2.4 W laser power (white scale bar of 15 μm).	109

SYMBOLS AND ABBREVIATIONS

NH₃ - ammonia

I_a - amorphous intensity at 2θ=16° for cellulose II.

ATR - attenuated total reflectance

V_{ON} - activation voltage

BJT - bipolar junction transistor

B - body

C - capacitance

(C₆H₁₀O₅)_n - cellulose

CA - cellulose acetate

CI - crystallinity index

CMC - carboxymethyl cellulose

CMF - cellulose microfibril

CNC - cellulose nanocrystal

CNF - cellulose nanofibril

L - channel length

CMOS - complementary metal-oxide semiconductor

W - conducting channel thickness

V_{DD} - constant supply voltage

I_{ON/OFF} - current modulation

CV - cyclic voltammetry

DLIGE - direct-written laser-induced graphene electrodes

DMAc - dimethyl acetamide

DTG - derivative thermal gravimetry

D - drain

I_D - drain current

V_{DS} - drain-source voltage

EDL - electrical double layer

EGT - electrolyte-gated transistor

R - electrical resistance

EIS - electrochemical impedance spectroscopy

C_e - entanglement concentration

K - factor related to surface mobility
FET - field effect transistor
FTIR - Fourier transform infrared spectroscopy
FWHM - full width at half maximum
G – gate
 V_{GS} - gate-source voltage
HCl - hydrochloric acid
OH - hydroxyl groups
 H_2O_2 - hydrogen peroxide
GIZO - gallium-indium-zinc oxide
IZO - indium-zinc oxide
IR - infrared spectra
S2- internal secondary wall
IoT - Internet-of-Things
 V_{IN} - input voltage
ICCM - ionic conductive cellulose mat
JFET - junction field effect transistor
LIG - laser-induced graphene
LIGE - laser-induced graphene electrodes
LiCl - lithium chloride
LiOH - lithium hydroxide
 G'' - loss modulus
 R_L - load resistance
 I_{dark} - magnitude of the dark current
 I_{ph} - magnitude of the photocurrent
R - mass electrical resistance
 M_v - molecular weight volumetric
 M_n - molecular weight numeric
MOSFET - metal-oxide semiconductor field effect transistor
nNMMO - n-methyl-morpholine N-oxide
NMOS - N type metal-oxide semiconductor
 T_{onset} - onset temperature of thermal degradation

Cox - oxide capacitance
V_{OUT} - output voltage
Paper-e - paper electronic
PALF - pineapple leaf fiber
PLA - poly(lactic acid)
PCL - polycaprolactone
PEO - poly(ethylene oxide)
PEI - polyetherimide
PESU - polyethersulfone
PI- polyimide
PET-co-PEI - poly(ethylene terephthalate-co-ethylene isophthalate)
PEDOT:PSS - poly(3,4-ethylenedioxythiophene) polystyrene sulfonate
PMOS - P type metal-oxide semiconductor
KOH - potassium hydroxide
P_{UV} - power of the UV source
I_D/I_G - ratio of D and G graphene bands obtained from Raman spectra
I_{2D}/I_G - ratio of 2D and G graphene bands obtained from Raman spectra
R_{res} - responsivity
RH - relative humidity
Si - silicon
SiO₂ - silicon dioxide
RMS - smallest root mean square
H₂SO₄ - sulfuric acid
SB-Spinning - solution blow spinning
NaBr - sodium bromide
SEM-EDS - scanning electron microscopy-energy dispersive X-ray spectroscopy
NaClO - sodium hypochlorite
NaOH - sodium hydroxide
S1- secondary wall
S - source

A - surface area of each aluminum electrode deposited on the cellulose mat

S_s - subthreshold slope

G' - storage modulus

l - thickness of the cellulose mat

I_t - total intensity at the crystalline peak (020) for cellulose

TEM - transmission electron microscopy

g_m - transconductance

TEMPO - 2,2,6,6-tetramethylpiperidine-1-oxyl

TGA - termogravimetric

S3 - tertiary wall

UV - ultraviolet

V_t - voltage threshold

H₂O - water

XRD - X-ray diffraction

XPS - X-ray photoelectron spectroscopy

ZnO - zinc oxide

η^* - complex viscosity

σ - ionic conductivity

l_β - monoclinic

μ_{Sat} - saturation mobility

μ_n - surface mobility

l_α - triclinic

1 INTRODUCTION

In recent years, there has been great interest in the research and development of polysaccharide-based materials because they originate from renewable sources, are biodegradable and abundantly present in nature, and have low extraction costs. In addition, polysaccharides show properties of scientific and technological interest and can be easily functionalized for different applications [1,2]. Cellulose, starch and chitin are main examples of polysaccharides. Cellulose stands out among all polysaccharides because it is the most abundant biopolymer in the Earth's crust and the cheapest substrate used in the daily life of humans [3].

In the past few decades, cellulose has been applied in several products through the use of nanotechnology [4–6], and more recently it has been used to manufacture low-cost, biocompatible, flexible and environment-friendly electronic devices and systems, thus opening an unprecedented New Era in organic electronics [7]. Paper electronic (paper-e) development is driven by the environmental problems cause by electronic waste (e-waste) [8]. However, the high performance of cellulose-based electronic devices has a demand for smoother and defect-free surfaces, which can be achieved with the use of nanostructures such as cellulose nanocrystals (CNCs) [9–11]. CNCs are extracted from lignocellulosic fibers through time-consuming chemical routes using acids and bases as reagents, which can make the process long and not cost-effective [12]. In addition, formation of nanopaper substrates also contributes to increase the process duration [13].

It is worth mentioning that, even though cellulose is used in several areas, ranging from simple to highly technological applications, many sources of cellulose are still little explored commercially, such as pineapple leaf fibers (PALFs), which exhibit unique characteristics [14]. PALFs originate from the sixth largest fruit production in the world and are composed mostly of cellulose [15]. Cellulose nanostructures can be easily extracted from PALFs using smaller amounts of chemical reagents compared with other vegetable fibers [15–17]. In addition, PALFs present several application potentials, such as in the medical field [18]. However, this rich cellulosic source is still a by-product or

even a residue in certain locations, with PALFs being discarded or even burned after pineapple harvesting [19].

Aiming at electronic devices that are nearly totally organic, sustainable, and of rapid production at low cost in the face of the issues presented, this doctoral thesis proposed two new and innovative approaches to obtain substrates, dielectric, and electrodes from a single biopolymer: cellulose. In a first approach, cellulose acetate fibers were obtained using the solution blow spinning (SB-Spinning) technique, which is a simple and inexpensive approach for producing polymeric micro- and nanofibers. The acetate fibers were deacetylated, forming a submicro-structured ionic conductive cellulose mat (ICCM) used as a substrate and dielectric in transistors and inverters. In the second approach, laser-induced graphene (LIG) structures were obtained from CNCs extracted from PALFs and in carboxymethyl cellulose (CMC) inks, which were used as electrodes in zinc oxide ultraviolet (ZnO UV) sensors. Therefore, this doctoral thesis advocates two innovative hypotheses to reduce the cost production of substrates, dielectric and electrodes. In addition to revolutionizing the production of graphene from by-products/residues from agricultural pineapple production.

2 LITERATURE REVIEW

2.1 Fundamental concepts

2.1.1 Lignocellulosic fibers, cellulose nanostructures, cellulose molecule, and cellulose derivatives

Lignocellulosic fibers compose the cell walls of tree stems as well as the leaf structure of several plants, such as pineapple leaf fibers (PALFs) [20,21]. Lignocellulosic fibers are a rich source of cellulose, hemicelluloses and lignin, in addition to presenting a small amount of grease and fat, in which cellulose represents between 40 and 50% of plant dry mass and can reach 90% in the case of cotton [22,23]. Lignocellulosic fibers are used as raw material to produce various types of paper with numerous applications, and these substrates have been the most widely used by humans for thousands of years [7,24].

Figure 2.1 shows the structure of lignocellulosic fibers and how cellulose fibers are arranged in their structures, as well as the mechanical and chemical routes for obtaining cellulose nanostructures, together with the chemical structure of the polymeric cellulose chain.

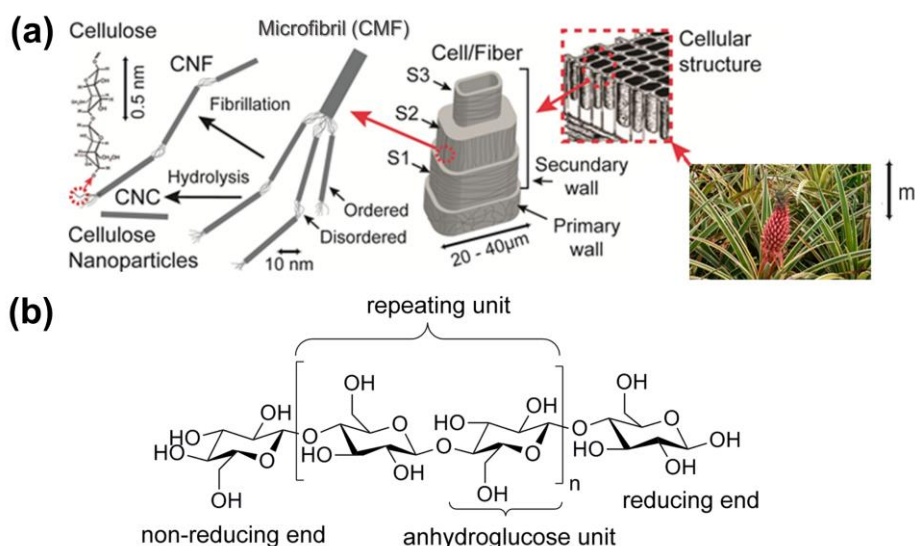


Figure 2.1 - (a) Structure of lignocellulosic fibers that compose the PALFs; (b) Chemical structure of cellulose. Images adapted from Correio da Amazônia [25]; Postek et al. [26], and Butchosa Robles [27].

Physically, lignocellulosic fibers are composed of a primary wall, an external secondary wall (S1), an internal secondary wall (S2), a tertiary wall (S3), and a lumen [1,22]. The S1, S2 and S3 walls are differentiated by the orientation of the cellulose microfibrils (CMFs) in relation to the fiber axis. This orientation is known as microfibrillar angle, which is directly related to the mechanical properties of the lignocellulosic fibers [22,28]. Cellulose nanostructures are obtained through two main routes from CMFs [29,30]: (1) mechanical shear of the CMFs, generating cellulose nanofibrils (CNFs) that present both amorphous and crystalline regions along their structure and a spaghetti-shaped arrangement of nanofibrils with a diameter ranging from 5 to 60 nm and length reach over 100 μm ; (2) acid hydrolysis of the amorphous region of the CMFs, generating cellulose nanocrystals (CNCs) that can reach over 90% crystallinity and present a whisker-like shape with diameter and length ranging from 5 to 70 nm and 100 to 300 nm, respectively, as illustrated in Figure 2.1a.

Lignin is one of the main components of lignocellulosic fibers, and is distributed in greater amounts on the secondary wall of plant cells. Lignin functions mainly as an agent, which can be fungicidal, hydrophobic, binder for cellulose fibers, and strengthener of cell walls [21,31]. Its chemical structure consists of an amorphous macromolecule composed of three basic units: p-hydroxyphenyl, guaiacyl, and syringyl [23,31]. The higher levels of syringyl compared with those of guaiacyl present in lignin indicate the readiness degree by which lignin can be from lignocellulosic fibers, known as delignification process [32,33].

Hemicelluloses are also considered extremely important in the structure of lignocellulosic fibers, as they are closely associated with cellulose, forming holocellulose, which presents hydrophilicity and provide plant fibers with elasticity [21,22,34]. Hemicelluloses are composed of distinct groups of carbohydrates (pentoses, hexoses, hexuronic acids and deoxyhexoses) of low molecular weight with no long-standing crystalline structure [33,22].

Finally, cellulose $(C_6H_{10}O_5)_n$ is considered the most important component of lignocellulosic fibers. It is a polysaccharide formed by the repetition of β -D-glucopyranose units grouped by glycosidic linkage [35]. The second unit of the monomer is twisted 180° in relation to its first unit, forming a monomer consisting of two β -D-glucopyranose units called cellobiose [29,36], as shown in Figure 2.1b.

The presence of hydroxyl groups (OH) along the cellulose chain allows the solid state of this material to present large regions of ordered chains (crystalline region) and small regions of low molecular order (amorphous region). Six polymorphs of crystalline cellulose are known: cellulose I, II, III₁, III₂, IV₁, and IV₂ [37]. Cellulose I is the natural form synthesized by plants, algae, bacteria, and fungi. It presents two polymorphs, a triclinic (I_α) and a monoclinic (I_β) structure, and the I_α/I_β ratio varies according to the plant/animal origin in which the cellulose is synthesized [38]. Cellulose II is obtained through mercerization (alkaline treatment of cellulose I) or regeneration (solubilization of cellulose I in solvent followed by precipitation in water). Cellulose III₁ and III₂ can be produced by processing cellulose I or II with amine or ammonia, respectively. Cellulose IV₁ and IV₂ can be obtained by adding cellulose III₁ and III₂ to glycerol at 206 °C, respectively [38–40].

Cellulose is a polymer that presents no melt-state processability, and its solubility is restricted to a few solvents, such as: N-methyl-morpholine N-oxide/water (nNMMO/H₂O), lithium chloride/dimethyl acetamide (LiCl/ DMAc), ionic liquids, and ethylene diamine/salt [36]. In contrast, cellulose is easily functionalized with several chemical groups from the hydroxyls present in the most diverse carbons of the β -D-glucopyranose unit, thus providing processability and solubility to the most diverse organic solvents [41]. The hydroxyl linked to the carbon six of cellulose is the most reactive and can be functionalized with the most diverse chemical groups, such as esters and carboxy groups, forming different cellulose derivatives. The main cellulose derivatives are cellulose acetate (CA) and carboxymethyl cellulose (CMC) [42], as illustrated in Figure 2.2.

Cellulose acetate is obtained from the acetylation process with acetic anhydride in the presence of sulfuric acid (Figure 2.2a). CA presents characteristics of a thermoplastic polymer with a high degree of solubility in organic solvents such as acetone, in addition to having its commercial use consolidated in several products such as cigarette filters [43,44].

Carboxymethyl cellulose can be obtained from the cellulose oxidation process using reagents such as sodium hypochlorite (NaClO) and sodium bromide (NaBr) in the presence of the 2,2,6,6-tetramethylpiperidine-1-oxyl radical (TEMPO) catalyst (Figure 2.2b), generating a water-soluble cellulose derivative with functional properties for several applications, such as flocculating agent and emulsifier [45,46].

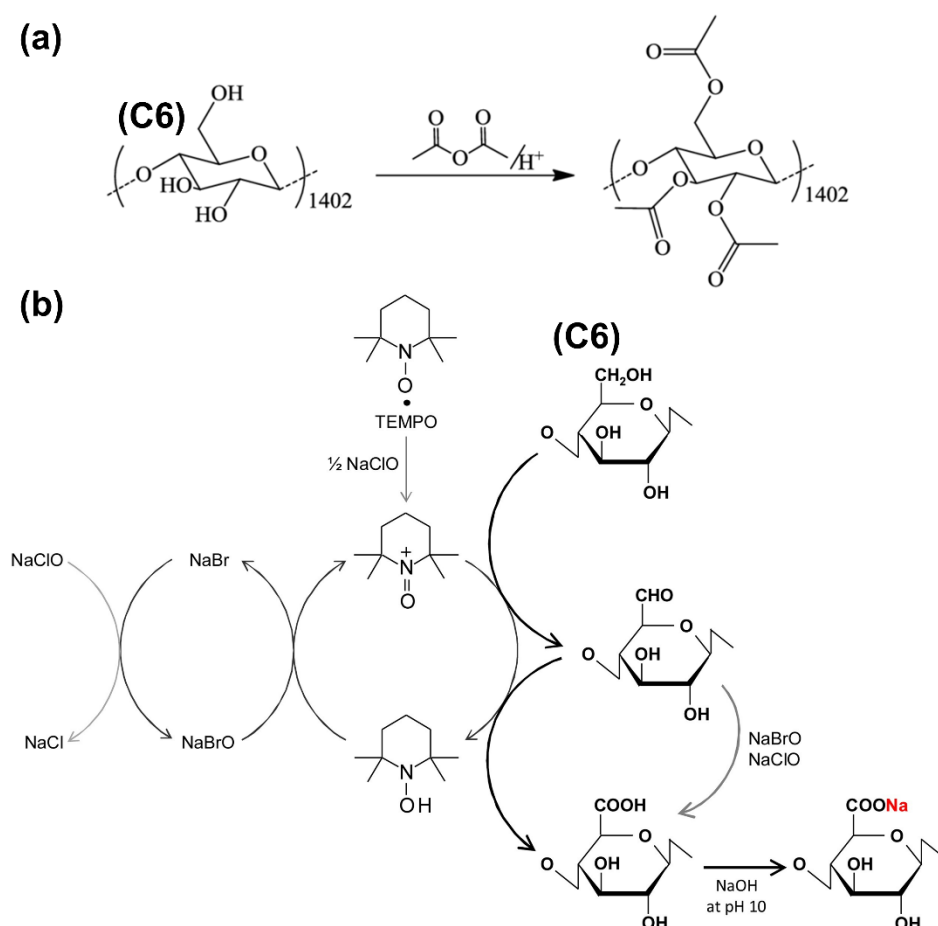


Figure 2.2 - Main cellulose functionalizing reactions: (a) Cellulose acetylation to obtain CA; (b) Cellulose oxidation to obtain CMC. Reprinted with permission from El Barkany, S. et al. [47] and Isogai A. et al. [45].

2.1.2 Pineapple leaf fibers (PALFs)

Pineapple is the sixth most economically exploited tropical fruit in the world, with a production of 28 million tons in 2018. This fruit is grown mainly in Brazil, the Philippines, Costa Rica, Thailand, China, Indonesia, and India. According to the Food and Agriculture Organization of the United Nations (FAO), pineapple production in Brazil was the third largest in the world in 2018, reaching 2.6 million tons [48].

Pineapple is a tropical plant of Amazonian origin belonging to order *Bromeliales*, family *Bromeliaceae*, subfamily *Bromelioideae*, genus *Ananas*, divided into two main species: *Ananas comosus* and *Ananas macromondes* [20,49]. *Ananas comosus* is the best known species and its production is the most widespread, with emphasis on the curaua variety (*Ananas comosus* var. *erectifolius*), a wild pineapple species widely used in ornamentation [50,51].

Curaua PALFs are lignocellulosic fibers and present great pulping potential because of their high concentration of cellulose ($\approx 60\%$ m/m) and the 1:4 syringyl to guaiacyl (S:G) ratio observed in their lignin, which are factors that assist with the delignification process [15,33]. Delignified curaua PALFs can be easily fibrillated through mechanical route, with no need for chemical agents to obtain CNFs, or easily hydrolyzed through chemical route to extract CNCs with over 90% crystallinity [15–17]. Thus, PALFs present greater potential for pulping and extracting cellulose nanostructures compared with other vegetable fibers such as eucalyptus fibers, allowing the use of smaller amounts of chemical reagents in the extraction process [15–17,52].

Pineapple leaf fibers of curaua and other species are by-products used in the manufacturing of handicraft and fabric [53] and in the interior lining of automobiles [54], and in the worst scenarios they end up being incinerated as residue [55]. In the past few decades, PALFs have been employed to reinforce polymer [54,56,57], produce nanopaper from CNC/CNF mixture [16,17], and develop medical implants [18].

Figure 2.3 illustrates the curaua cultivar with highlight for the fruit and crown involved in PALFs.



Figure 2.3 - Illustrative image of the pineapple curaua cultivar with emphasis on the fruit and crown involved in PALFs. Reprinted from Correio da Amazônia [25].

2.1.3 Solution blow spinning (SB-Spinning)

Recently, method to produce polymeric fibers from a solution, known as solution blow spinning (SB-Spinning), was developed using concepts similar to those of electrospinning, but with application of a turbulent air jet directed to the polymeric solution instead of electrical voltage for fiber spinning. SB-Spinning has been established as a simple and inexpensive technique for spinning polymeric fibers, being capable of spinning ~ 0.5 g/h of fibers per nozzle [58]. Figure 2.4 illustrates the SB-Spinning method with its main components.

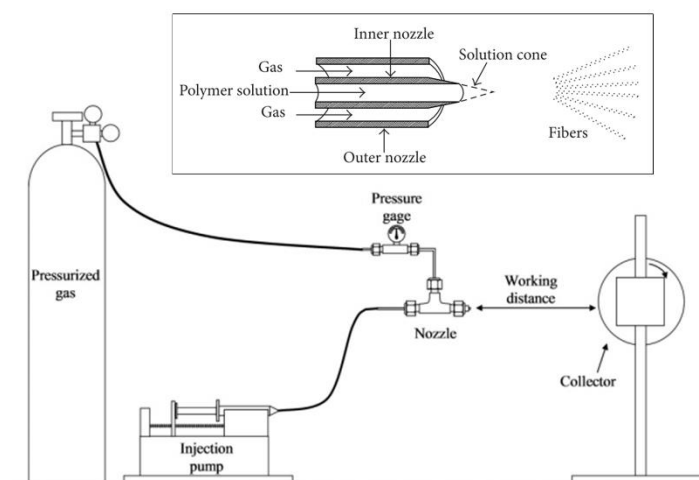


Figure 2.4 - Illustration of the solution blow spinning (SB-Spinning) system. Reprinted with permission from Oliveira et al. [58] and Medeiros et al. [59].

The SB-Spinning system comprises a metal cone into which the polymer solution is fed through an inner nozzle (0.5 mm) and the air is fed through an outer nozzle (1.5 mm), with nozzle tip of 2 mm and inner gap between nozzles of 0.5 mm. The polymeric solution feed rate is controlled by a commercial injection pump, in which a 10 ml glass syringe containing the polymeric solution is coupled and connected to the inner nozzle, controlling the solution flow. The air pressure is also controlled by a pressure gauge connected to the outer metal nozzle. Both the control of the flow solution rate and air pressure are essential for obtaining and controlling the spinning dimension of the polymeric fibers. The distance between the cone and the collector, working distance – (WD), is also evaluated in the process. It is worth mentioning that the fibers are collected by a collector in both rotational and fixed modes [58–60].

The viscosity of the polymeric solution, polymer concentration, solvent evaporation rate, and environmental humidity and temperature should also be assessed in the process to obtain the fibers and dimensionally control them using the SB-Spinning method [58,59]

2.1.4 Field effect transistor (FET) and inverters

The term transistor comes from transfer resistor, as it was known by its inventors. In analog circuits, the resistance transfer process means that the characteristic impedance of the component varies above or below the pre-established voltage bias. From this characteristic, the basic operation principle of a transistor can be defined: use of voltage between two terminals to control the current flow in a third terminal [61].

In this way, a transistor can be used as a controlled source, which is the basis for the design of amplifiers. In the extreme case, the control voltage can be used to make the current in the third terminal vary from zero to a significant value, causing this device to implement an analog switch, which is the basic element of digital circuits. Because of these applications, it is possible to conclude that a transistor is the most important electronic component ever

created, having enabled the revolution of computers and electronic equipment [61].

There are two main types of three-terminal devices: the bipolar junction transistor (BJT), which operates with electrons and holes as charge carriers, and the field effect transistor (FET), whose current control is performed by means of an electric field induced in the conductive region. Both types are equally important, with each presenting distinct advantages and applications. There are basically two types of FET: junction field effect transistor (JFET) and metal-oxide semiconductor field effect transistor (MOSFET) [62].

A MOSFET can be of the N type (NMOS), in which the electric current occurs through electrons in the substrate, or of the P type (PMOS), in which the electric current occurs through holes in the substrate. This study is based on the NMOS, which hereafter will be designated simply as FET. The combination of NMOS and PMOS creates CMOS (complementary metal-oxide semiconductor), in such a way that one complements the other in the need to produce logical functions [62].

Figure 2.5 shows a schematic representation of the different types of transistors presented.

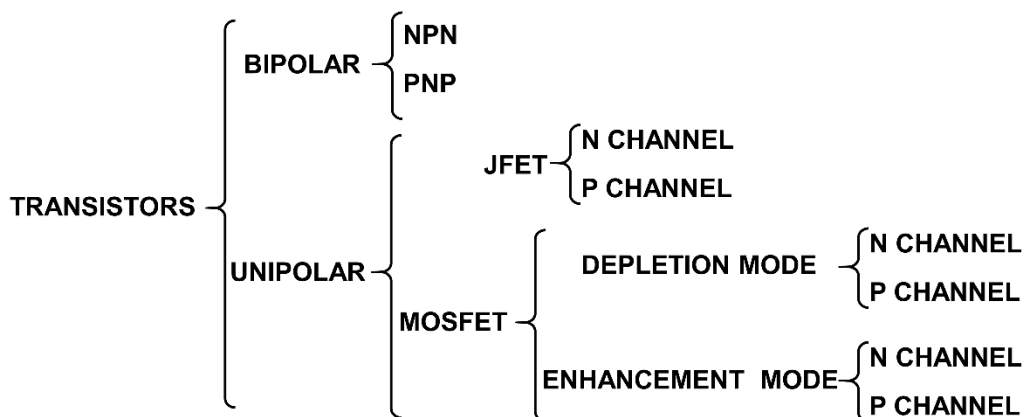


Figure 2.5 - Schematic representation of the different types of transistors.

With respect to the history of transistors, the first FETs were developed by Julius Edgar Lilienfeld in 1926 and Oskar Heil in 1934 [63], whereas the first

BJTs were developed by Shockley, Bardeen and Brattain in late 1947, and would replace the large vacuum valves. In 1956, the three last inventors were awarded the Nobel Prize in Physics for their researches on semiconductors and their discovery of the transistor effect [61].

Figure 2.6 shows the NMOS system.

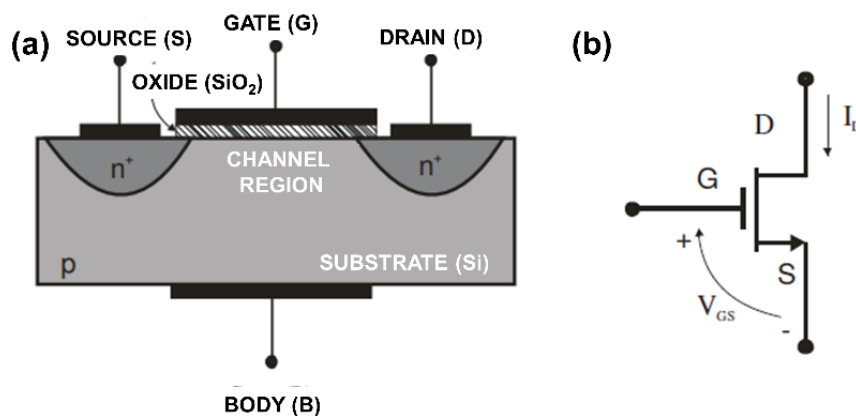


Figure 2.6 - (a) Schematic representation of a NMOS FET; (b) Symbolic representation of a NMOS in a circuit. Adapted from Ferreira [64].

The NMOS transistor is composed of a gate (G), a drain (D), a source (S), a semiconductor substrate material (e.g., silicon), a dielectric material (e.g., silicon dioxide (SiO₂)), and a B body terminal. In simple circuits, there are usually only three accessible terminals, and the B terminal is connected to the source. The source, drain and terminal are made of metallic materials such as aluminum (Figure 2.6a). Figure 2.6b shows the NMOS symbol in a circuit with the drain current (I_D) and the voltage created between the gate and the source (V_{GS}) [62].

The NMOS operates in three regions, as outlined in Figure 2.7.

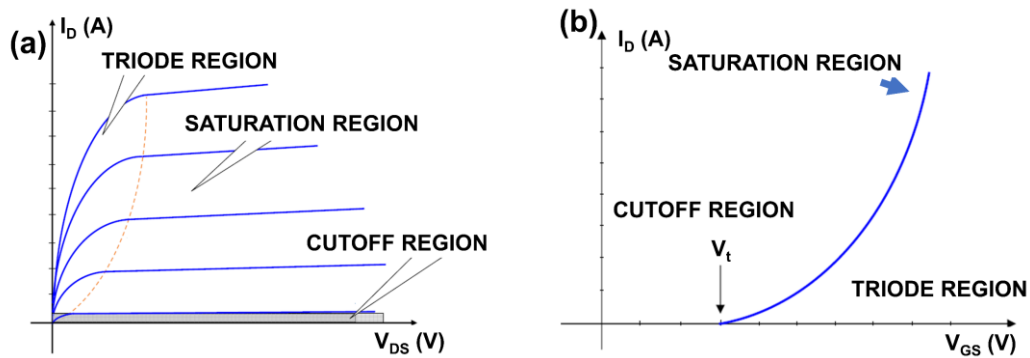


Figure 2.7 - Representation of the three operating regions of a FET in relation to (a) drain current variation (I_D) as a function of drain and source voltage (V_{DS}) and in relation to (b) drain current variation (I_D) as a function of gate and source voltage (V_{GS}). Adapted from Ferreira [64].

The first operating region of a NMOS is the cutoff region. This region occurs when $V_{GS} < V_t$, where V_t is the voltage threshold, which is the minimum V_{GS} value to induce the conducting channel. The transistor remains off and there is no conduction between the drain and source. While I_D should ideally be zero because the switch is off, there is a weak inverted current [62,64,65], as shown in Figure 2.7a and b.

The second operating region of a NMOS is the triode region. This region occurs when $V_{GS} > V_t$ and $V_{DS} < V_{GS} - V_t$, where V_{DS} is the current between the drain and the source. The transistor remains on and the conducting channel is induced, allowing current flow between the drain and source, thus I_D varies as a function of V_{DS} and V_{GS} , as shown in Figure 2.7a and b. In this case, a depletion region occurs in the Si substrate as a result of the migration of electrons to the conducting channel. The FET operates as a resistor controlled by the gate voltage [62,64,65]. Figure 2.8 shows a FET model in the triode mode.

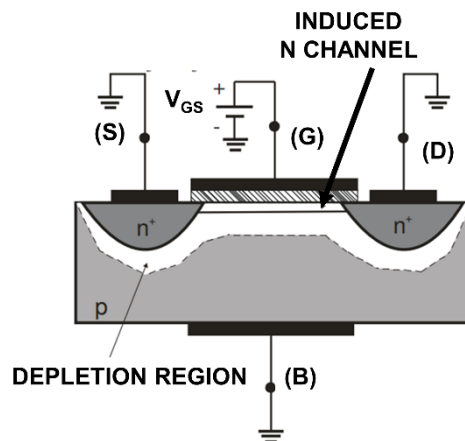


Figure 2.8 - Schematic representation of a FET model in the triode mode. Adapted from Ferreira [64].

Where I_D is obtained by Equation 2.1:

$$I_D = K[2(V_{GS} - V_t)V_{DS} - V_{DS}^2], \text{ where } K = \frac{1}{2} \mu_n C_{OX} \frac{W}{L} \quad (\text{Eq. 2.1})$$

where the K factor is dependent on surface mobility (μ_n), C_{ox} is the oxide capacitance, W is the conducting channel thickness, and L is the channel length [62,64,65].

The third operating region of a NMOS is the saturation region. This region occurs when $V_{GS} > V_t$ and $V_{DS} > V_{GS} - V_t$. The transistor remains on with the channel still induced, allowing current to flow between the drain and the source. As the drain voltage is greater than the gate voltage, part of the channel is turned off. This region is called pinch-off. In this case, the source current is equal to the drain current (I_D) and the gate current (I_G) is null. The I_D is now relatively independent on the drain voltage in relation to the source voltage, and is controlled only by the gate voltage (Figure 2.7 a and b), as described in Equation 2.2:

$$I_D = K(V_{GS} - V_t)^2, \text{ where } K = \frac{1}{2} \mu_n C_{OX} \frac{W}{L} \quad (\text{Eq. 2.2})$$

Figure 2.9 shows a FET model in the saturation mode.

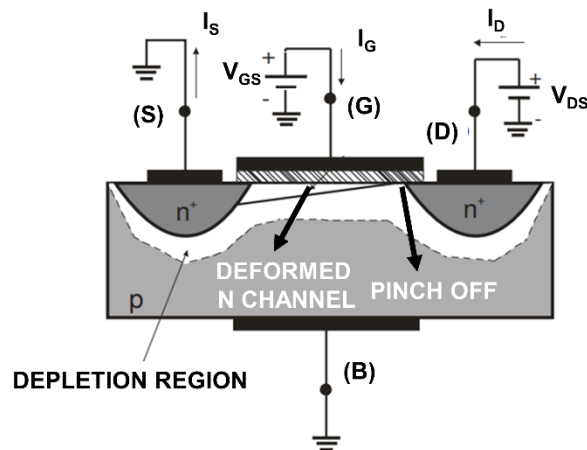


Figure 2.9 - Schematic representation of a FET model in the saturation mode. Adapted from Ferreira [64].

The same equations can be used for the PMOS transistor, but V_t is negative and the inequalities are reversed [62].

The saturation mode of FET is of interest if the transistor is used to operate as an amplifier. For the FET to behave as a switch, the transistor must operate in the cutoff and triode regions, and this operating mode of a FET is widely used in digital circuits [62,66].

In 2008, the research group led by Professor Elvira Fortunato developed a pioneer study addressing the use of cellulose as substrate and dielectric in oxide semiconductor field effect transistors. The first FETs with cellulose fibers as active material opened an unprecedented New Era in the research on paper electronic (paper-e) [67]. This is due to the characteristics of cellulose, which is as the most abundant polymer in the Earth's crust, in addition to being biodegradable, light, and flexible; also, transparent nanopapers can also be produced from cellulose. Furthermore, the average global paper production is 100 million tons/year, and the paper industry can currently produce 30 m of paper per second using the roll-to-roll method, which have made cellulose the substrate most produced and consumed by humans for hundreds of years. From these numerous advantages, paper and other cellulose-based substrates become attractive in view of the high demand for inexpensive and recyclable electronic devices, together with the concept of the Internet-of-Things (IoT)

[11,67–71]. Figure 2.10 shows the schematic representation of a FET with paper as substrate and gate dielectric.

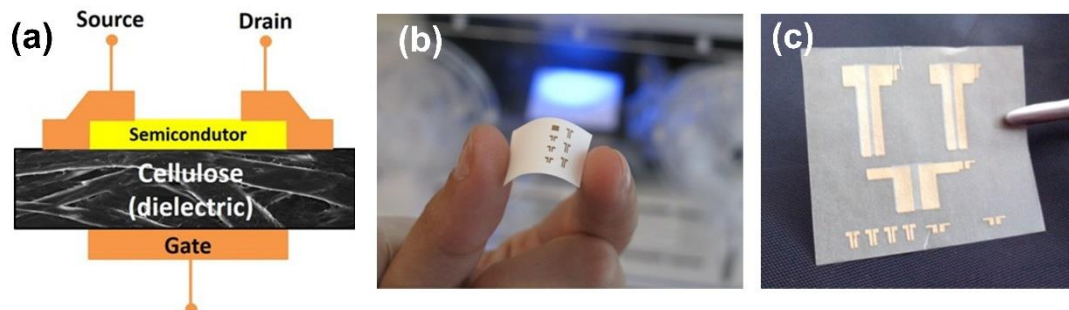


Figure 2.10 - (a) Schematic representation of a FET with paper as substrate and gate dielectric; (b) the first paper FET using oxide as semiconducting material; (c) CMOS on paper. Adapted with permission from Gaspar et al. [72], Fortunato et al. [74] and Martins et al. [77].

The paper used in transistors as dielectric presents a solid-state electrolyte behavior, in which its capacitance is usually generated under low-voltage operation with formation of electrical double layer (EDL) from the voltage applied at the gate. The cations present in the cellulose fibers tend to remain at the edge next to the semiconductor material and the anions tend to remain close to the gate, according to the principle of electrochemistry. The cations at the interface cellulose fiber/semiconductor induce the formation of channel in the semiconductor, and thus the transistor operation. Therefore, the interface between paper and semiconductor becomes extremely important to the transistor operation, with paper roughness being a parameter to be considered in the performance of these electronic devices. Moreover, the fibers hydration level and the type of metallic ion are other parameters to be considered in the operation of paper-based transistors, since they govern the ionic conduction and, consequently, the EDL formation. Figure 2.11 presents a schematic representation of EDL formation on cellulose fibers and a graph of capacitance and phase angle as a function of frequency, indicating the phases of dipole relaxation, ionic relaxation, and EDL formation on paper according to the frequency variation.

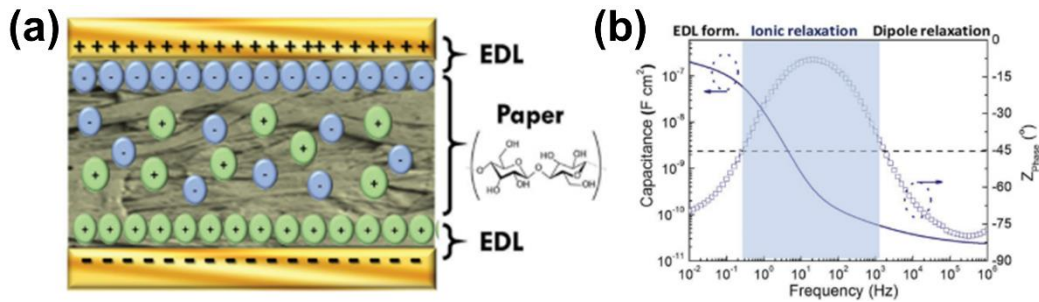


Figure 2.11 - (a) Schematic representation of EDL formation on cellulose fibers; (b) capacitance and phase angle as a function of the frequency applied on paper and the respective polarization regimes that occur on cellulose fibers. Reprinted with permission from Gaspar et al. [73].

It is known that EDL formation on paper (Figure 2.11a) generally occurs at low frequencies related to increased capacitance with angle phase $< -45^\circ$ (Figure 2.11b), thereby indicating the operating conditions of transistors.

It is worth mentioning that there are several works in the literature addressing cellulose as active material that go far beyond FETs [11,72,74], such as for memory transistors [75], solid-state batteries [76], CMOS logic inverters [77], and universal logic gates [73].

Considering the idea of inverters as the basis for logic circuits, those are electronic devices including rectifier, dc bus and inverter stages, responsible for changing the output voltage frequency and magnitude in order to change speed, power of a connected induction motor [77,78]. Figure 2.12 illustrates the two types of inverter structures: an CMOS inverter and a resistor-loaded inverter consisting of a FET coupled to a resistor, in addition to the characteristic voltage curves of an inverter.

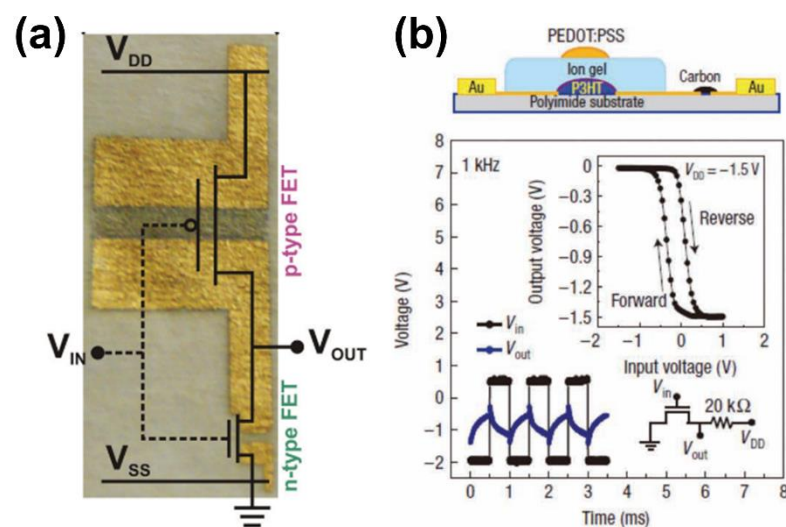


Figure 2.12 - Inverter models. (a) Image of a CMOS on paper with a schematic representation of the inverter circuit. (b) Resistor-loaded inverter using a poly(3,4-ethylenedioxythiophene) polystyrene sulfonate (PEDOT:PSS) gate transistor with a schematic representation of the inverter circuit highlighted V_{OUT} vs. V_{IN} curve and V_{OUT} and V_{IN} as a function of time at 1 kHz. Reprinted with permission from Martins et al. [77] and Cho et al. [78].

The operation of a CMOS inverter consists basically in applying a constant supply voltage (V_{DD}) to the P-type FET source and an input voltage (V_{IN}) to both the N and P type FET gates (Figura 2.12a), thus generating an output voltage (V_{OUT}) inverted to the V_{IN} at the N and P type FET drains (Figura 2.12b). For the case of a FET coupled to a resistance, the operation principle is the same with small differences, V_{DD} is applied to the resistance, V_{IN} is applied to the gate, and V_{OUT} occurs between the drain and resistance (Figure 2.12b). An inverter is characterized by the V_{OUT} vs. V_{IN} curves, as well as by the V_{OUT} and V_{IN} variations as a function of frequency and time (Figure 2.12b) [77,78].

2.1.5 Laser-assisted processing and laser-induced graphene (LIG)

Laser is the acronym for "light amplification by stimulated emission of radiation", that is, it is a device that emits light through an optical amplification process based on the coherent emission of electromagnetic radiation [79]. The first laser device dates from 1960. It was developed by Theodore H. Maiman

based on the theoretical works by Charles Hard Townes and Arthur Leonard Schawlow [80,81]. Laser has numerous applications, from simple to complex ones, namely, barcode and compact disc (CD) readers, information transmission through optical fibers, medical applications in surgery and skin treatment, devices for weapons, complex processing of electronic devices through lithography, and characterization using atomic force microscopy (AFM) by laser beam position variation in relation to angular displacement of the cantilever [82,83].

The literature reports on several types and principles of laser operation, with emphasis on laser using gas, solid-state [84], fiber [85], photonic crystal [86], semiconductor [87], dye [88], free-electron [89] and exotic media [90]. This doctoral thesis focuses on gas laser, more precisely on carbon dioxide (CO_2) laser [91], as shown in Figure 2.13.

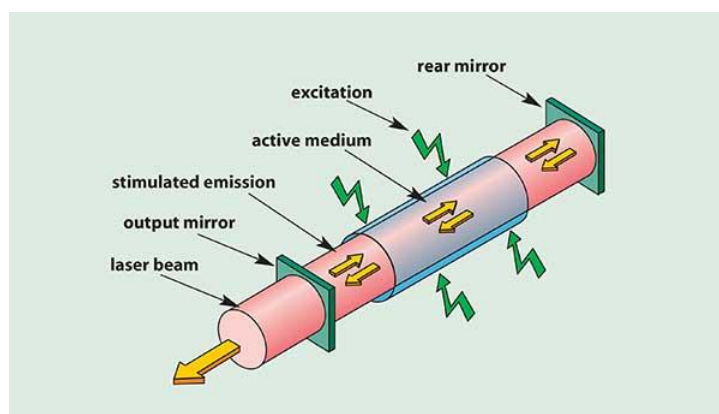


Figure 2.13 - Schematic representation of a CO_2 laser with highly coherent infrared generation and specific wavelength. Reprinted from Photonics Marketplace [92].

This type of laser operates basically on the excitation of CO_2 electrons with emission of photons in the infrared waveband, where they are reflected at one end of the device by the rear mirror and exit coherently and with a specific wavelength through a partially reflective mirror positioned at the other end [91,93].

One of the recent applications of CO_2 laser is the synthesis of laser-induced graphene (LIG) in carbon-based materials - the same technique

applied for the synthesis of graphene from its precursor graphene oxide [94]. LIG is a 3D porous material that presents high thermal stability ($>900\text{ }^{\circ}\text{C}$), electric conductivity ($5\text{-}25\text{ S cm}^{-1}$), and surface area ($\approx 340\text{ m}^2\text{ g}^{-1}$). It is a versatile material that can be easily engineered, structurally and morphologically, speaking simply by changing the laser parameters [95,96]. Laser-assisted processing differs from other processing techniques because of formation of the 3D graphene structure, since it is possible to design complex LIG geometries with high resolution and without the use of a mask, in addition to not requiring high process temperatures and chemical reagents, that raise the synthesis cost [94,95].

This promising graphene is obtained through the photothermal transition of carbon-based materials by pulsed laser irradiation, as illustrated for LIG production in polyimide (PI) substrate (Figure 2.14).

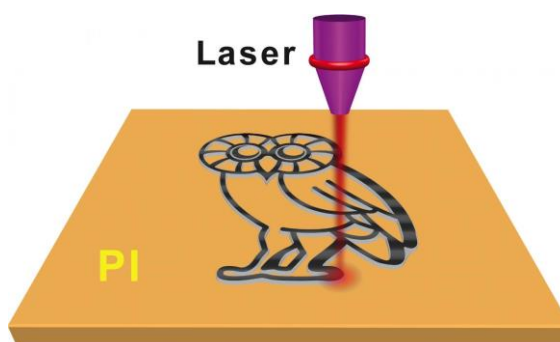


Figure 2.14 - Schematic representation of LIG synthesis on PI substrate. Reproduced with permission [96]. Copyright 2014, Macmillan Publishers Limited.

Production of LIG on carbon substrates that contain aromatic rings occurs directly, and can be performed in an oxidative atmosphere, since the aromatic rings present in these materials have a planar conjugated ring system with delocalized π electron clouds that serves as a precursor of the graphitic structure [95]. Among the main aromatic substrates for obtaining LIG, PI [96–100], polyetherimide (PEI) [96], polyethersulfone (PESU) [101,102], and even lignin [103] are highlighted. For carbohydrates, which do not contain aromatic rings in their chemical structure, such as cellulose and starch, LIG synthesis

occurs in two steps, with intermediate formation of amorphous carbon [104,105]. The LIG synthesis, in this case, must occur in an inert atmosphere and with the use of a fire retardant (e.g., ammonium polyphosphate) [105] or with the oxidation of these materials [104], where metallic ions create a protective atmosphere against ash formation and the carboxyl or phosphate groups assist with the process of forming the graphitic structure based on aromatic rings with double bonds, as illustrated in Figure 2.15.

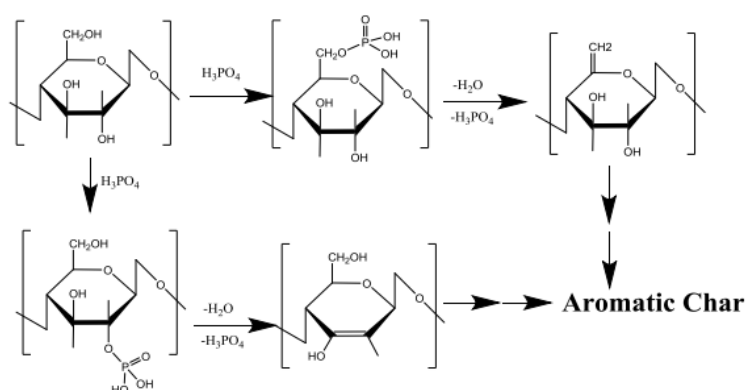


Figure 2.15 - One of the possible formation mechanisms of the graphitic aromatic chain from the cellulose molecule. Reprinted with permission from [105]. Copyright 2018 American Chemical Society.

Production of LIG from cellulose, aided by the peculiar characteristics of this type of raw material, opens new promising possibilities for the application of cellulose not only as a solid-state electrolyte, but also as electrodes in electronic devices.

2.1.6 Zinc oxide ultraviolet (ZnO UV) sensors

Ultraviolet (UV) radiation is, to a certain degree, beneficial to human health due to the production of vitamin D (UVB); however, in most cases, it is the main cause of skin cancer (UVA+UVB). Therefore, UV exposure becomes, in a way, something that should be very well controlled, especially in regions where its incidence is high all throughout the year and exposure to this type of radiation ends up being something difficult to avoid. In this context, UV sensors

become a powerful tool to detect this type of radiation in the environment and, consequently, a tool that can be used to prevent skin cancer. Also aiming at the issue of sustainability and low cost, there is an increasing demand for UV sensors made up of non-toxic, inexpensive materials that guarantee the stability of the device over time, and the ZnO sensors are excellent candidates, because they meet these requirements and are already widely used in the field of UV sensors [106,107].

Zinc oxide is abundant in nature, has a low extraction cost, and presents numerous applications, such as in cosmetics, paint formulation, and as antifungal agent, in addition to being widely used in piezoelectric and photocatalytic devices, transparent conductive electrodes for solar cells, and environmental gas sensors [106,108–113]. This oxide is an N-type semiconductor with a band gap of 3.3 eV and excitation energy of 60 eV, and it has a wide range of electrical conductivity (10^{-9} - $10^4 \Omega \cdot \text{cm}^{-1}$) [114–117]. A ZnO UV sensor functions basically from the interaction between ZnO and UV radiation [108], as illustrated in Figure 2.16.

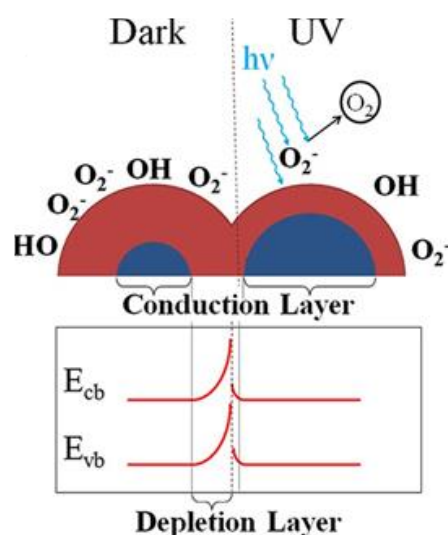


Figure 2.16 - Schematic representation of the photodetection process of ZnO under UV radiation. Reprinted with permission from Jacobs et al. [108].

The basic principle of interaction between ZnO and UV photons and their variation in electrical conductivity is based on the creation of the electron-hole

pair in the conduction band. In the absence of UV incidence, there is no creation of the electron-hole pair, and the material becomes an electrical insulator. Under the incidence of photons at a UV frequency above the ZnO band gap, a photoelectric effect occurs. The electron-hole pair is created, and the holes are quickly swept to the material surface recombining the ionized oxygen through the electron contained in ZnO. Thereby, the probability of carrier recombination decreases inside the material and the electrical photoconductivity increases with the electrons present in the band gap. When the UV radiation on the sample ceases, the electrons are reabsorbed, causing the photocurrent to decay again [108,118–121].

A ZnO sensor is usually composed of interdigital electrodes, which can be made of copper, carbon or graphene. ZnO is deposited between these interdigital electrodes by aqueous suspension or in the composition of inks [97,114]. Figure 2.17 shows the carbon interdigital electrodes deposited on paper substrate, followed by ZnO nanostructures deposited by drop casting. The responsivity curves of ZnO UV sensors under UV on/off radiation are also shown.

It is worth mentioning that the design of the interdigital electrodes, such as the number and width of the contacts as well as the gap between them, influences the sensor performance due to the greater surface area interdigital and the shorter path for the electric current to pass through the interdigital [107].

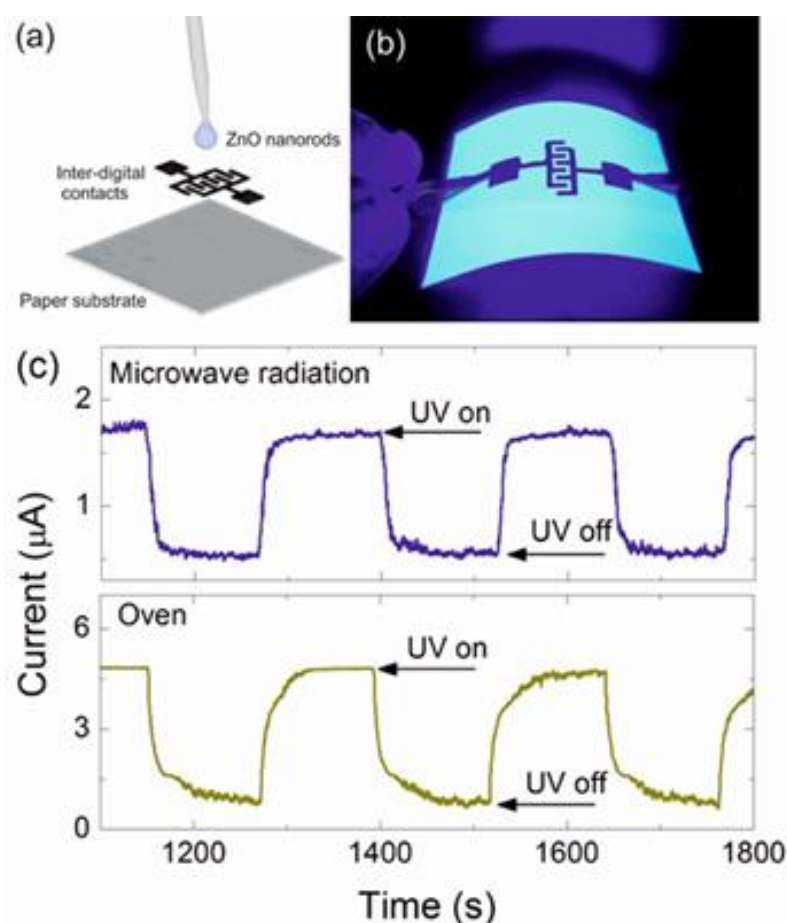


Figure 2.17 – (a) Schematic representation of a ZnO UV sensor production. (b) ZnO UV sensor on paper under UV radiation. (c) ZnO UV sensor responsivity under UV on/off radiation by ZnO nanostructures obtained from microwave and oven. Reprinted with permission from Pimentel et al. [114]. Copyright 2014. American Chemical Society

2.2 State-of-the-art in cellulose as substrate and dielectric for flexible transistors and inverters

The high demand for electronic devices has strongly affected the availability of natural resources, in addition to requiring a good relocation of the waste generated by the disposal of these devices [122,123]. The use of cellulose with dual functionality, as substrate and dielectric, in many types of electronic devices has opened an unprecedented New Era as a solution for this apocalyptic scenario of natural resources depletion along with environmental devastation [124]. As the most abundant renewable biopolymer in the Earth's

crust, cellulose could easily meet this high demand for raw material to produce electronic devices, in line with the search for cheap raw materials that are easy to manufacture and present exceptional properties, such as flexibility and recyclability [7]. However, it is worth highlighting the challenges faced by cellulose as a dielectric in view of the main requirements of a good electrolyte, such as good interface with the semiconductor material and low roughness [125]. It should also be emphasized that formation of EDL in cellulose fibers is strongly dependent on the substrate texture and the humidity conditions of the environment because of the hydrophilic characteristics of these fibers [8,11,126].

In the face of technological advances, an increasing number of group has been searching for portable electronic devices that operate at low voltage (<2 V), in line with the IoT concept of conveying information between humans and things and between things [127,128]. Cellulose-based transistors and inverters operate at low voltage and with high performance using micro- and nano-structured cellulose because of the reduced porosity and roughness (RMS = 0.6 nm – 6 μ m) and functionalization of the fibers with certain metallic ions (Li^+ , Na^+ and K^+) [10,73,129]. In the literature addressing GIZO FETs fabricated on office paper ($I_{\text{ON/OFF}}=10^3\text{-}10^4$; $S_S=0.8$ V dec^{-1}) [74] and nanopaper with superior performance ($I_{\text{ON/OFF}}=10^4\text{-}10^5$; $S_S=2$ V dec^{-1}) [72]. However, the process employed to obtain micro- and nano-structured cellulose may involve chemical routes with high residue generation, mechanical routes with energy expenditure, and even enzymatic routes that demand time and complex equipment infrastructure [130–132].

Solution blow spinning (SB-Spinning) appears as an alternative to these problems in the extraction of micro- and nano-structured cellulose, and it has been established as a simple technique to produce fibers with no need for high temperatures, large amounts of chemical reagents and long dialysis and filtration time [59,133]. Moreover, SB-Spinning is established as a powerful tool for the dimensional control and functionalization of polymeric fibers [58–60].

Several studies have addressed the production of micro- and nano-structured polymeric fibers using SB-Spinning, with highlight for poly(lactic acid)

(PLA) [59], polycaprolactone (PCL) [134], poly(ethylene oxide) (PEO) [58]. These fibers have been extensively investigated for use in scaffolding biomaterials [135], composite reinforcement [136], filtration [137], microchip-based 3D-cell culture [138], and biomedical engineering [139]. In addition, there is a recent study about cellulose-derived fibers blended to polyacrylonitrile (PAN) obtained by SB-Spinning [140] and CA mats obtained by electrospinning applied to electronics [141]. However, to the best of our knowledge, cellulose mat obtained by SB-Spinning applied as electrolyte-gated transistor (EGT) have not yet been reported.

Therefore, this study proposes to develop ICCMs by means of the SB-Spinning approach applied simultaneously as substrate and dielectric for low-voltage operating electronic devices. The ICCMs were prepared from a cellulose acetate (CA) solution suitable for the SB-Spinning process, followed by a deacetylation process using three alkaline hydroxides: lithium hydroxide (LiOH), sodium hydroxide (NaOH), or potassium hydroxide (KOH). CA was chosen as a precursor material for cellulose due to its solubility in several organic solvents [142], compatibility with the processes of spinning [143–146], dry spinning [147] and electrostatic-induction-assisted solution blow spinning [148], as well as to its deacetylation facility [149]. PEO was used as an additive for spinning, as reported for CA spinning systems [150,151].

2.3 State-of-the-art of cellulose as a precursor of LIG electrode for flexible sensors

In view of the environmental issues regarding waste generation and energy consumption presented by several electronic components, from production to final disposal, there is an increased search for materials from renewable sources with low manufacturing cost that can be easily disposed and/or recycled with no further environmental impact [122–124,152]. LIG meets these requirements and is a promising material for electronic and energy storage devices [103,153,154]. It can be applied as a rapidly obtained electrode with industrial scale synthesis capacity without causing major impacts on the

environment or depending on traditional multi-step production processes associated with cleanroom techniques [94,95].

Among the numerous applications of LIG, the literature highlights its use in supercapacitors [96,155–158], sustainable energy conversions [159,160], microfluidics [161–163], antimicrobial electrodes [97,101,102], sensors and biosensors [100,107,164–174]. In the area of ZnO UV sensors using LIG as electrode, studies addressing LIG obtained from PI/PEI substrates presenting responsivity of 2 and 92 nA/W, respectively, for 1 V bias stand out in the literature [107,170]. In addition, a study reported the potential for obtaining LIG from cork lignocellulosic material for use in ZnO UV sensors with responsivity of approximately 4.4 μ A/W for 5 V bias [175].

Although there are several studies reporting the synthesis of LIG from cellulose in the literature, to the best of our knowledge, the only research addressing this synthesis was aimed at developing ammonia (NH₃) sensors. This type of sensor presented a detection limit of 0.33% NH₃ concentrated in the atmosphere - a performance considered low compared with that of other gas sensors [173]. Among the possible causes for this low performance of the LIG obtained from cellulose, high porosity and problems with the interface with other materials can be listed [176,177]. Therefore, the second stage of this doctoral thesis aims to investigate the production of laser-induced graphene electrodes (LIGE) from the formulation of CMC-based inks containing LIG synthesized from CNCs extracted from PALFs, thus addressing possible porosity and interface problems caused by electrodes directly obtained from LIG. The justification for using CNCs extracted from PALFs is associated, first, with the production availability of these fibers, which in most of cases end up being incinerated, and second with the fact that CNCs present a high crystallinity index that can favor the formation of LIG, in addition to the facility of extracting lignocellulosic fibers using a moderate amount of chemical reagents [15–17,52], as discussed in subitem 2.1.2. According to our analysis, the cellulose crystallinity promotes photothermal resistance to laser, assisting on LIG formation [105]. ZnO UV sensors were produced to validate the proposed methodology for obtaining LIGE. In this context, it is intended to establish cellulose as a LIGE precursor for

UV sensors, opening new promising possibilities for organic electronics, considering that the use of cellulose as substrate and dielectric in several electronic devices is already consolidated [10,11,72,74–77].

3 MATERIALS AND METHODS

3.1 ICCMs obtained by SB-Spinning as substrate and dielectric for flexible electronics

3.1.1 Materials

Cellulose acetate (CA) ($\rho=1.3 \text{ g/cm}^3$, $M_n=52,000$ and 39.20-40.20 %wt acetyl) (Sigma-Aldrich, USA); poly(ethylene oxide) (PEO) ($M_v=400,000 \text{ Da}$) (Sigma-Aldrich, USA); formic acid 98-100% v/v (Sigma-Aldrich, USA); acetic acid (99.7%, Exodo, Brazil); ethanol absolute, anhydrous (CARLO ERBA), LiOH $\geq 98\%$ (Sigma-Aldrich, USA); NaOH $\geq 96\%$ (LABKEM); KOH $\geq 90\%$ (Sigma-Aldrich, USA).

3.1.2 Preparation of CA-based mats by SB-Spinning

Cellulose acetate polymeric solutions at a concentration of 8 w/v % were obtained in a formic acid (FA)/acetic acid (AA) 2:1 (v:v) ratio solution with PEO molecular weight values of 0, 0.04, 0.08, 0.24 and 0.40 w/v % in relation to solvent. This solvent was chosen according to the boiling point, vapor pressure, and Hansen solubility parameters for solvents and CA weight concentration reported by Ghorani et al. [178], as described in Table 3.1.

The boiling point and vapor pressure of acids ensured that the material was apparently dried when it reached to the collector, and maintained the solution stable in the nozzle jet. The Hansen solubility parameters ($D_{(s-p)}$) of the acids are lower than the solubility radius (R) of CA, which guarantees CA solubility in the 2:1 (v:v) (FA)/(AA) mixture [178], as illustrated in Figure 3.1.

Solutions of PEO at the concentrations of 0.24 and 0.40 m/v % without CA were prepared to verify only the effect of PEO on the formation of spun fibers. First, the solutions were stirred at 180 rpm for 12 h using a Jeio Tech stirrer and then mechanically stirred in a magnetic stirrer for extra 3 h. Table 3.2 shows all the CA, PEO and CA-PEO formulations, SB-Spinning flow rates, and types of collector investigated to obtain the best CA fibers.

Table 3.1 - Boiling point and vapor pressure of solvents and Hansen solubility parameters of solvents and CA

Solvents and CA	Boiling point (°C)	Vapor pressure (kPa)	Hansen solubility parameters	
			D _(s-p) for CA	R for CA
Acetic acid	118	1.33 (17 °C)	2.68	
Formic acid	101	4.4 (20 °C)	7.39	
CA				12.4

Table 3.2 - Detailed information of the prepared samples, and respective nomenclature depending of CA and PEO composition as well as SB-Spinning parameters

Sample	CA (m/v %)	PEO (m/v %)	Flow rate (ml/h)	Type of collector
Neat CA_3.5	8	0	3.5	aluminum film
Neat CA_7.0	8	0	7.0	aluminum film
Neat CA_10.0	8	0	10.0	aluminum film
CA_PEO 0.04_3.5	8	0.04	3.5	aluminum film
CA_PEO 0.04_7.0	8	0.04	7.0	aluminum film
CA_PEO 0.04_10.0	8	0.04	10.0	aluminum film
CA_PEO 0.08_3.5	8	0.08	3.5	grating
CA_PEO 0.08_7.0	8	0.08	7.0	grating

CA_PEO 0.08_10.0	8	0.08	10.0	grating
CA_PEO 0.24_3.5	8	0.24	3.5	grating
CA_PEO 0.24_7.0	8	0.24	7.0	grating
CA_PEO 0.24_10.0	8	0.24	10.0	grating
CA_PEO 0.40_3.5	8	0.40	3.5	grating
CA_PEO 0.40_7.0	8	0.40	7.0	grating
CA_PEO 0.40_10.0	8	0.40	10.0	grating
PEO 0.24_3.5	0	0.24	3.5	aluminum film
PEO 0.24_7.0	0	0.24	7.0	aluminum film
PEO 0.24_10.0	0	0.24	10.0	aluminum film
PEO 0.40_3.5	0	0.40	3.5	aluminum film
PEO 0.40_7.0	0	0.40	7.0	aluminum film
PEO 0.40_10.0	0	0.40	10.0	aluminum film

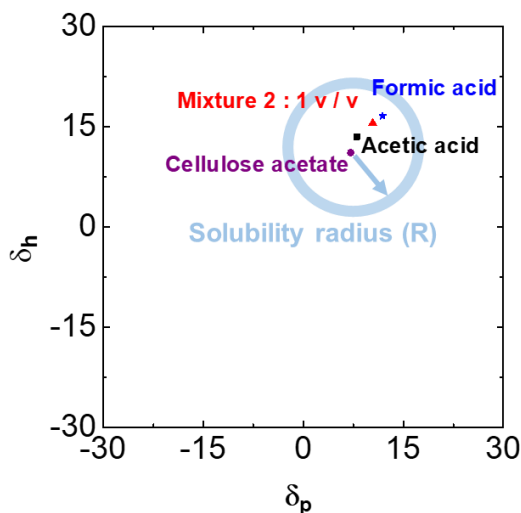


Figure 3.1 - Hansen parameters describing the CA solubility range in formic and acetic acids.

The polymer solutions were poured into a 25 mL glass syringe (Arti Glass, Italy) coupled to a syringe pump (New Era Pump Systems Inc., USA). A rotational speed of 180 rpm was applied to the collectors, which used a grating to collect the fibers and form the mat without sticking to the collector. On the other hand, an aluminum film was used when there were no fibers formation to collect the residual polymer solution. The spinning process occurred at a pressure of 30 psi, keeping the tip and the collector at a fixed distance of 20 cm under a controlled atmosphere: $T \sim 25$ °C and relative humidity (RH) of 45–50%.

3.1.3 Characterization of CA-based mats

Formation of CA films or CA fibers was characterized by scanning electron microscopy (SEM) using a JMS 6510 (JEOL®) microscope operated at accelerating voltage of 15 kV. All samples were sputter-coated with gold using a Leica EM SCD050 device and attached to SEM copper stubs using carbon strips. The diameter of the CA-PEO fibers was measured using the ImageJ 2.0 software (available at <http://rsb.info.nih.gov/ij/>; by Wayne Rasband, National Institutes of Health, Bethesda, MD, USA). Regression analysis was conducted to assess the effects of PEO concentration, flow rate, and their interaction on

the diameter of the CA-PEO fibers. Data were processed using the R 3.5.0 software. A significance level of 5% ($p < 0.05$) was adopted for all statistical analyses.

Interaction between CA and PEO was investigated using Fourier transform infrared spectroscopy (FTIR). The spectra were obtained by means of 68 scans per sample using a Bruker Vertex 50 spectrometer with attenuated total reflectance (ATR) operating between 4000-400 cm^{-1} at 2 cm^{-1} resolution. Infrared (IR) spectra were normalized to the highest intensity peak using the OriginPro[®] 8.0 software, considering the humidity control (50% H. R.).

A rheological test was performed to assess possible molecular interactions between PEO-CA, CA-CA, and PEO-PEO in solution. The CA and CA-PEO solutions were analyzed under oscillatory regime using an Anton-Paar[®] Physica MCR 301 modular rheometer in a concentric-cylinder cup system at 25 °C, 1-500 rad/s angular frequency, 1% constant deformation (linear viscoelastic region). The PEO and acid solutions were analyzed under the same conditions but using a Couette flow system because of their low viscosity.

3.1.4 Preparation of ICCMs

First, deacetylation was carried out by swelling the CA-PEO fibers in water for 24 h, followed by immersion of 100 mg of the CA-PEO mats in 50 ml of alkaline hydroxides (LiOH, NaOH, or KOH): ethanol solution (0.5 N) for 4 h in a Jeio[®] Tech stirrer at 180 rpm. The deacetylated ICCMs were removed from the alkaline solution and dried at room temperature for 48 h.

3.1.5 Characterization of ICCMs

X-ray diffraction (XRD) analysis of the CA-PEO and ionic conductive cellulose mats were performed on a Shimadzu[®] XRD 600 diffractometer using $\text{CuK}\alpha$ radiation at 30 kV and 40 mA. Scattering radiation was detected in the 5–45° 2θ range at a scan rate of 1°/min. The specimens were prepared on glass supports with the least rough sample to minimize the noise effect in the XRD

analyses. The crystallinity index (CI) of the ICCMs was calculated following the empirical method proposed by Segal et al. [177], according to Equation 3.1:

$$CI = (I_t - I_a) / I_t \times 100 \quad \text{Eq. 3.1}$$

where: CI is the crystalline index; I_t is the total intensity of the crystalline peak (020) for cellulose II at $2\theta=21.7^\circ$, and I_a is the amorphous intensity at $2\theta=16^\circ$.

FTIR analyses of the CA-PEO and ICCMs were conducted to verify the effectiveness of the deacetylation process using alkaline hydroxide solutions. The same FTIR equipment and conditions employed to characterize the cellulose acetate-based mats were used in these analyses.

Thermal stability investigation of CA-PEO and ICCMs was carried out using a TGA-DSC-STA 449 F3 Jupiter® thermal analyzer under synthetic air atmosphere (40 ml/min) up to 550 °C with a heating rate of 10 °C/min.

Roughness of the ICCMs was estimated by 3D profilometry using an Ambios XP-Plus 200 Stylus profiler.

Scanning Electron Microscopy/Energy Dispersive X-Ray Spectroscopy (SEM-EDS) analyses were performed to analyze the cellulose fibers and estimate the Na^+ and K^+ ions content absorbed in the ICCMs using a Zeiss Auriga Crossbeam microscope with carbon-coated samples. The diameter of the cellulose fibers was also calculated using the ImageJ 2.0 software (available at <http://rsb.info.nih.gov/ij>, by Wayne Rasband, National Institutes of Health, Bethesda, MD, USA).

X-ray photoelectron spectroscopy (XPS) was performed to quantify the Li^+ ions absorbed on the ICCMs on an AXIS Supra™ Kratos Analytical device.

Electrochemical characterization of the ICCMs was carried out at room temperature (23 ± 2 °C and RH $\approx 40\%$) using a Gamry Instruments Reference 600 potentiostat coupled to a probe and gold plate configuration.

3.1.6 Fabrication of FETs and inverters

A 35 nm-thick amorphous indium-gallium-zinc oxide (a-GIZO) semiconducting layer (1:2:2 % mol-Ga₂O₃:In₂O₃:ZnO) was deposited by radio frequency (RF) magnetron sputtering (AJA ORION system) on one side of the ICCM. A degenerate semiconducting 200 nm-thick indium-zinc oxide (IZO) film (In₂O₃-ZnO; 89.3: 10.7 wt%) was deposited by RF sputtering as part of the bottom gate on the other side of the ICCM. Next, source/drain (S/D) aluminum electrodes were deposited in the channel region by electron-beam evaporation with aluminum film thickness of 200 nm using shadow masks, as illustrated in Figure 3.2. A resistive load inverter was manufactured by drawing graphical lines using an HB-2 pencil (Black'Peps, Maped) to define the load resistances. The electrical connection between the drain electrode and the load resistance were established using a rollerball silver conductive ink pen (Circuit Scribe).

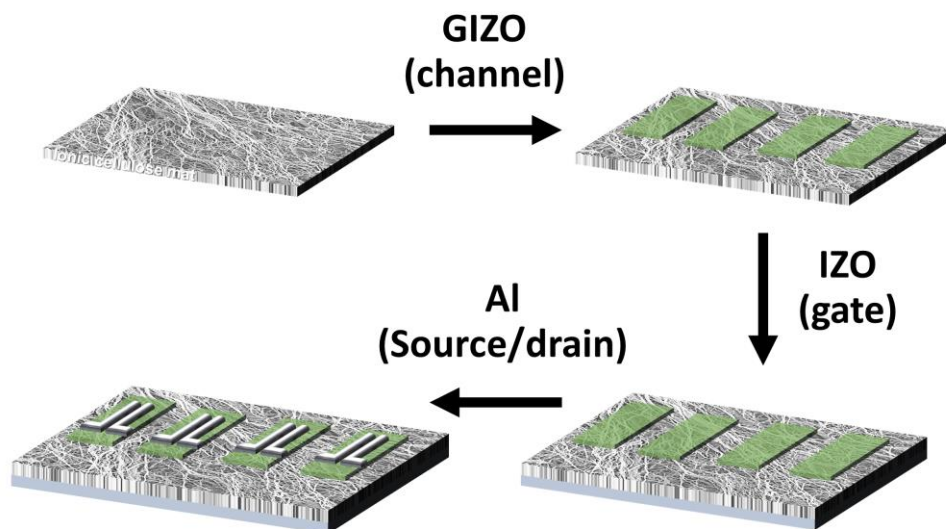


Figure 3.2 – Schematic illustration about fabrication of FETs on ICCMs.

3.1.7 Characterization of the dielectric FETs and inverters

Field effect transistors in the flat (top) and folded (bottom) modes were characterized at room temperature (23 ± 2 °C and RH \approx 40%) in a dark box using a micro-probing station (Cascade Microtech M150) connected to a semiconductor parameter analyzer (Keysight B1500A) using the EasyEXPERT

software. The bending tests were conducted under flexural inward and outward deformation along the channel axis while varying the curvature radius from 45 to 15 mm. Between each inward and outward deformation cycle, the FETs were characterized in the flat mode to investigate the effects after each bend radius test. The dynamic electrical characterization of inverters at different frequencies (0.1–3 Hz) was carried out using a Keysight B1500A analyzer coupled to a Microtech M150 probing station and an oscilloscope (ISO-TECH IDS 8062). The transistors were analyzed by optical microscopy (Olympus BX51).

3.2 LIGE from pineapple CNCs and CMC-based ink for ZnO UV sensors

3.2.1 Materials

Sodium carboxymethyl cellulose (CMC) (Mw=90,000) (Sigma-Aldrich, USA); pineapple leaf fibers (PALFs) obtained from curaua (*Ananas erectifolius*) supplied by the Brazilian Agricultural Research Corporation (Embrapa), Embrapa Eastern Amazon; zinc oxide nanopowder <100 nm (Sigma-Aldrich, USA), ethanol absolute, anhydrous (CARLO ERBA), sulfuric acid 98-100% v/v, (Dinâmica), hydrochloric acid 36-38% (Synth), hydrogen peroxide 34-36% v/v, (Synth), NaOH ≥96% (Vetec™); tracing paper.

3.2.2 Delignification pretreatment of PALFs and CNCs extraction from PALFs

In natura PALFs extracted from curaua were mercerized with NaOH 5 wt% at 60 °C and then bleached in a solution (1:1 v/v) containing NaOH 4 wt% and hydrogen peroxide (H₂O₂) 24% (v/v) at 60 °C, as described by Claro et al. [16,17].

The CNCs were extracted from bleached PALFs by acid hydrolysis in a solution (2:1 v/v) containing sulfuric acid (H₂SO₄) 60% (v/v) and hydrochloric acid (HCl) (36.5 wt%) at 45 °C, thus maintaining the thermal stability of the sample due to the absence of sulfate on the fiber surface, as proposed by Corrêa et al. [15]. The CNCs were neutralized by dialysis tubing on cellulose membranes (D9402, Sigma-Aldrich®) for 96 h.

3.2.3 Fabrication of ZnO UV sensors with interdigital LIGE

Figure 3.3 shows an overview of the new approach proposed to obtain interdigital LIGE for ZnO UV sensors using an Universal Laser System (ULS): 10.6 μm CO₂, VLS 3.50 laser, 2.0" lens kit, 50.8 mm focal length, and 0.127 mm beam diameter. The LIGE are composed of LIG obtained from CNCs and CMC-based ink containing sodium (Na⁺) ions by varying the laser focus, laser power and tip speed parameters. First, the CNCs were functionalized using commercial spray-on fire retardant (BanFire) as reported in the literature for LIG on cellulose fibers [105]. Next, the CNCs were compressed to 5 ton/min using a manual hydraulic press (Specac), forming a 5 mm-thick CNC tablet. The laser parameters used for obtaining LIG from the CNC tablet were investigated to produce LIG with greater electrical conductivity. Aiming at the best parameters, a laser beam with ± 1.1 mm ($\pm F$) defocus including the focal plane (0F) was applied as a function of tip speed at 5.5, 5.8 and 6.0 cm/s using a 4 W laser power, followed by varying the laser power between 3.5 and 4.5 W in relation to the best focus condition as a function of tip speed. It is worth noting that +1.1 mm (+F) defocus is the equipment limit so that the sample does not touch the laser tip.

The LIG with the lowest sheet electrical resistance formed on the CNC tablet was used to formulate the CMC-based ink dissolved in 50/50 v/v water/ethanol mixture in the following CMC/LIG mass percent concentrations in solution: 3/0 (LIG_0); 3/0.6 (LIG_0.6); 3/1.2 (LIG_1.2). CMC-based ink interdigital electrodes with different LIG concentrations were drawn using a brush and adhesive tape as a mask on a high-purity tracing paper as substrate. The interdigital LIGE were designed with a 0.5 mm gap between 15 contacts with 0.5 mm thickness and interconnection by main contacts of 30x10 mm (length x width). When the ink is dry, the laser is passed on the ink electrodes to produce more LIG from CMC. Also aiming at a greater conductivity of the CMC graphene, the laser parameters for the CMC-based ink were investigated following the same methodology applied for the CNC tablet. Aiming at the best parameters for the CMC-based ink, a laser beam with ± 1.1 mm ($\pm F$) defocus including the focal plane (0F) was applied as a function of tip speed at 7.6, 8.2

and 8.9 cm/s using a 2.4 W laser power, followed by varying the laser power between 2.3 and 2.5 W in relation to the best focus condition as a function of tip speed.

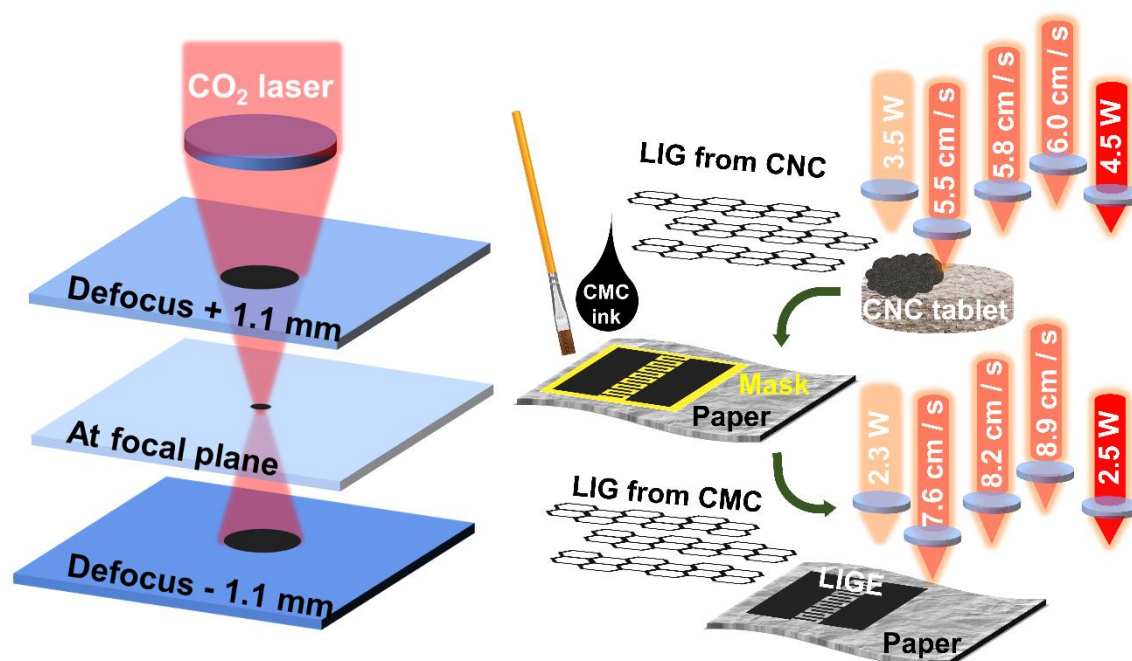


Figure 3.3 - Overview of the new approach proposed to obtain interdigital LIGE from pineapple CNCs and CMC-based ink by varying the laser focus, laser power and tip speed parameters.

In addition, the tracing paper was oxidized to produce direct-written laser-induced graphene electrodes (DLIGE) on paper substrate and compare them with the LIGE obtained from CMC-based ink. Paper oxidation consisted in converting primary cellulose hydroxyls into carboxyl acids using the TEMPO catalyst [179]. An amount of 6.85 g of paper was submerged in 400 ml of deionized water, followed by addition of 85.7 mg TEMPO and 0.857 g sodium bromide (NaBr) in 12 ml of deionized water each. After that, the solution was vigorously stirred for 1 h with addition of 36.46 g of sodium hypochlorite (NaClO). Subsequently, the solution pH was adjusted to 10 during oxidation by adding 1M NaOH solution, as reported in the literature [104,179]. Finally, after 1 h, the paper was removed from the solution and left to dry at room temperature.

The oxidized paper underwent the same laser process in the same equipment used for CNC and CMC, with 2.4 W laser power, 8.2 cm/s tip speed, and +1.1 mm defocus in relation to the focal plane, varying only the number of passes: one laser pass (Paper_P1) and two laser passes (Paper_P2) on the paper surface, as proposed by Chyan et al. [105]. The same interdigital LIGE dimensions applied to CMC-based ink were directly laser written on the paper without a shadow mask.

The CMC-based ink with ZnO was prepared by completely dissolving 3 wt% CMC in water and adding 40 wt% ZnO nanoparticles under slow stirring. The CMC-based ink with ZnO was deposited on all interdigital LIGE using the screen-printing technique.

Aiming to calculate the sheet resistance for all formulations, 5x5 mm squares were drawn and silver contacts were deposited at the opposite edges of the square using a rollerball pen (Circuit Scribe) for electrical characterization by needle contact.

3.2.4 Characterization of ZnO UV sensors

The structure of CNCs was analyzed by transmission electron microscopy (TEM) using a FEI Magellan 400 L microscope. The LIG of CNCs and LIGE of all formulations were characterized by scanning electron microscopy (SEM) using a Carl Zeiss AURIGA® Cross Beam® to analyze their profile and interface with the tracing paper substrate.

The physical properties of LIG obtained from CNC, CMC, and tracing paper were characterized using a Renishaw Qontor Raman microscope with a laser beam of 633 nm at 16 mW during 10 s exposure time with five accumulations to obtain the Raman spectra. Through characteristic Raman spectra of graphene, the intensity ratio of the D and G bands (I_D/I_G) can be determined to estimate the number of defects in LIG materials, where the D band represents the graphene defects/folded graphene layers and the G band represents the quality of graphitization induced by the carbon atom order degree [180,181]. The I_{2D}/I_G ratio can also be measured by Raman spectra, and indicates the number of graphene layers, where I_{2D} corresponds to the 2D band

that is related to phonons with opposite moment in the graphitic material and suggests the formation of conductive crystalline graphene [182,183].

Sheet resistance (R_s) of all formulations was measured from the LIG square (10x10 mm) with layer thickness (~1 mm) and the resistivity calculated from the IV curves (from -1 to 1 V) obtained at room temperature (23 ±2 °C, RH ≈40%) in a dark box using a micro-probing station (Cascade Microtech M150) connected to a semiconductor parameter analyzer (Keysight B1500A) using the EasyEXPERT software.

Electrochemical characterization of the ZnO UV sensors was carried out at room temperature (23 ±2 °C, RH ≈40%) using a Gamry Instruments Reference 600 potentiostat applying a 10 V constant voltage bias. Current vs time curves were obtained by cyclically exposing the sensors, in a dark box, to ultraviolet light (UV lamp, UVL-28 EL series) at 8 W power wavelength and 365 nm wavelength between 30-120 s periods. The responsivity (R_{res}) of the ZnO UV sensors was estimated according to the Equation 3.2 [184]:

$$R_{res} = \frac{I_{ph} - I_{dark}}{P_{UV}} \quad \text{Eq. 3.2}$$

where: I_{ph} and I_{dark} are the magnitudes of the photocurrent and dark current, respectively, and P_{UV} is the power of the UV source.

Aiming to obtain flexible electronic devices, bending tests were conducted under flexural inward (IN) and outward (OUT) deformation along the channel axis while varying the curvature radius from 45 to 15 mm using metal supports on the same potentiostat equipment.

It is important to note that all characterizations reported in the section 3 were performed after the samples conditioned to RH ≈ 50%.

4 RESULTS AND DISCUSSIONS

4.1 ICCM by SB-Spinning as substrate and dielectric “interstrate” layer for flexible electronics

4.1.1 Design and engineering of CA-based mats by SB-Spinning

This first stage aims to demonstrate the results for ICCMs obtained by SB-Spinning with subsequent deacetylation process applied as substrate and dielectric “interstrate” layer for FETs and inverters.

Cellulose acetate and poly(ethylene oxide) defect-free fibers were obtained by varying solution PEO concentration and flow rate in SB-Spinning, as shown in the SEM micrographs in Figure 4.1.

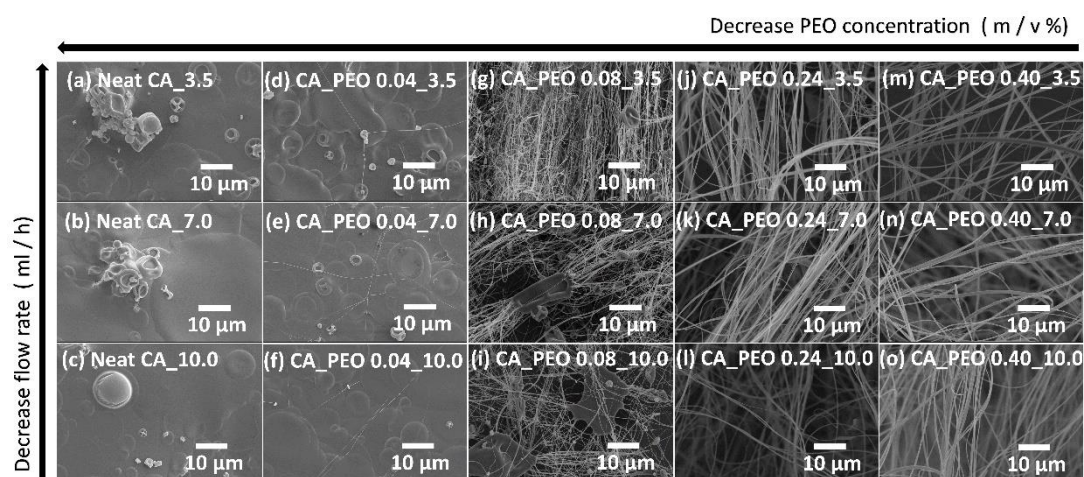


Figure 4.1 - SEM micrographs evaluating the effect of PEO on CA fiber formation and flow rate during the SB-Spinning process: (a) Neat CA_3.5; (b) Neat CA_7.0; (c) Neat CA_10.0; (d) CA_PEO 0.04_3.5; (e) CA_PEO 0.04_7.0; (f) CA_PEO 0.04_10.0; (g) CA_PEO 0.08_3.5; (h) CA_PEO 0.08_7.0; (i) CA_PEO 0.08_10.0; (j) CA_PEO 0.24_3.5; (k) CA_PEO 0.24_7.0; (l) CA_PEO 0.24_10.0; (m) CA_PEO 0.40_3.5; (n) CA_PEO 0.40_7.0; and (o) CA_PEO 0.40_10.0.

The neat CA solution only formed films with particles in the aluminum collector, as it can be observed in Figures 4.1a-c. Fiber formation began when 0.04 m/v% of PEO was added to the solution, but mostly film and particles continued to be formed, as shown in Figures 4.1d-f. Increased PEO

concentration assisted with formation of defect-free CA fibers (Figs. 4.1g-o), and the minimum amount of 0.24 m/v% of PEO was needed to obtain well-defined, defect-free CA-PEO fibers. In addition, it was not possible to observe the effect of flow rate on the formation of CA-PEO fibers in the SEM micrographs.

Furthermore, the type of sample formed (film or fiber) and the differentiation in fiber diameter were evaluated by varying the flow rate and PEO mass concentration (3 and 5 wt%) according to Table 4.1.

Table 4.1 - Type of CA-based sample formed after SB-Spinning and the respective CA-PEO fiber diameter with PEO mass variation

Samples	Type of sample	Fiber diameter (nm)
Neat CA_3.5	Film	-
Neat CA_7.0	Film	-
Neat CA_10.0	Film	-
CA_PEO 0.04_3.5	Film and low fiber production	-
CA_PEO 0.04_7.0	Film and low fiber production	-
CA_PEO 0.04_10.0	Film and low fiber production	-
CA_PEO 0.08_3.5	Defective fibers	-
CA_PEO 0.08_7.0	Defective fibers	-
CA_PEO 0.08_10.0	Defective fibers	-
CA_PEO 0.24_3.5	Defect-free fibers	385 ±100
CA_PEO 0.24_7.0	Defect-free fibers	339 ±73
CA_PEO 0.24_10.0	Defect-free fibers	314 ±68
CA_PEO 0.40_3.5	Defect-free fibers	615 ±124
CA_PEO 0.40_7.0	Defect-free fibers	645 ±115
CA_PEO 0.40_10.0	Defect-free fibers	667 ±127

Statistical analyses showed that only PEO mass concentration had a significant effect on the CA fiber diameter ($p < 0.001$), as demonstrated by the mean and standard deviation values described in Table 4.1. Therefore, in this study, there was no significant effect on CA fiber diameter caused by flow rate ($p = 0.450$), or by the interaction between flow rate and PEO mass concentration ($p = 0.182$). Thus, a new regression model was adjusted considering only the effect of PEO mass concentration and assuming a linear relationship. According to the adjusted model, for each unit increase in PEO concentration, there is an

increase of 113.3 nm in fiber diameter, considering $R^2=0.77$ and a model mean error of 63.4 nm.

From the data obtained, physicochemical hypotheses were raised to obtain CA-PEO fibers using the SB-Spinning method, as illustrated in Figure 4.2.

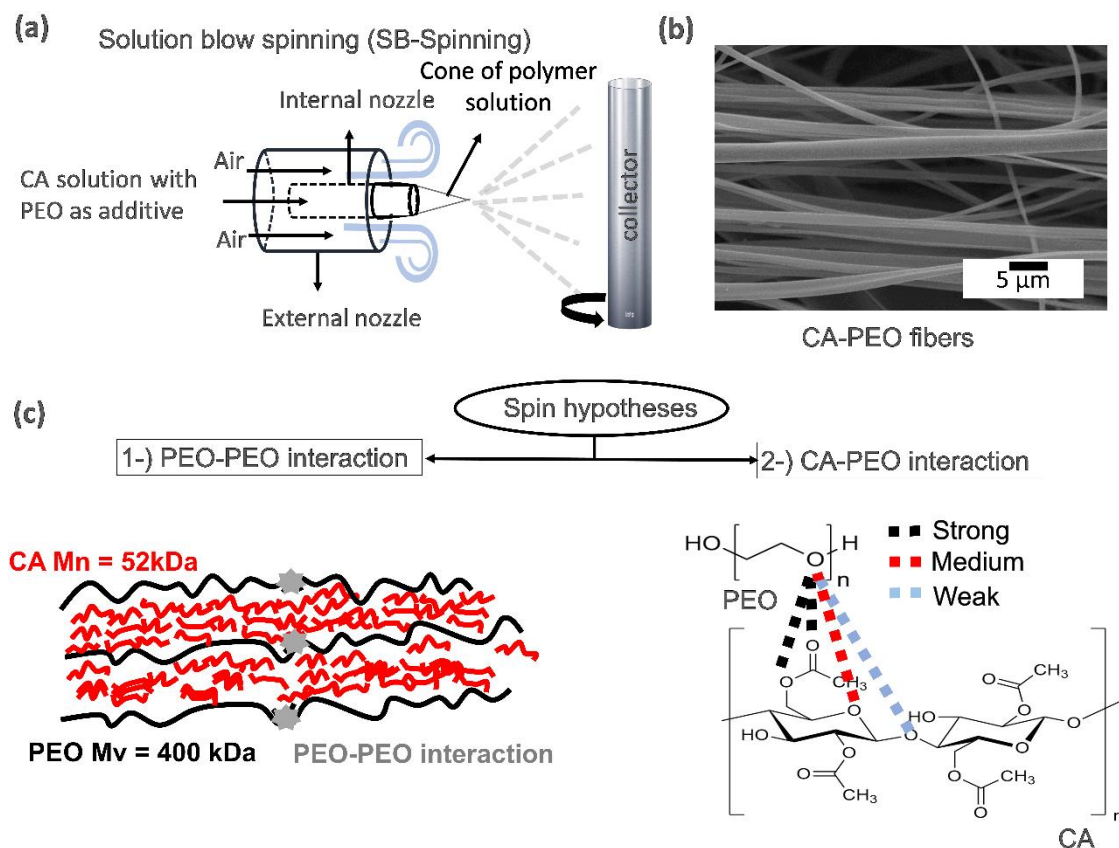


Figure 4.2 - a) Schematic representation of the SB-Spinning technique. b) SEM image of CA-PEO fibers. c) Possible interactions between CA and PEO during fiber formation, whose strength may vary according to spin hypotheses.

Figure 4.2a shows a schematic representation of the SB-Spinning method with formation of the polymeric solution cone and subsequent spinning of the CA-PEO fibers with the aid of turbulent air flow between the nozzles with mat deposition on the collector, and Fig. 4.2b highlights a microphotograph of the CA-PEO fibers. From the fibers obtained, two hypotheses were raised for spinning the solution containing CA-PEO, as shown in Figure 4.2c:

- 1) PEO-PEO molecular interaction due to the size of PEO chains ($M_v=400$ kDa) compared with that of CA chains ($M_n=52$ kDa), according to the molecular entanglement theory;
- 2) the possible stronger chemical interactions between the PEO oxygen and the oxygen contained in the acetate group, and the possible weaker chemical interactions between the PEO oxygen and the oxygen contained in the D-glucopyranose ring and in the glycosidic bond.

In order to test the hypotheses raised, first, the CA-PEO chemical interaction was investigated through the FTIR spectra for both the CA films and the CA-PEO mats compared to PEO spectra, as illustrated in Figure 4.3.

A shift in the bands assigned to the acetate groups was observed with varying PEO in the fiber composition, as also reported for the chitosan-collagen system [183]. The greatest displacements induced by PEO were verified in the C-O-C (12 cm^{-1}) and C=O (7 cm^{-1}) stretching bands of the CA acetate groups (Figs. 4.3c, d and e). In contrast, PEO interaction with the D-glucopyranose ring and the glycosidic bond was less significant, since the shift in the corresponding C-O-C vibration bands were only of 5 and 2 cm^{-1} , respectively (see Figs. 4.3a, b and e). The C-O-C group characteristic of PEO appears next to the glycosidic group of CA, presenting a slight approximation between these bands with PEO addition, as shown in Figure 4.3b.

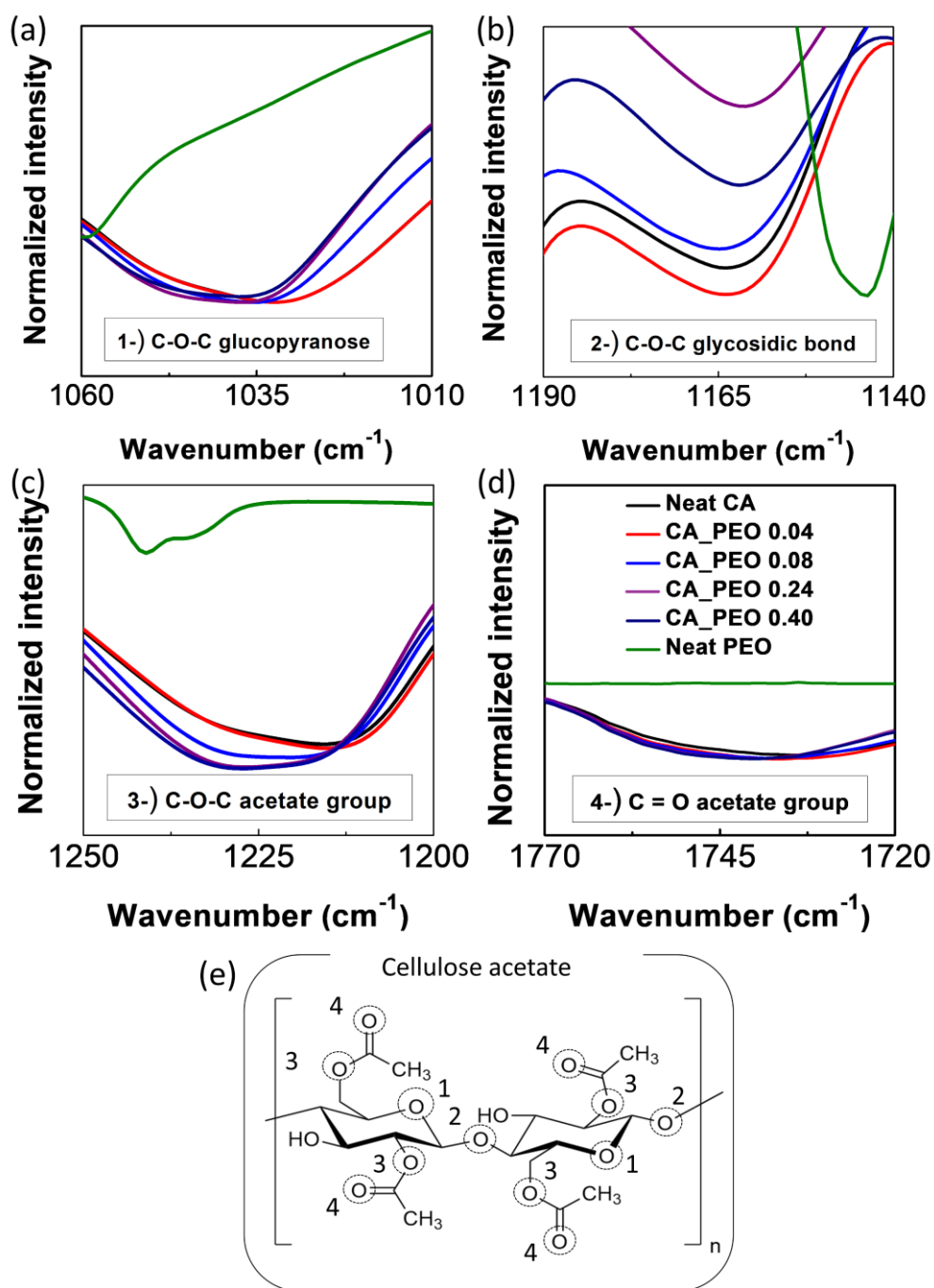


Figure 4.3 - FTIR spectra for PEO groups and CA groups that interact with PEO: (a) C-O-C from D-glucopyranose ring; (b) C-O-C from glycosidic bond; (c) C-O-C from acetate group; (d) C=O from acetate group; (e) arrangement of the groups in the cellobiose monomer.

In order to prove the two interaction hypotheses (PEO-PEO and CA-PEO), Figure 4.4 shows the rheological data for neat CA, CA-PEO and neat PEO solutions.

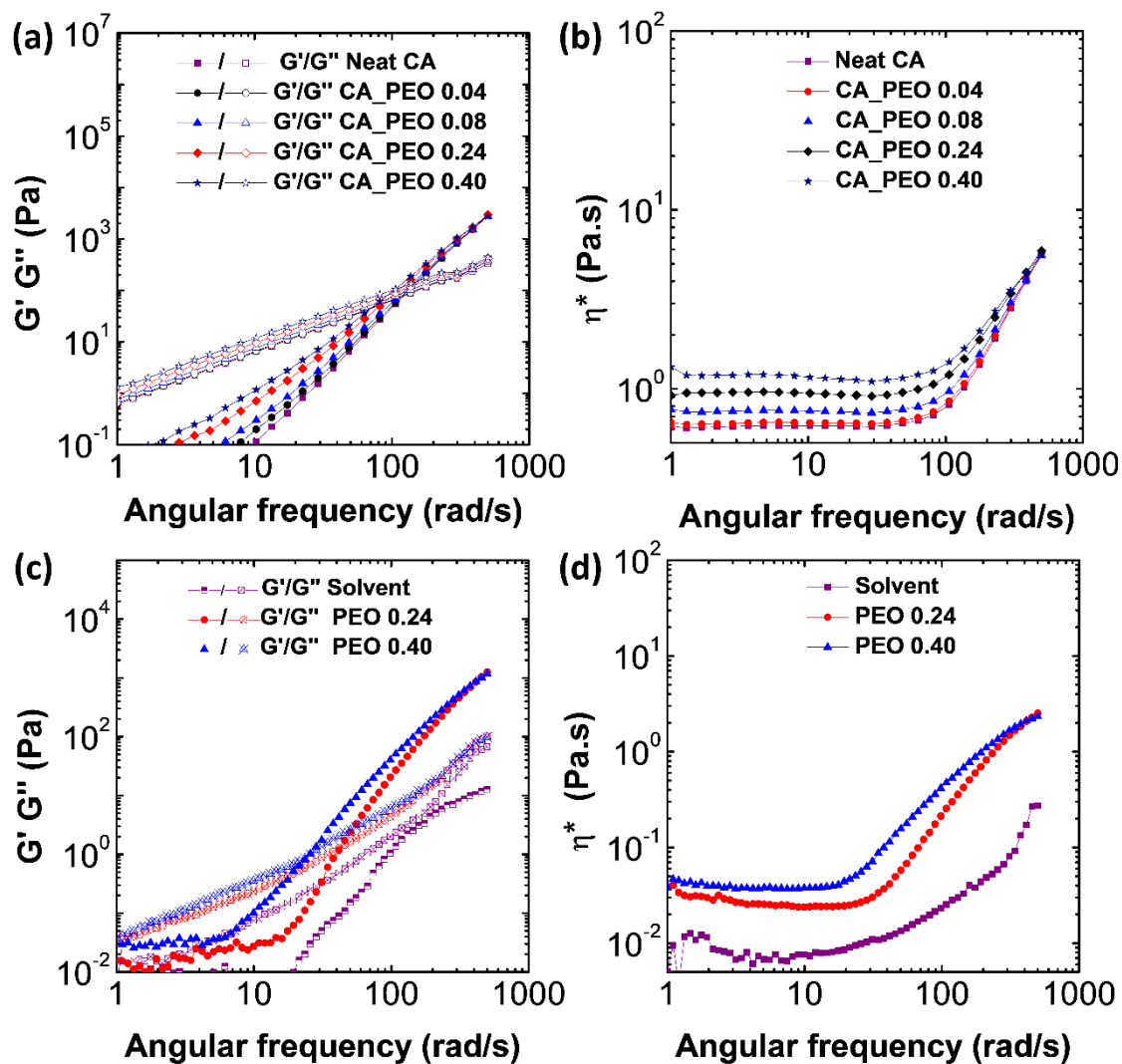


Figure 4.4 - Rheological diagrams of CA and CA_PEO solutions: (a) storage modulus (G')/loss modulus (G''); (b) complex viscosity (η^*). Rheological diagrams of PEO and solvents: (c) G'/G'' ; (d) η^* .

The increase in PEO concentration caused a decrease in the angular frequency at which the cross-over point of storage modulus (G') and loss modulus (G'') occurs for both CA-PEO system and PEO, as shown in Figures 4.4a and 4.4c, respectively. In addition, an increase in complex viscosity (η^*)

occurs for both CA-PEO system and PEO, as illustrated in Figures 4.4b and 4.4d, respectively. These observations indicate the CA-PEO and PEO-PEO molecular interactions [185], which would allow stretching of the chains to maintain adhesion and form defect-free fibers through the SB-Spinning process [186,187]. An empirical relationship has been established between the rheological properties and electrospinning process for fibers of linear and branched poly(ethylene terephthalate-co-ethylene isophthalate) (PET-co-PEI), where the polymer concentration required for electrospinning decreases with increasing the entanglement concentration (C_e) [188,189].

Aiming at a better understanding of the PEO chains in the formation of defect-free CA fibers, the PEO solutions without CA were spun using the same parameters as the samples of defect-free CA fibers. Morphology of the neat PEO spun is shown in Figure 4.5.

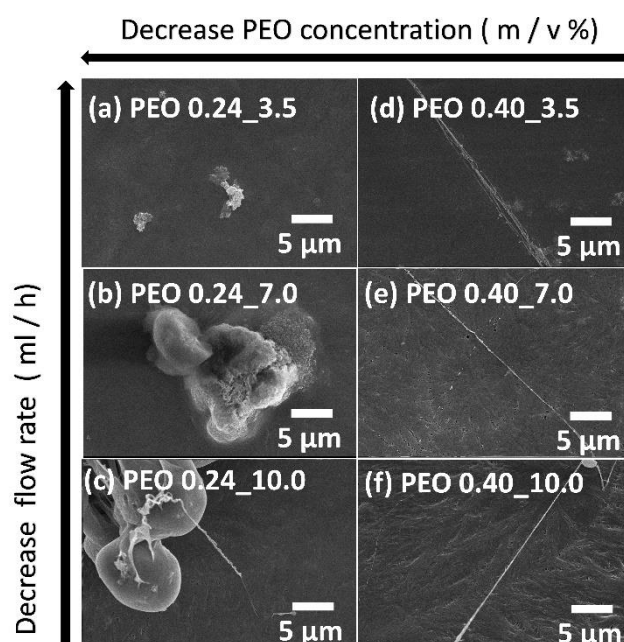


Figure 4.5 - Micrographs of pure PEO spun: (a) PEO 0.24_3.4; (b) PEO 0.24_7.0; (c) PEO 0.24_10.0; (d) PEO 0.40_3.5; (e) PEO 0.40_7.0; and (f) PEO 0.40_10.0.

The results revealed that no fibers were formed at the PEO_0.24 concentration, as shown in Figures 4.5a, 4.5b and 4.5c. In contrast, by increasing the PEO concentration, the PEO_0.4 samples presented formation

of PEO fibers without CA, indicating that PEO molecules with size $M_v=400$ kDa interact with each other in the absence of CA molecules and form fibers (Figs. 4.5d, 4.5e and 4.5f).

From the CA-PEO fibers formed, the CA_PEO_0.24 sample obtained at a flow rate of 10 ml/h was chosen for further studies because it produced a freestanding flexible mat with a larger number of fibers during 1 h, and this mat was well-defined, with smaller fiber diameter, and larger surface area for deacetylation reaction compared with the other mats.

4.1.2 Characterization of ICCMs

The optimized CA-PEO mat was deacetylated in alkali hydroxide solution in ethanol. Different alkali hydroxides were used to allow incorporation of alkaline ionic species (Li^+ , Na^+ , and K^+) that assist with the water retention process inside the cellulose mats (LiOH_mat, NaOH_mat, and KOH_mat, respectively) and are responsible for their improved electrochemical behavior [10].

Complete deacetylation of the CA-PEO fibers was confirmed by FTIR measurements, as shown in Figure 4.6.

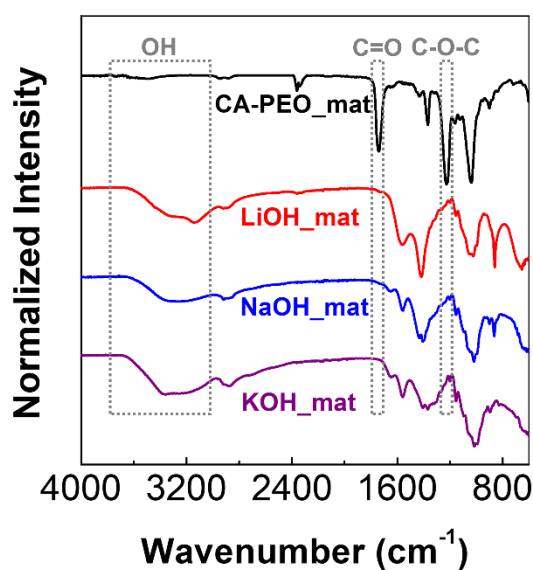


Figure 4.6 - FTIR spectra of CA-PEO mat before and after deacetylation using LiOH, KOH, and NaOH.

Disappearance of the bands related to the C=O (1735 cm^{-1}) and C-O-C (1226 cm^{-1}) groups, which are characteristic of acetate group, and the increased intensity (3360 cm^{-1}) of the bands characteristic to the OH group indicate the effective deacetylation of the mat using the three types of alkaline solutions, as previously reported for regenerated cellulose mats obtained by electrospinning [149,190]. The KOH_mat presented the highest band intensity related to the OH group, whereas the NaOH_mat spectrum showed the lowest band intensity, indicating the hypothetical effects of the alkali hydroxides on the degree of deacetylation and/or the amount of water adsorbed on the ICCMs [191].

Thermal stability of the CA-PEO mat before and after deacetylation was assessed by TGA, as illustrated in Figure 4.7.

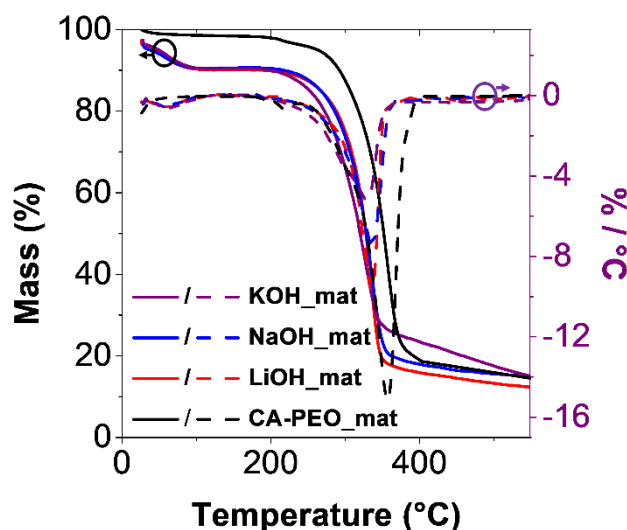


Figure 4.7 - TGA and derivative thermal gravimetry (DTG) of the CA-PEO mat before the deacetylation process and of the ICCMs after deacetylation using LiOH, KOH, and NaOH.

Regardless of the alkali hydroxides used in deacetylation, the different ICCMs showed very similar thermal behavior. The ICCMs presented an initial weight loss of nearly 5% up to $100\text{ }^{\circ}\text{C}$, which was associated with water vapor desorption. The KOH_mat showed the largest amount of desorbed water (5.73

wt%), followed by the LiOH_mat (5.25 wt%), and the NaOH_mat (4.58 wt%), with values compatible with the FTIR spectra. The ICCMs were thermally stable up to ≈ 270 °C, presenting the following onset temperature of thermal degradation (T_{onset}): LiOH_mat (277 °C), NaOH_mat (273 °C) and KOH_mat (262 °C), and variation of ≈ 15 °C at the cellulose T_{onset} in relation to the ionic salts used in the deacetylation process. In addition, the deacetylation process reduced the thermal stability of the ICCMs by ≈ 35 °C compared with the T_{onset} of the CA-PEO mat (315 °C), and produced cellulose fibers that were more hydrophilic than the CA-PEO fibers (1.12 wt% of desorbed water). The characteristic thermal degradation peak for PEO at -210 °C [192] appeared only in the CA-PEO mat curve, indicating a possible removal of this additive during the deacetylation process. A marked weight loss occurs at higher temperatures due to the decomposition of cellulose [69] and CA [193].

Moreover, deacetylation induced recrystallization of the cellulose fibers, as observed in the XRD diagrams presented in Figure 4.8.

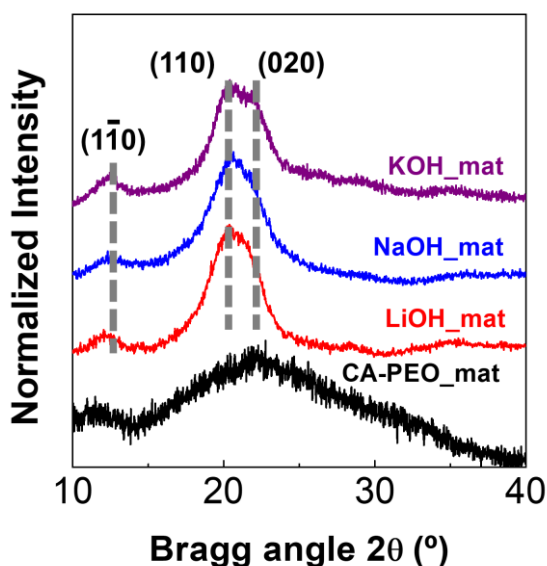


Figure 4.8 - XRD diagrams of CA-PEO mat before and after deacetylation using LiOH, KOH, and NaOH in ethanol solution.

Because the CA-PEO mat is totally amorphous, the deacetylation process resulted in regenerated crystalline cellulose fibers that showed

characteristic peaks at $2\theta=12.5^\circ$ ($1\bar{1}0$), $2\theta=20^\circ$ (110) and $2\theta=22^\circ$ (020), corroborating the results reported by French [194]. The ICCMs presented the following Segal crystallinity indexes [195]: LiOH_mat (30%), NaOH_mat (23%), and KOH_mat (21%), indicating a direct relationship between the crystallinity index and cation radius, and an almost inverse relationship between the crystallinity index and the water adsorption proposed in the TGA and FTIR results. Nevertheless, the greater thermal stability of the amorphous CA related to the regenerated crystalline cellulose fibers may be associated with the effect of the chemical deacetylation process on cellulose degradation, which the residual cation affects the thermal stability of polysaccharides [196].

The hypothesis raised in the TGA for the possible removal of PEO during deacetylation was confirmed by the morphological changes observed on the surface of the CA-PEO fibers immersed only in water for 4 h, as reported in the literature on PEO solubility in water [197], and shown in Figure 4.9.

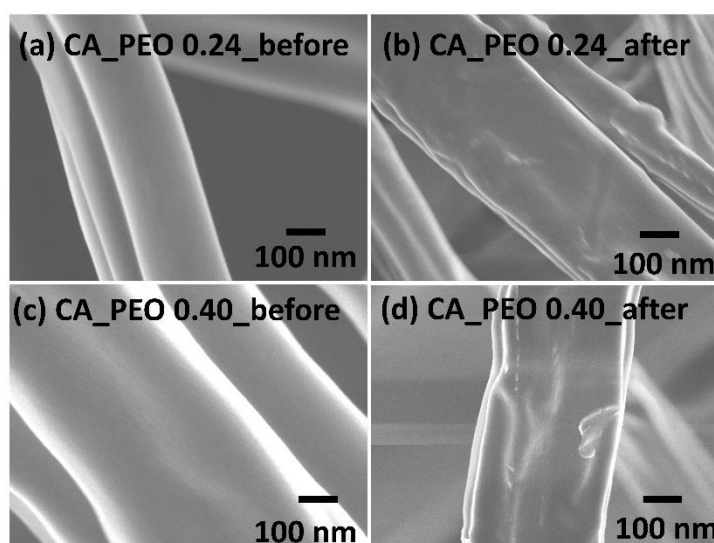


Figure 4.9 - SEM micrographs of CA-PEO fibers before and after water immersion: (a) CA_PEO 0.24_before; (b) CA_PEO 0.24_after; (c) CA_PEO 0.40_before; (d) CA_PEO 0.40_after.

Alkali hydroxides in aqueous medium had an even greater influence on the diameter and morphology of the ICCM fibers compared with those of the fibers immersed only in water, possibly removing the surface PEO from these

fibers, as illustrated in Figure 4.10. Figure 4.10 also shows the XPS and EDS results for verification of the salt ions infiltrated in the fibers and the profile analysis for assessment of roughness and specific surface defects.

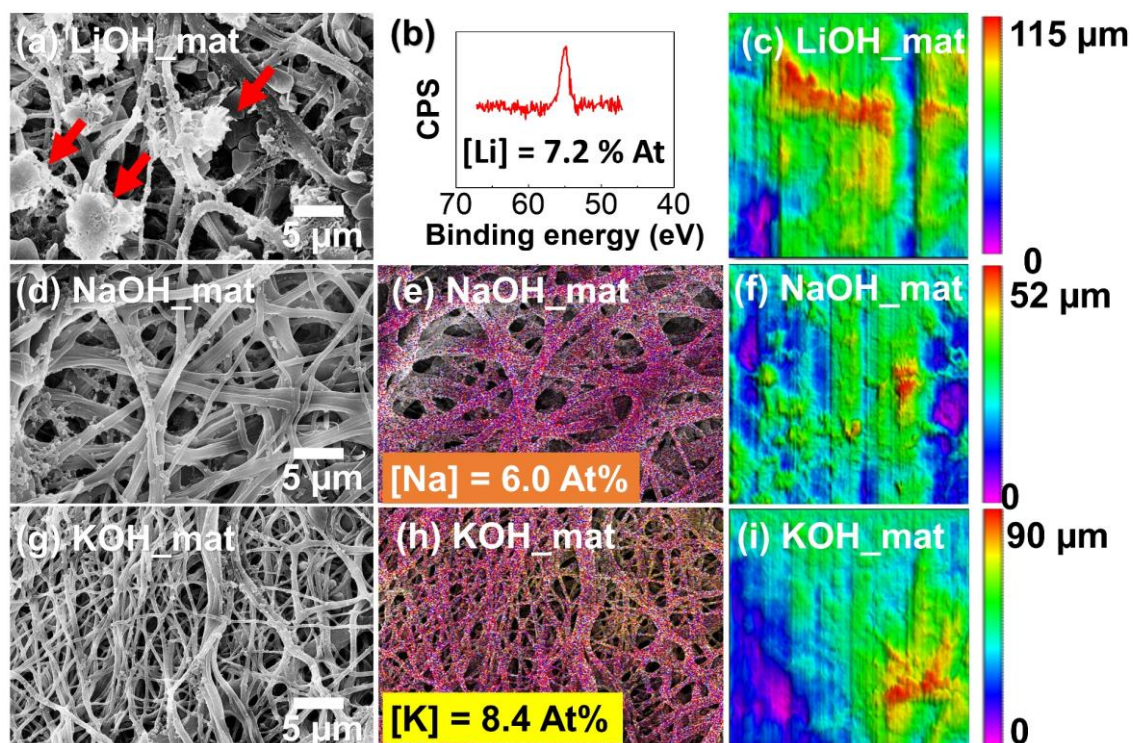


Figure 4.10 - Influence of the alkali hydroxides on the surface properties of the ICCMs: (a) SEM images of (a) LiOH_mat, (d) NaOH_mat, and (g) KOH_mat. (b) XPS of LiOH_mat. EDS mapping, where purple is carbon, blue is oxygen, and yellow is the metallic ions of (e) NaOH_mat and (h) KOH_mat. 3D profile for (c) LiOH_mat, (f) NaOH_mat, and (i) KOH_mat with color scale bar roughness intensity.

The NaOH_mat exhibited the largest diameter of cellulose fibers, reaching 524 ± 103 nm, compared with those of the LiOH_mat (314 ± 41 nm) and KOH_mat (345 ± 53 nm), which maintained the diameter of the cellulose fibers similar to that of the CA-PEO fibers before the deacetylation process (Figs. 4.10a, d and g). In addition, the LiOH_mat showed a partial rupture of the fibers, indicating a possible dissolution of cellulose due to the alkali hydroxide [198], as shown by the narrow straight lines in Figure 4.10a. XPS and EDS analyses confirmed an uniform incorporation of alkaline ionic species along the

fibers (Figs. 4.10b, e and h). The NaOH_mat presented the smallest root mean square (RMS) surface roughness (7.7 μm) with uniform 3D profile topography, followed by KOH_mat (16.9 μm) and LiOH_mat (19.6 μm). The roughness and homogeneity of the NaOH_mat surface may be associated with the larger diameter of the cellulose fibers, making the ICCM more compact, whereas the roughness and heterogeneity of the LiOH_mat surface may be associated with the partial rupture of the cellulose fibers.

Electrochemical response of the ICCMs was assessed by electrochemical impedance spectroscopy (EIS) and cyclic voltammetry (CV) using a typical capacitor structure (Al/ICCM/Al), as shown in Figure 4.11.

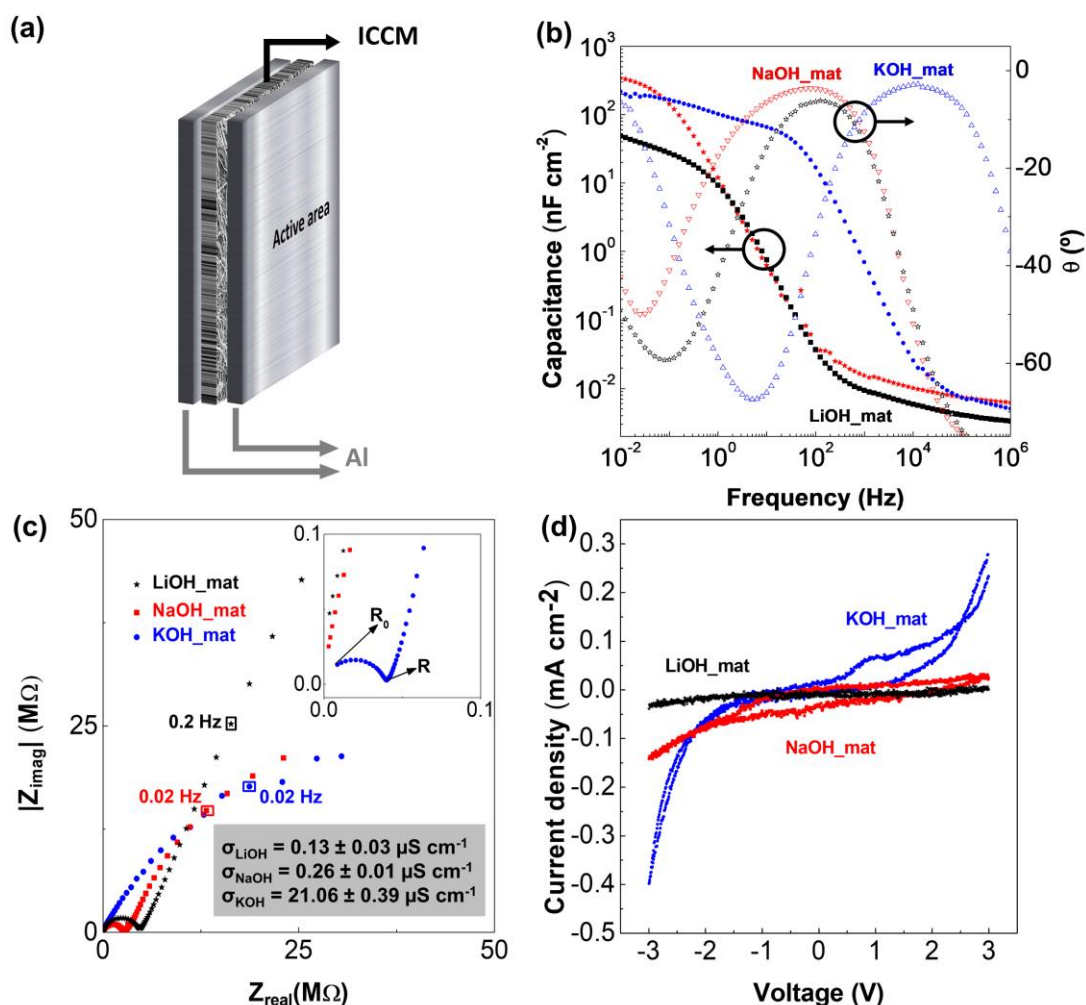


Figure 4.11 - (a) Schematic representation of the electrochemical cell with the ICCM. (b) Capacitance and phase angle vs. frequency for the LiOH, NaOH and KOH cellulose mats and their respective (c) Nyquist plots (inset: ionic

conductivity for each ICCM). (d) Cyclic voltammetry (CV) measurements of the LiOH, NaOH and KOH cellulose mats from -3 to 3 V at 400 mV/s.

The capacitance-frequency measurements and their respective Nyquist plots are presented in Figures 4.11b-c. The capacitance of the ICCMs increased for low frequencies due to formation of EDLs in the dielectric-metal interfaces formed by mobile ionic species within the cellulose matrix. The ICCMs show a capacitive regime varying between 60 Hz (KOH_mat) and 0.3 Hz (NaOH_mat) for phase angle $<45^\circ$, which is consistent with the literature [73,199,200]. The ICCM deacetylated with KOH exhibited capacitive behavior over a wider frequency range (60 - 0.2 Hz) than those deacetylated with LiOH and NaOH, reaching a capacitance value of 82 nF cm² at the minimum phase angle located at 5 Hz. LiOH_mat and NaOH_mat showed capacitance values of 32 and 300 nF cm², respectively, at the minimum phase angle, evidencing the effect of the alkaline cations on EDL formation and capacitance values.

Ionic conductivity (σ) of the ICCMs was determined according to Equation 4.1:

$$\sigma = \frac{l}{A(R-R_0)} \quad \text{Eq. 4.1}$$

in where l is the thickness of the ICCMs; A is the surface area of each aluminum electrode deposited on the cellulose mat, which corresponds to 1 mm² (Fig. 4.11a); R is the mass electrical resistance and R_0 is the electrode resistance, both determined through the Cole–Cole plot [11,200,201] shown in Fig. 4.11c, with values presented in Table 4.2.

Table 4.2 - Detailed information on the thickness, R and R_0 of each ICCM

ICCM	Thickness (μm)	R ($\text{M}\Omega$)	R_0 ($\text{M}\Omega$)
LiOH_mat	83 ± 11	5.014 ± 0.032	0.005 ± 0.001
NaOH_mat	106 ± 23	2.819 ± 0.410	0.004 ± 0.001
KOH_mat	71 ± 7	0.035 ± 0.005	0.004 ± 0.001

The KOH_mat showed the highest ionic conductivity, reaching $21.60 \pm 0.39 \mu\text{S cm}^{-1}$, followed by NaOH_mat ($\sigma_i = 0.26 \pm 0.01 \mu\text{S cm}^{-1}$) and LiOH_mat ($\sigma_i = 0.13 \pm 0.03 \mu\text{S cm}^{-1}$). In Figure 4.11d, stronger hysteresis can be observed for the KOH_mat, with polarity reversal in the charge current. Compared with the LiOH and NaOH mats, the KOH infiltrate exhibited a more complete charging of the aluminum electrodes [202].

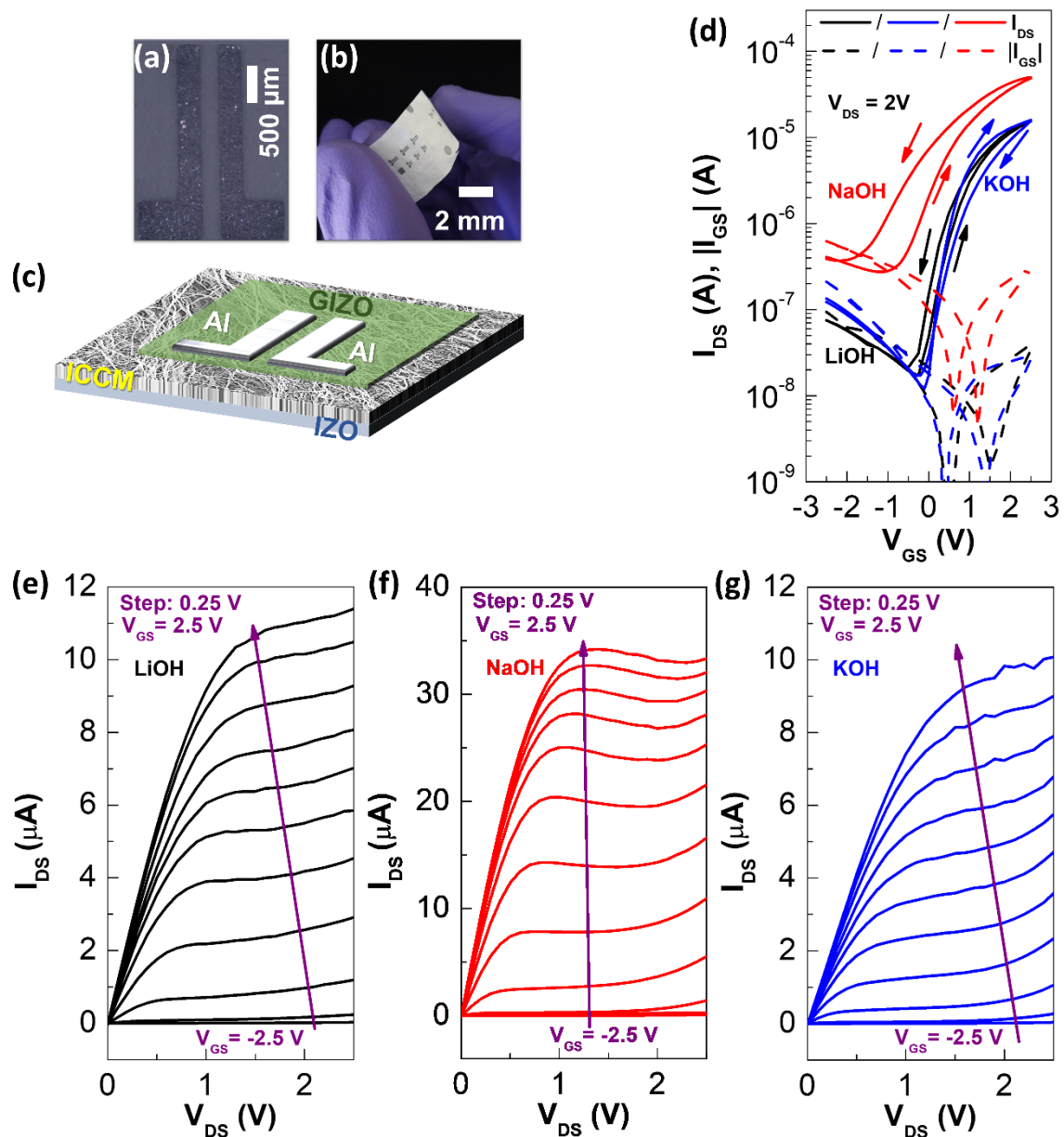
The higher values of ionic conductivity and CV behavior of the KOH_mat may be associated with the greater amount of water infiltrating its structure, forming a hydrolyzed shell, as indicated in by FTIR and TGA. The presence of water assists with ionic conductivity [10], favoring the formation of EDLs as a result of water dissociation, providing the fibrillar structure with H^+ and OH^- ions [203]. In addition, the roughness, structure homogeneity and fiber diameter of the ICCMs proposed in the 3D profile can also affect the ionic conductivity and formation of EDLs on NaOH_mat and LiOH_mat, as previously reported for smooth and compact micro- and nano-fibrillated cellulose paper [11]. In other words, the previously listed results suggest that water and type of alkaline ions are main factors that determine the electrochemical properties of the ICCMs.

Thus, the ICCMs exhibit suitable electrochemical properties to be applied simultaneously as solid-state electrolyte and substrate for flexible electronics.

4.1.3 Electrical performance of ICCMs as dielectric and substrate in oxide-based FETs

Figure 4.12 shows the FETs on the ICCMs and the results obtained from the transistors according to the types of ions infiltrated in the fibers.

Figure 4.12 - (a) Optical photomicrograph of a transistor. ICCM as "interstrate" layer in a FET: (b) photograph and (c) schematic illustration. (d) Influence of salt ions on cyclic transfer characteristic curves of the FETs, where solid and dashed lines correspond to drain (I_{DS}) and leakage (I_{GS}) currents, respectively. The output curves with purple arrows represent the sweep direction for each ionic salt: (e) LiOH; (f) NaOH, and (g) KOH.



Figures 4.12a-c shows a schematic representation and optical images of the GIZO FETs fabricated on ICCM as "interstrate" layer. The GIZO semiconducting channel and the Al electrodes were designed using shadow masks with channel width (W) of $1500\ \mu\text{m}$ and channel length (L) of $150\ \mu\text{m}$ ($W/L=10$). The cyclic transfer characteristic curves ($I_{\text{DS}}-V_{\text{GS}}$) and the respective output voltage curves ($I_{\text{DS}}-V_{\text{DS}}$) are shown in Figures 4.12d-g. Electrical parameters including ON/OFF current modulation ($I_{\text{ON/OFF}}$), activation voltage (V_{ON}), transconductance ($g_m = \partial I_{\text{DS}} / \partial V_{\text{GS}}$), subthreshold slope (S_s), and saturation mobility (μ_{Sat}) were determined in the forward scan direction in the saturation

regime ($V_{DS}=2V$). The last two parameters were determined according to Equations 4.2 and 4.3, respectively:

$$SS = \left(\frac{\partial \text{Log} I_{DS}}{\partial V_{GS}} \Big|_{max} \right)^{-1} \quad (\text{Eq. 4.2})$$

$$\mu_{Sat} = \left(\frac{\partial \sqrt{I_{DS}}}{\partial V_{GS}} \right)^2 \frac{2L}{WC} \quad (\text{Eq. 4.3})$$

Where: I_{DS} is the drain current, V_{GS} is the gate voltage, C is the capacitance of the ICCM, and W ($\sim 1500 \mu\text{m}$) and L ($\sim 150 \mu\text{m}$) are the width and length of the channel, respectively.

The FETs presented a typical n type behavior, low operating voltage (< 2 V) in the ON state for $V_{GS} < 0$ V, high I_{DS} of up to $30 \mu\text{A}$ for $V_{GS} = 2$ V, and gate leakage current between 10^{-6} and 10^{-8} A. The values extracted from the characteristic curves of the FETs are described in the Table 4.3.

Table 4.3 - Electrical parameters of GIZO FETs fabricated on distinct ICCMs applied as “interstrate” layer. The values show the mean and respective standard error of the mean obtained from ten devices.

ICCM	V_{ON} (V)	$I_{ON/OFF}$ ($\times 10^3$)	g_m (μS)	S_s (V / dec)	μ_{Sat} ($\text{cm}^2 \text{V}^{-1} \text{s}^{-1}$)
LiOH_mat	-0.2 ± 0.2	0.84 ± 0.06	9.0 ± 0.1	0.37 ± 0.03	22.8 ± 2.8
NaOH_mat	-1.4 ± 0.3	0.22 ± 0.15	2.6 ± 0.1	0.64 ± 0.12	3.9 ± 0.8
KOH_mat	-0.2 ± 0.1	1.30 ± 0.10	9.6 ± 0.1	0.23 ± 0.01	13.9 ± 0.1

The electrical parameters described in Table 4.3 indicate that the LiOH and KOH FETs showed useful characteristics, whereas the performance of the NaOH FET presented a distinct characteristic. The KOH FETs showed slightly better performance than the LiOH FETs, with greater electrical modulation of three orders of magnitude, higher g_m that reached nearly $10 \mu\text{S}$, S_s lower than 0.3 V dec^{-1} , and intermediate μ_{Sat} ($14 \text{ cm}^2 \text{V}^{-1} \text{s}^{-1}$). Performance of the KOH FETs was similar to those of the GIZO FETs fabricated on office paper ($I_{ON/OFF} = 10^3 - 10^4$; $S_s = 0.8 \text{ V dec}^{-1}$) [74] and considerably inferior to that on nanopaper ($I_{ON/OFF} = 10^4 - 10^5$; $S_s = 2 \text{ V dec}^{-1}$) [72]. In contrast, the NaOH_mat

FETs showed a shift in cyclic transfer characteristics, with apparently higher S_s , lower μ_{sat} , and higher $|I_{GS}|$ current compared with the values of the LiOH_mat and KOH_mat transistors (Fig. 4.12d and Table 4.3). In addition, the output voltage curves of the NaOH_mat FETs presented higher I_{DS} values compared with those of transistors fabricated on LiOH_mat and KOH_mat, which showed similar I_{DS} values, as illustrated in Figures 4.12e-g. The performance of the NaOH FETs may be associated with formation of EDL at lower frequencies, even if the larger contact surface between the fibers promotes smaller defects on the NaOH_mat (Figure 4.10).

According to our analysis of the NaOH_mat FET, the greater contact between the fibers probably enables the occurrence of a high gate leakage current. This event is dominated by the displacement in current, that is, a current that flows to the electrode through the external circuit when the ions are displaced to the mat interface to form the EDLs. Higher contact between the fibers means that ionic displacement may occur not only in the fibers, but also between them. This results in a greater ionic current flow within the mat when EDLs are formed and, consequently, greater current flow through the external circuit to compensate for it. Thus, the I_{OFF} current of the transistor is limited by the I_{GS} current, which is dominated by the ionic current. As a result, the S_s ends up being affected by the higher I_{OFF} current. In addition, the higher intensity of the I_{DS} current ends up being a result of the lower surface roughness of the NaOH_mat, thus allowing better formation of the GIZO film on the fibers.

The KOH_mat transistors maintained their functionality in the bending mode with up to 15 mm in-plane radius, and stopped functioning at 15 mm out-plane radius and after 15 mm bending radius on the flat mode after bending, as shown in Figure 4.13.

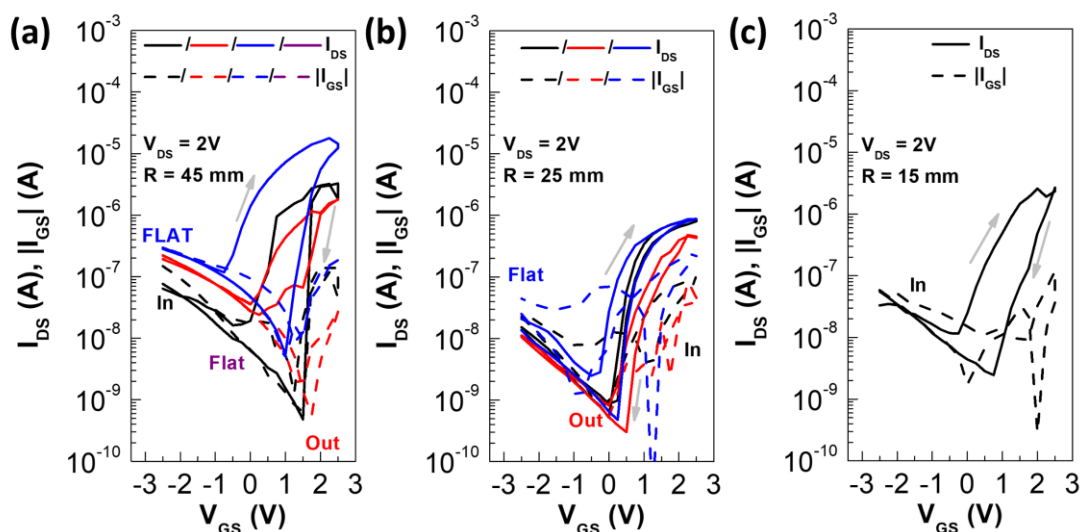


Figure 4.13 - Influence of ICCM in- and out-plane bending radius on the cyclic transfer characteristic curves of FETs, where solid and dashed lines correspond to drain (I_{DS}) and leakage (I_{GS}) currents, respectively: (a) 45 mm, (b) 25 mm, and (c) 15 mm.

V_{ON} , $I_{ON/OFF}$ and S_s values increased slightly in the bending radius of 45 mm and were maintained close to the initial values in the flat mode until the bending radius of 15 mm, as described in Figure 4.14.

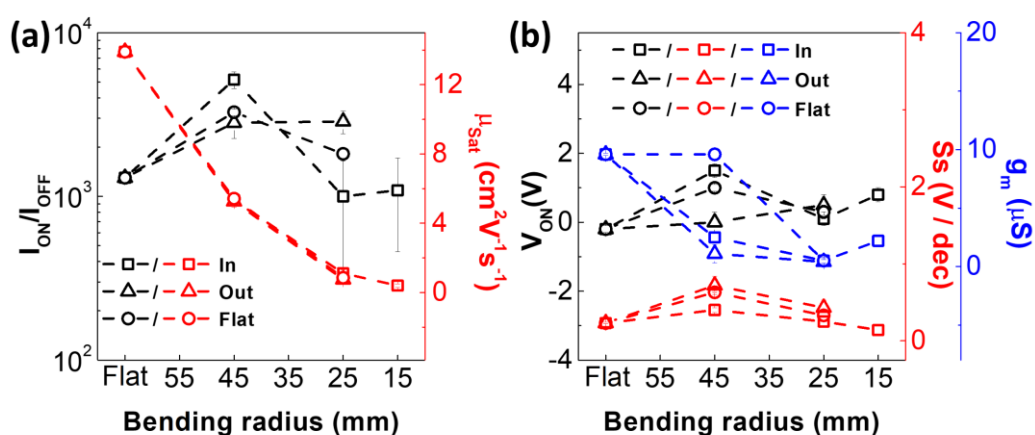


Figure 4.14 - Influence of ICCM in- and out-plane bending radius on the electrical parameters of the GIZO FETs: (a) $I_{on/off}$ and μ_{Sat} and (b) V_{ON} , S_s and g_m .

In contrast, the μ_{sat} and g_m values reduced with bending radius and did not recover in the flat mode until the FETs stopped functioning completely at the bending radius of 15 mm, as illustrated in Figure 4.13. Different V_{ON} , $I_{\text{ON/OFF}}$ and g_m values were observed in the flat mode after bending and the in- and out-plane bending modes. Therefore, FET performance may be hindered by modifying the structural network of cellulose fibers [204] and by cracks in the FET components after bending [205], as observed for cracks on the IZO films deposited on the ICCM fibers in Figure 4.15.

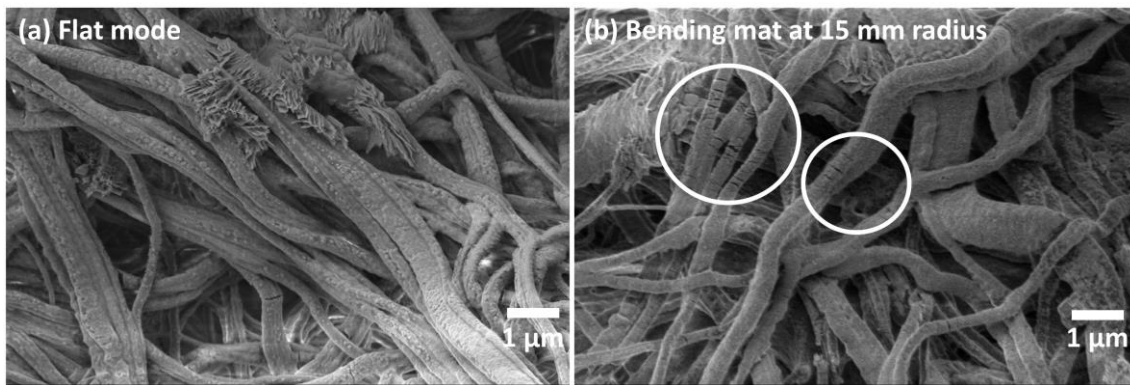


Figure 4.15 - IZO-covered ICCM: (a) flat mode and (b) bending mat at 15 mm radius with IZO cracks indicated by white circles.

4.1.4 Electrical performance of ICCMs as dielectric and substrate in pencil-drawn resistor-loaded inverters

Considering the performance of the GIZO FETs fabricated on the KOH_mat, these devices were integrated into resistor-loaded inverters as a proof of concept for integration of microelectronic devices simply by drawing graphitic tracks using a pencil that will define the load resistance (R_L), as shown in Figure 4.16.

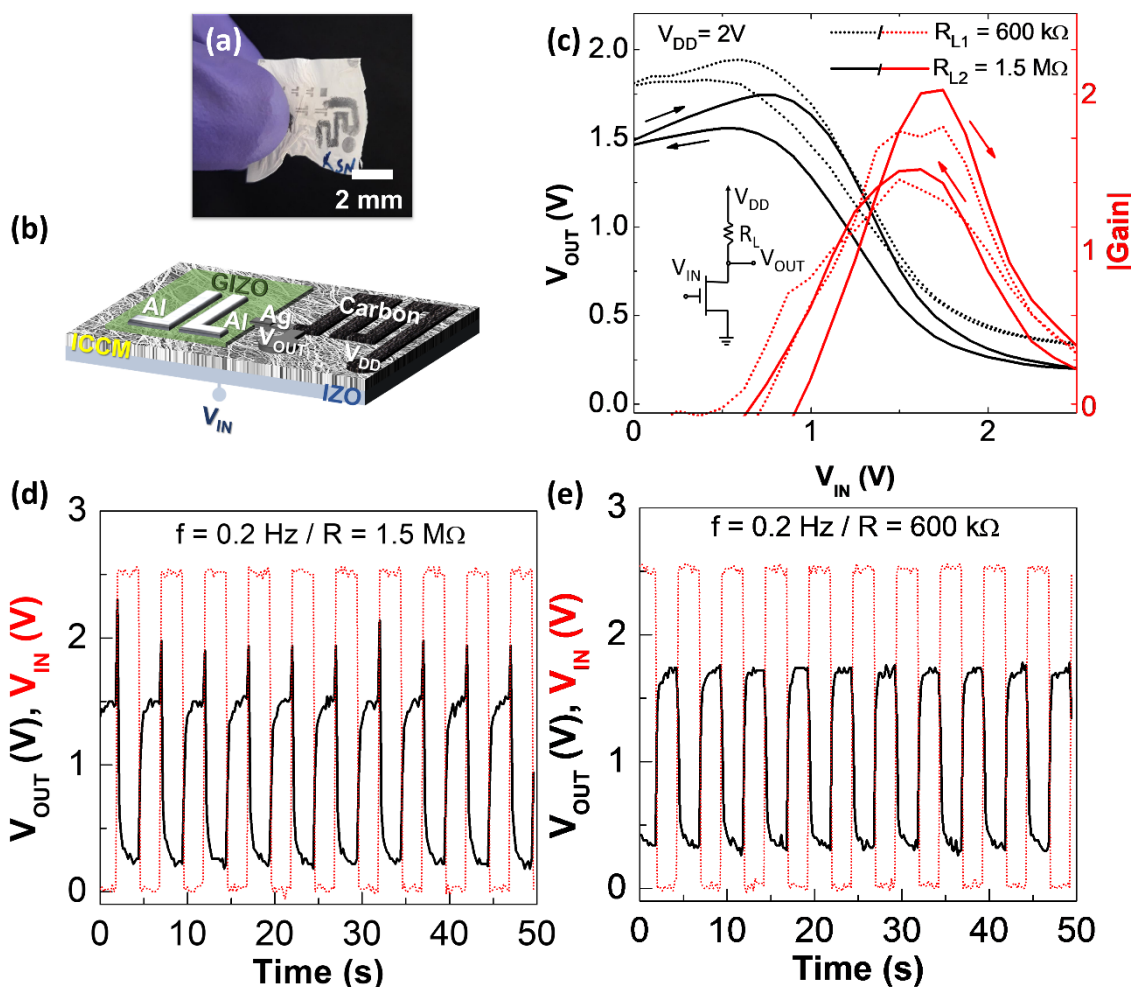


Figure 4.16 - (a) Photograph of ICCM as dielectric and substrate in pencil-drawn resistor-loaded inverters. (b) Schematic representation and photograph of KOH_mat as "interstrate" layer in an inverter. (c) Voltage transfer curve of the inverter on KOH_mat with a schematic representation of the circuit. Dynamic electrical characterization of the inverter on KOH_mat at 0.2 Hz using two resistances: (d) 1.5 MΩ and (e) 600 kΩ.

The electrical connections between the FET and the pencil-drawn resistors are standardized using a commercial rollerball silver conductive ink pen (Circuit Scribe). Figure 4.16b shows the schematic representation of this inverter.

Figures 4.16a-b show the schematic representation and photograph of the device, where two electrical resistances (600 kΩ and 1.5 MΩ) were drawn on the mat surface using an HB 2 pencil. These resistances were connected to

the FET electrodes using a rollerball silver conductive ink pen. The resistive load inverter showed the greatest gain of almost 2 at $V_{IN} \approx 1.7$ V and $V_{OUT} \approx 1.8$ V for a resistance of 1.5 M Ω , indicating that the increase in R_L causes a greater inverter gain, as illustrated in Figure 4.16c. The dynamic electrical characterization of the inverter indicated good dynamic performance of V_{OUT} in response to the 0.2 Hz V_{IN} pulses for both R_L values, as shown in Figures 4.16d-e. The dynamic response showed a decrease in charge/discharge from 1 to 3 Hz associated with the mobility capacity of the ions to form the EDL [206], as demonstrated in Appendix A. The increase in resistance also slightly decreases the dynamic response of the inverter up to a maximum operating frequency of 3 Hz.

4.2 LIGE from pineapple CNCs and CMC-based ink for flexible ZnO UV sensors

4.2.1 LIG obtained from pineapple CNCs

Aiming not only at the application of cellulose as a substrate and dielectric, this second approach shows the results obtained from LIG applied as an electrode in ZnO UV sensors obtained from the CNCs of the PALFs with subsequent formulation of CMC-based, obtaining more LIG from CMC.

Initially, a study on the laser parameters was carried out to obtain the most conductive LIG from pineapple CNCs to formulate CMC-based inks to be applied as electrode in UV ZnO sensors. Figure 4.17 shows images of different colors on the CNC tablets before and after laser passing, as well as the nanostructures of the CNCs before and after laser passing, indicating a possible LIG formation on these materials by varying the laser focus, laser power and tip speed parameters.

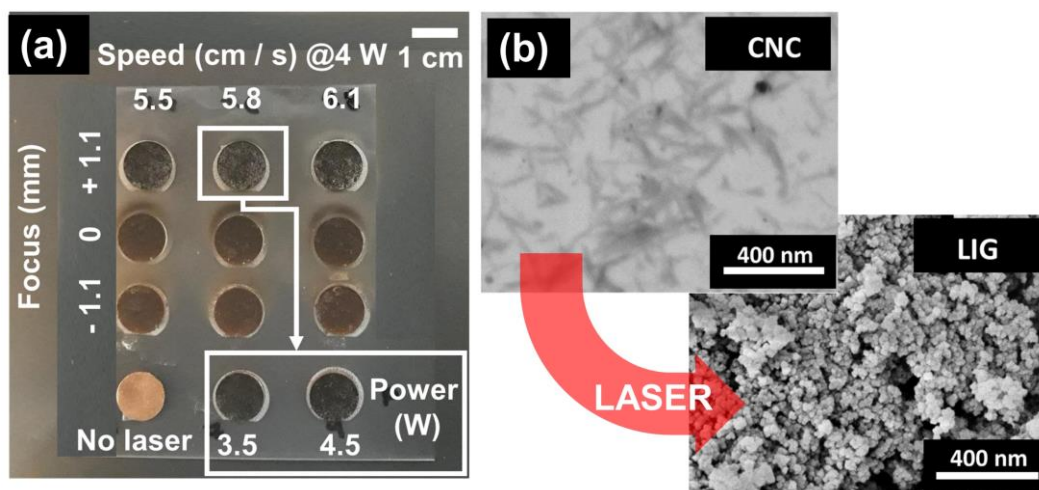


Figure 4.17 - LIG obtained from pineapple CNC tablet. (a) Photograph of CNC tablet before laser passing and photographs of several LIG on CNC tablet, varying laser focus, laser power, and tip speed. (b) CNC “whiskers” before laser passing and circular LIG nanoparticles after laser passing.

All CNC tablets darkened after laser passing, indicating possible LIG formation on the surface of all samples, as shown in Figure 4.17a. The samples obtained using a laser beam defocus of +1.1 mm became even darker than those produced under other conditions, indicating the possible formation of a greater amount of LIG for this condition. The CNCs extracted from the PALFs presented a shape similar to “whiskers”, with crystallinity index >90% [15], 34 ± 5 nm diameter, and 400 ± 100 nm length [16,17]. After laser passing on the CNC tablets, the laser beam modified the “whiskers” shape of the CNCs, forming possible circular LIG nanoparticles, as illustrated in Figure 4.17b.

Formation of LIG from CNC tablets under each laser condition is confirmed by the respective Raman spectra, as shown in Figure 4.18.

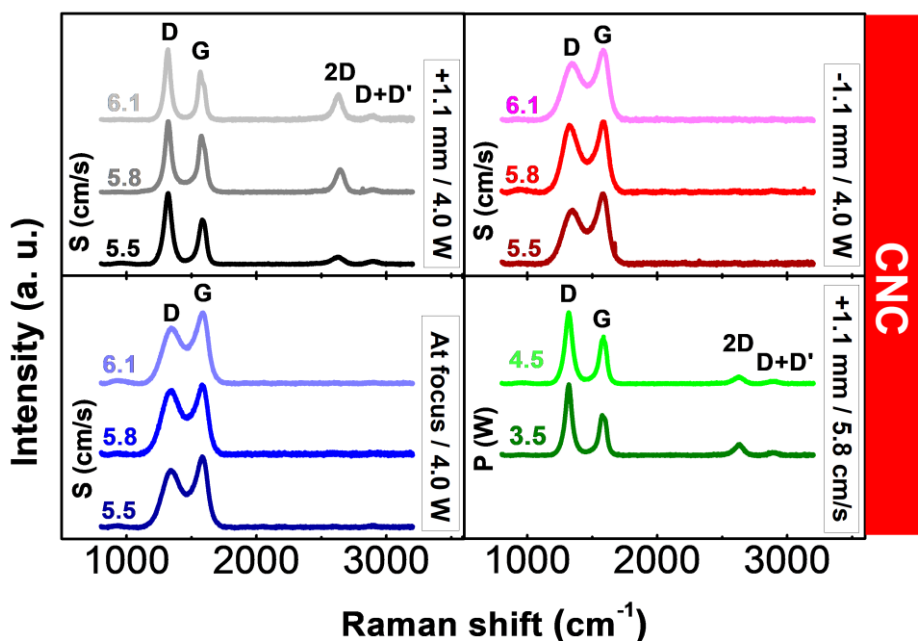


Figure 4.18 - Raman spectra of LIG synthesized from CNC tablet, varying laser focus, tip speed (S), and laser power (P).

The Raman spectra confirmed the formation of LIG nanoparticles from CNC under all laser parameter conditions, indicating by the D ($\approx 1318 \text{ cm}^{-1}$) and G ($\approx 1574 \text{ cm}^{-1}$) bands, characteristic of LIG,

Variation in the I_D/I_G and I_{2D}/I_G ratios, and full width at half maximum (FWHM) values in relation to the G band of each Raman spectrum laser condition are represented in Figure 4.19.

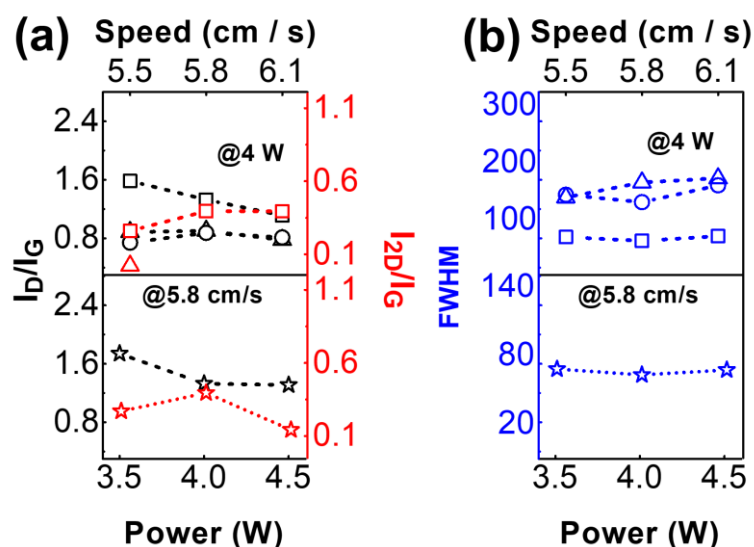


Figure 4.19 - (a) I_D/I_G and I_{2D}/I_G ratios with laser focus (\square/\square +1.1 mm, Δ/Δ at focus, \bigcirc -1.1 mm) (\star/\star +1.1 mm), laser speed, and laser power. (b) FWHM values for the G band in relation to with laser focus (\square +1.1 mm, Δ at focus, \bigcirc -1.1 mm) (\star +1.1 mm), laser speed, and laser power.

Variations in the I_D/I_G and I_{2D}/I_G ratios after appearance of the 2D (≈ 2645 cm^{-1}) band for some conditions indicate the effect of the laser parameters on the physical characteristics of LIG synthesized from CNC tablets, as illustrated in Figure 4.19a. FWHM values of the G band also varied with varying the laser parameters, indicating the physical changes in the LIG obtained from CNC [105], as it can be observed in Figure 4.19b.

Aiming to observe the electrical conduction of this formed LIG and correlate it with the color and Raman spectra, the sheet resistance values of the different structures formed using the laser parameters are described in Figure 4.20.

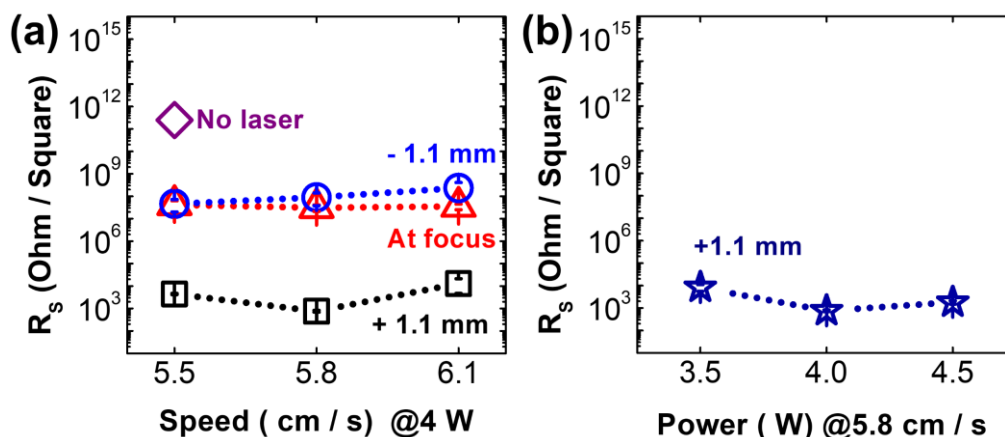


Figure 4.20 - LIG obtained from pineapple CNC tablet. Sheet resistance of LIG as a function of (a) tip speed and laser focus at constant laser power, and (b) laser power at constant laser focus and tip speed.

All samples presented sheet resistance values smaller than those of the no laser CNC tablets, which demonstrates that the formed LIG has different electrical conductivities in relation to the laser parameters (Figs 4.20a,b).

After laser passing with beam defocus of +1.1 mm, the LIG layers formed on the CNC tablets became darker and showed smaller sheet resistance compared with the other samples. These samples also showed 2D and D+D' ($\approx 2888 \text{ cm}^{-1}$) bands, indicating formation of conductive crystalline LIG [96] and showing the real disordered material that composes this LIG [207,208], respectively. In addition, the LIG obtained using a laser beam defocus of +1.1 mm presented $I_{2D}/I_G < 2$ and $I_D/I_G > 1$, indicating predominance of graphene multilayers containing defects [159] and small crystallites [209]. Smaller FWHM values for the G band as also observed to higher electrical conductivity LIG obtained from CNF [104].

The samples subjected to laser passing using the -1.1 mm defocus point and the focus point presented brownish (hazel) color and high sheet resistance. In this case, only the D and G bands appeared, indicating the absence of conductive crystalline graphene. $I_D/I_G < 1$ indicates the formation smaller defects for these conditions [209]. Variation in laser power and tip speed had less influence on sheet resistance, as well as on the appearance of the 2D and D+D' bands. The I_D/I_G ratios also showed no dependence on laser power and tip

speed, indicating a greater effect of the laser focus on electrical conductivity and type of LIG formed.

After laser passing with beam defocus of +1.1 mm, laser power of 4 W, and tip speed of 5.8 cm/s, the CNC tablets showed lower sheet resistance ($\approx 800 \Omega/\text{sq.}$) compared with the values of the other samples, suggesting that these were the best conditions to obtain LIG from CNC extracted from PALF. Therefore, these conditions were chosen to formulate the CMC-based ink.

4.2.2 LIGE obtained from CMC-based ink containing LIG from PALFs

Based on the LIG obtained from the CNC, two CMC-based ink formulations were prepared (LIG_0.6 and LIG_1.2), as well as a sample containing only CMC (LIG_0) in which the same parameters used for the CNC tablets to synthesize more LIG from CMC were investigated. The best condition for each ink composition containing LIG from CNC was chosen as the electrode used to fabricate the UV ZnO sensors.

The LIGE formed from the CMC-based ink formulations containing different concentrations of LIG from CNC were analyzed as a function of color and morphology of the induced microstructure, as shown in Figure 4.21 and Appendix B.

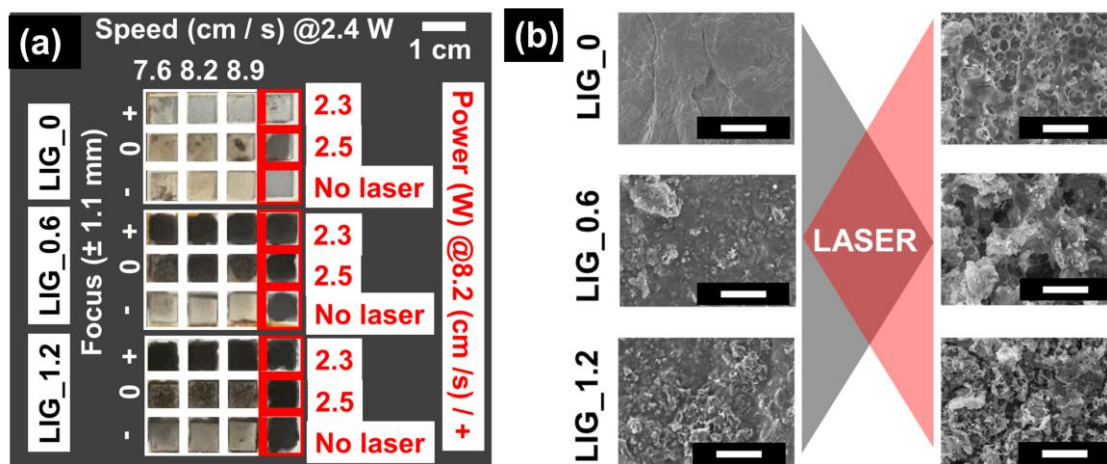


Figure 4.21 - LIGE synthesized from CMC-based ink containing LIG from CNC. (a) Photographs of LIG_0, LIG_0.6 and LIG_1.2 before and after laser passing, varying laser focus, tip speed, and laser power. (b) Photomicrographs of LIG_0, LIG_0.6 and LIG_1.2 before and after laser passing (white scale bar of 100 μm).

Variations in the laser beam focus and amount of LIG added to CMC-based ink formulation affected the final apparent color of the material after laser passing, with darker color suggesting that more graphene was synthesized, as it can be observed in Figure 4.21a. The more effective microstructural change undergone by the material is another indication of LIGE formation, as shown in Figure 4.21b and Appendix B.

The physical characteristics of the LIGE formed after laser passing on the ink were also investigated by Raman spectroscopy, similarly to the LIG obtained from the CNCs, as illustrated in Figure 4.22.

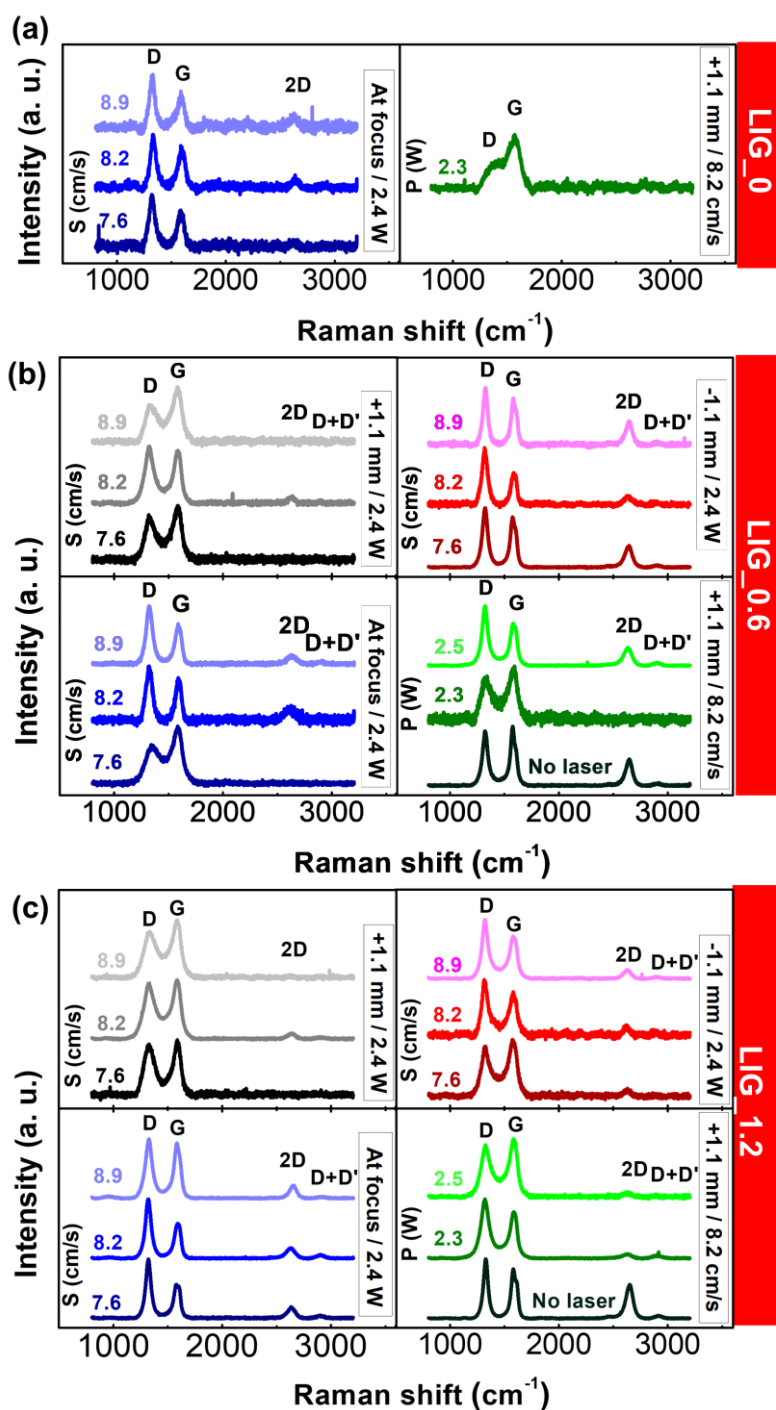


Figure 4.22 - LIGE synthesized from CMC-based ink containing LIG from CNC. Raman spectra of LIGE, varying laser focus, tip speed (S) and laser power (P), from the following LIG compositions: (a) LIG_0, (b) LIG_0.6, and (c) LIG_1.2.

Raman spectroscopy confirmed the formation of LIGE from CMC-based ink containing LIG in relation to color and microstructural changes with intensity

variation of the D, G, 2D and D + D' bands, as illustrated in Figures 4.22a-c. The respective I_D/I_G and I_{2D}/I_G ratios, and FWHM values in relation to the G band of each Raman spectrum laser condition are represented in Figure 4.23.

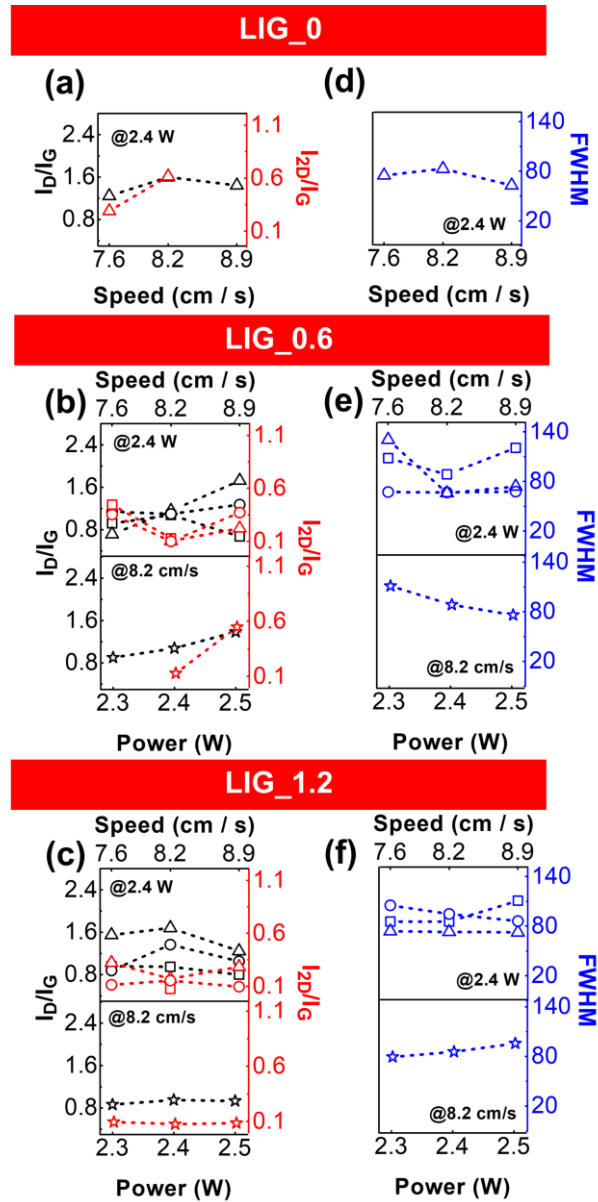


Figure 4.23 – I_D/I_G and I_{2D}/I_G ratios with laser focus (\square/\square +1.1 mm, Δ/Δ at focus, \bigcirc/\bigcirc -1.1 mm) (\star/\star +1.1 mm), laser speed, and laser power from the following LIG compositions: (a) LIG_0; (b) LIG_0.6 and (c) LIG_1.2. FWHM values for the G band in relation to laser focus (\square +1.1 mm, Δ at focus, \bigcirc -1.1 mm) (\star +1.1 mm), laser speed, and laser power from the following LIG composition: (d) LIG_0; (e) LIG_0.6 and (f) LIG_1.2.

Intensity variation of the D, G and 2G bands also indicates a change in the type of LIGE formed in relation to the amount of LIG added to the ink and changes in laser parameters, as shown in Figures 4.23a-c. The same variations were also found for the FWHM values of the G band, as it can be observed in Figures 4.23d-f.

The laser parameter variations and the sheet resistance values of all CMC-based inks obtained in the different LIG compositions were measured to correlate the physical and morphological properties with the electrical properties of the ink, as illustrated in Figure 4.24.

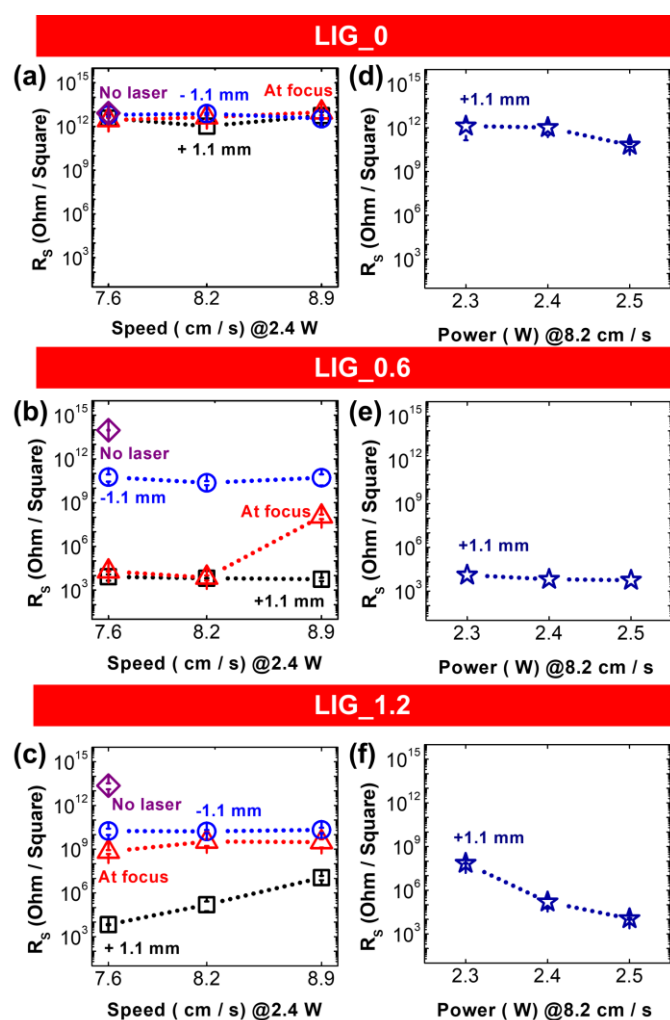


Figure 4.24 - Sheet resistance of LIGE as a function of tip speed and laser focus at constant laser power: (a) LIG_0, (b) LIG_0.6, and (c) LIG_1.2. Sheet resistance as a function of laser power at constant laser focus and tip speed: (d) LIG_0, (e) LIG_0.6, and (f) LIG_1.2.

The final material presented a wide variation in sheet resistance with modification of LIG composition in the ink and laser beam focus in relation to tip speed, as evidenced in Figures 4.24a-c. In addition, sheet resistance showed a slight variation in relation to laser power, as that observed for CNC (Figs. 4.24d-f). It is worth mentioning that the samples containing LIG before laser passing presented high sheet resistance ($\approx 10^{12} \Omega / \text{sq.}$) despite their darker color, appearance of Raman D, G and 2G bands and lower FWHM values. The higher sheet resistance values found for the no laser samples containing LIG are possibly due to the dispersed graphene embedded in a non-conductive CMC matrix, as it can be observed in the photomicrographs of the no laser samples (Appendix B).

The LIG_0.6 formulation after laser passing with beam defocus of +1.1 mm presented sheet resistance values lower than those of the other formulations, suggesting that this was the ideal parameter condition for obtaining LIGE (Figs 4.24b and e). The LIG_0.6 formulation showed lower LIGE sheet resistance ($\approx 5.5 \text{ k}\Omega / \text{sq.}$) for the condition with laser beam defocus of +1.1 mm, laser power of 2.4 W, and tip speed of 8.2 cm / s. The greater microstructural changes, lower values of FWHM for the G band and $I_D/I_G \approx 1$ are physical characteristics similar to those reported for the lower resistive LIG obtained from wood [159].

The LIG_1.2 sample exhibited low LIGE sheet resistance ($\approx 12 \text{ k}\Omega / \text{sq.}$) for the condition with laser beam defocus of +1.1 mm, laser power of 2.5 W, and tip speed of 8.2 cm/s (Figs 4.24c and f). The Raman band intensities characteristic of the LIG_1.2 graphene sample obtained from the optimized laser parameters, as well as its microstructures, were quite similar to those of the ideal LIG_0.6 sample.

The LIGE with lower sheet resistance values presented defects and conductive crystalline graphene and more substantial microstructural changes compared with those of samples before laser passing. Moreover, the LIG_0 formulation did not show expressive microstructural changes compared with the no laser sample and relevant variation in sheet resistance with modification of the laser parameters (Figs. 4.24a, d), which demonstrate the common

dependence between the LIG from CNC and the LIG synthesized from CMC-based ink to obtain the low sheet resistance LIGE.

Based on the data obtained, only two types of LIGE were chosen to fabricate the ZnO UV sensors: LIGE_0.6 from LIG_0.6 and LIGE_1.2 from LIG_1.2, both with the lowest sheet resistance values obtained from the optimized laser parameters.

4.2.3 DLIGE on tracing paper surface

To compare the LIGEs, the DLIGE were synthesized on oxidized tracing paper. Properties of the DLIGE were assessed according to their Raman spectra and sheet resistance values by varying the number of laser passes on the paper surface, as shown in Figure 4.25.

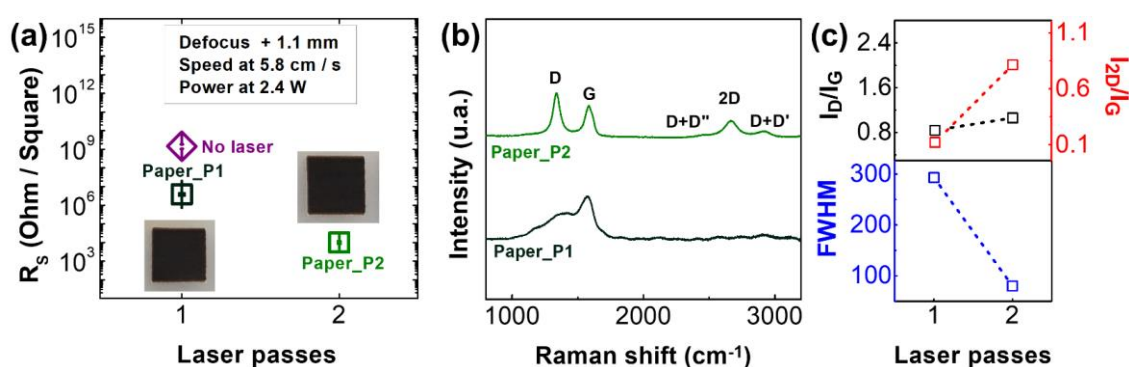


Figure 4.25 - LIG on tracing paper surface: (a) paper sheet resistance before laser passing and DLIGE sheet resistance as a function of the number of laser passes at 2.4 W laser power, 5.8 cm/s tip speed, and +1.1 mm defocus. The photographs highlight the DLIGE squares drawn from the first (Paper_P1) and second (Paper_P2) laser passes; (b) Raman spectra of DLIGE from each laser pass; and (c) I_b/I_g and I_{2D}/I_g ratios and FWHM values of the G band in relation to the laser passes.

The laser passes clearly decreased the DLIGE sheet resistance, which reached values as low as ≈ 10 k Ω /sq - quite similar to those found for the LIGE. The color of the DLIGE squares slight changed according to laser passes, which became darker after the second laser pass, as illustrated in Figure 4.25a.

Upon the third laser pass, the paper was partially destroyed, as shown in Figure 4.26.

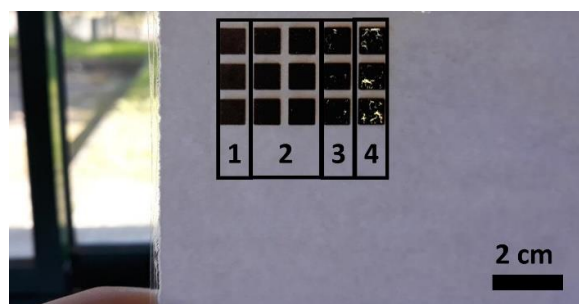


Figure 4.26 - Photograph of the DLIGE squares according to the number of laser passes, showing the partial destruction of the paper substrate after the third laser pass.

It should be noted that the tracing paper sheet resistance before the laser passes ($\approx 1 \text{ G}\Omega/\text{sq.}$) is smaller than those of the other samples for the same condition. This behavior may be associated with ionic conduction due to the presence of Na^+ ions generated from the oxidation process that might still be present in the oxidized paper [167]. It is worth emphasizing that the DLIGE microstructures undergo changes throughout laser passing, presenting a more porous structure in relation to the oxidized paper microstructure before laser passing, as shown in Figure 4.27.

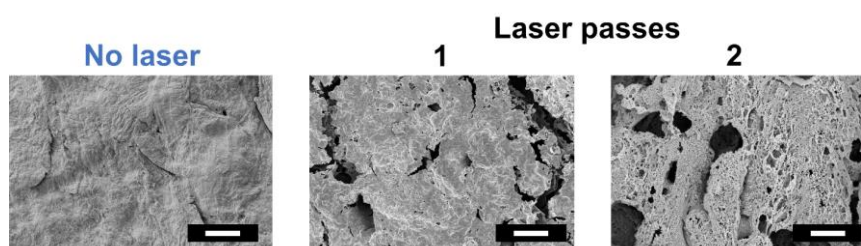


Figure 4.27 - Photomicrographs of oxidized tracing paper microstructure before and after laser incidence, varying the number of laser passes (15 μm white bar scale).

The following information was obtained from the Raman spectra of the DLIGE after two laser passes on tracing paper (Fig. 4.25b): after the first pass,

it was possible to observe a D (1336 cm^{-1}) band, corresponding to the degree of disorder of the formed graphene, and a G (1563 cm^{-1}) band, corresponding to the graphite that constitutes the induced material [180,181], with predominance of intensity of the graphite band over the disordered graphene band. Upon the second pass, an inversion in band intensity was verified, indicating predominance of defective graphene in the induced material. In addition, after the second laser pass, there was explicit appearance of the 2D ($\approx 2670\text{ cm}^{-1}$) band, suggesting DLIGE containing conductive crystalline graphene [96], and of the D+D' ($\approx 2933\text{ cm}^{-1}$) and D+D'' ($\approx 2444\text{ cm}^{-1}$) bands, indicating real graphene disorder in the DLIGE [207,208].

Figure 4.25c (top) shows an analysis of the variation between the I_D/I_G and I_{2D}/I_G ratios related to the DLIGE according to the number of direct laser passes on tracing paper. The increased I_D/I_G ratio with increasing the number of laser passes indicates a higher degree of defects in the DLIGE resulting from the greater reactivity to laser of aliphatic materials (e.g., coal and cellulose) compared with aromatic materials (e.g., lignin) [159,210]. In addition, the increased I_{2D}/I_G ratio indicates stacking of fewer graphene layers with increasing the number of laser passes [211]. Moreover, the FWHM values related to the G band reduced with increasing the number of laser passes, and showed FWHM values upon the second pass similar to those of the LIG synthesized from CNC and the LIGE obtained from CMC-based ink, as illustrated in Figure 4.25c (bottom). These characteristics may be associated with a decrease in the DLIGE sheet resistance after the second laser pass, as also observed for the CNC. From these results, the DLIGE obtained from LIG after the second laser pass on the oxidized tracing paper was chosen to fabricate the ZnO UV sensors for comparison with the LIGE devices.

4.2.4 Electrical performance of ZnO UV sensors

Aiming at the best approach to produce graphene obtained from PALFs for electronic devices, LIGE_0.6, LIGE_1.2, and DLIGE were used as electrodes for the ZnO UV sensors, as shown in Figure 4.28.

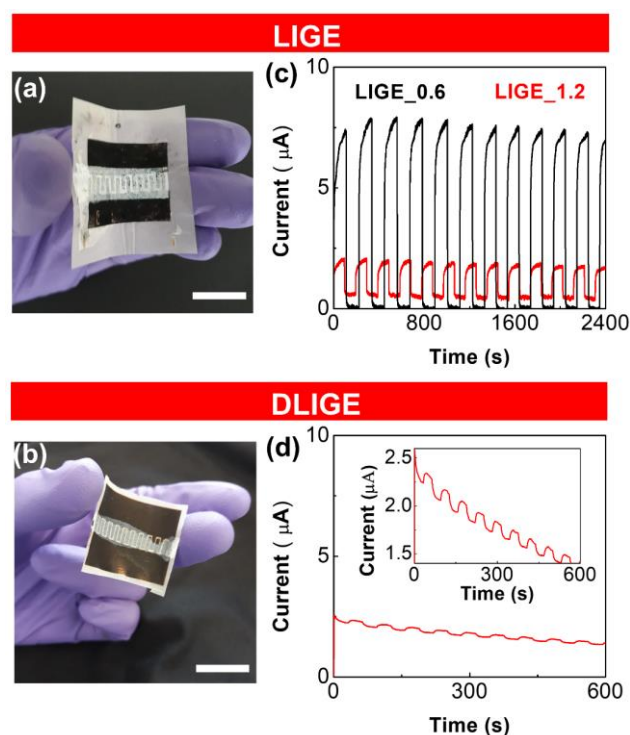


Figure 4.28 - Photographs of the ZnO UV sensors: (a) LIGE and (b) DLIGE (2 cm white bar scale). Photocurrent curve responses during ON/OFF UV radiation of the ZnO UV sensors: (c) LIGE_0.6, LIGE_1.2, and (d) DLIGE highlighted in zoom on the curve.

There were no apparent visual differences between the UV sensors obtained from LIGE and DLIGE after CMC-based ink ZnO screen-printing deposition between the LIG interdigital contacts, as evidenced in Figures 4.28a and b. However, from the electrical characterization curves of the ZnO UV sensors, it was possible to observe the effect of forming LIG from CNC on LIGE performance in the sensors, as well as a clear difference between the LIGE and DLIGE sensors performance, as illustrated in Figures 4.28c and d, respectively.

The current value of the LIGE_0.6 sensor showed a sharp increase when exposed to UV radiation compared with those of the LIGE_1.2 (almost 8-fold) and DLIGE (nearly 40-fold) sensors. The LIGE_0.6 ($0.925 \pm 0.017 \mu\text{A/W}$) device was more responsive to UV radiation than the LIGE_1.2 ($0.164 \pm 0.014 \mu\text{A/W}$) and DLIGE ($0.009 \pm 0.001 \mu\text{A/W}$) devices. The LIGE_0.6 sensor presented responsivity values higher than those of UV sensors fabricated from PEI/PI substrates [107,170] and ZnO UV sensors on paper [117], and a performance

quite similar to that of ZnO UV sensors on cork [175], with the latter two studies carried out with silkscreen deposition between the carbon interdigital contacts.

The difference in performance between the LIGE sensors may be associated with the lower sheet resistance of LIGE_0.6 compared with that of LIGE_1.2 due to the ideal LIG concentration in the CMC-based ink for lower sheet resistance (Figure 4.24). According to our analysis, the CNC-LIG increases the thermal resistance of CMC, helping in the formation of graphene, as observed for the LIG_0.6. However, the excess of LIG can promote an increase in the ink thermal conduction, promoting a possible thermal degradation of CMC by laser, as observed for the LIG_1.2.

In addition, the clear difference observed between LIGE and DLIGE may be associated with the LIG/paper substrate interface, LIG porosity, and short circuit in the DLIGE gap electrodes, as shown in Figure 4.29.

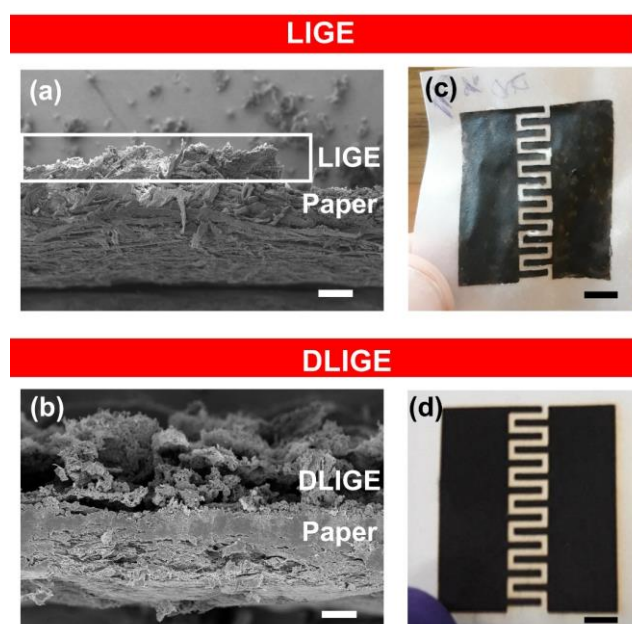


Figure 4.29 – Cross-sectional photomicrography of LIG/tracing paper interface of (a) LIGE and (b) DLIGE (20 μm white bar scale). LIG gap of (c) LIGE and (d) DLIGE (5 mm black bars scale).

The clear difference observed between LIGE and DLIGE may be associated with the better LIGE/paper substrate interface compared with the DLIGE/paper interface and, consequently, with the interface of other materials

such as ZnO ink, as shown in the Figures 4.29a and b. Another factor that may have influenced the difference in performance between LIGE and DLIGE is the difference in graphene porosity between these two approaches, where the graphene that formed the LIGE was apparently less porous than the one that formed the DLIGE (Figs. 4.29a and b).

It is worth highlighting that the DLIGE sensor presented higher leakage current between the electrodes without UV radiation incidence compared with that of the LIGE sensor. This behavior may be associated with the paper ionic conductivity, indicated by the lower sheet resistance value of the oxidized paper compared with those of the other samples before laser passing (Figs. 4.24 and 4.25). This problem may also be associated with the dispersion of DLIGE powder in the carbon interdigital contacts by the laser or with the screen-printing technique. In addition, the low thermal resistance of cellulose may have promoted a partial burning of its content between the gaps and generated a slight physical change in conductivity between the carbon interdigital contacts. These last two hypotheses can be confirmed by noting that the DLIGE gap shows a brownish color compared with the LIGE gap, which still keeps whitish color on the paper, as shown in Figures 4.29c and d. Comparison between LIGE and DLIGE showed the effectiveness of fabricating the LIGE electrodes using the ink technique, which presented superior performance for the LIG_0.6 device.

Aiming to produce flexible electronic devices, the bending tests of the ZnO UV sensors to compose the LIGE were performed using a metal bending support. Figure 4.30 shows the electrical bending curves for LIGE_0.6 and LIGE_1.2.

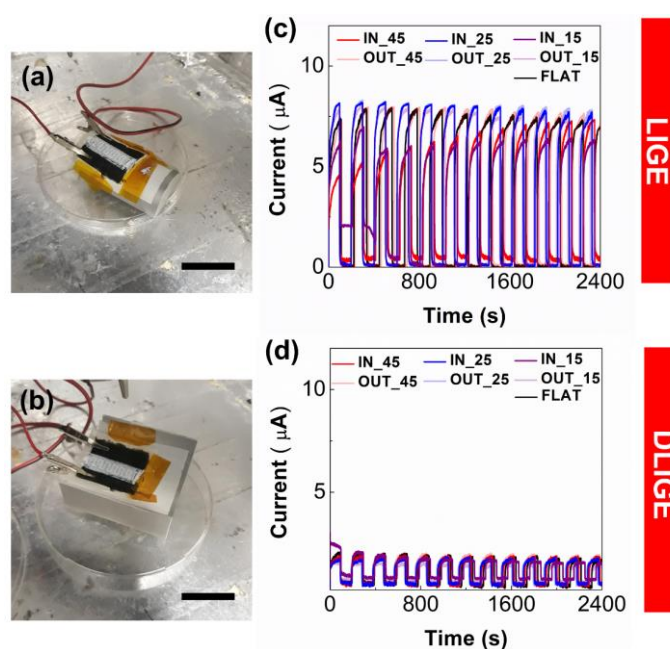


Figure 4.30 - Photographs of the CMC ZnO UV sensors with LIGE under (a) outward (OUT) and (b) inward (IN) bending tests (2 cm black bar scale). Influence of the in- and out-plane bending radii on the electrical performance of ZnO UV sensors: (a) LIGE_0.6 and (b) LIGE_1.2.

The devices were assessed using the bending test varying the radius from 45 to 15 ° in the outward (OUT) and inward (IN) modes, as illustrated in Figures 4.30a and b, and subsequently characterized in the flat mode.

Figures 4.30c and d show the curves of the LIGE_0.6 and LIGE_1.2 devices in the bending and flat modes. Both devices showed good performance in all radii of curvature both in the IN and OUT modes, and very similar behavior in the flat mode before and after the test, as previously reported for ZnS/SnO₂ UV sensors [170] and capacitors [212] with LIG electrodes. However, a slight reduction in responsivity was observed as the radius of curvature decreased. This reduction in responsivity is associated with increased deformation in the axial region of the carbon interdigital contacts where the ZnO ink was deposited, as reported for UV ZnO sensors with LIG electrodes [107]. In addition, the LIGE_0.6 device exhibited a slight variation in responsivity at the beginning of the test, stabilizing after 1600 s.

With these results, the LIGE sensors were proved to be applicable as flexible electronic devices, opening numerous application potentials in organic and sustainable devices for real-time wearable UV-radiation monitoring [213].

5 CONCLUSIONS

5.1 ICCM by SB-Spinning as substrate and dielectric “interstrate” layer for flexible electronics

Flexible regenerated ICCM can be obtained by SB-spinning using PEO as additive followed by a deacetylation process in alkaline hydroxides: ethanol solution. The type of alkaline hydroxide used in the deacetylation process affected the morphology and electrochemical properties of the cellulose mat, thus influencing the electrical performance of the GIZO FETs. The solid-state electrolyte mats were successfully applied as an "interstrate" layer on the oxide-based FETs and integrated into an inverter. The KOH_mat proved to be the best option for obtaining an ICCM with a capacity of $\sim 80 \text{ nF cm}^2$ over a wider frequency range. Significantly, the performance of the KOH_mat transistors was similar to that of paper applied simultaneously as a gate dielectric and substrate in FETs. In addition, using the KOH_mat, it was possible to handwrite a circuit using a 2 HB pencil and design an inverter with a gain of 2 and adequate dynamic performance up to 3 Hz. These characteristics are similar to those of commercial paper surface, which indicates that the low-cost and environmentally friendly cellulose mat electronics obtained by SB-Spinning competes with paper electronics. The dual function of the functional ICCM, together with the simplicity and versatility of the SB-Spinning process, reduce the fabricating complexity level while adjusting the structural, morphological, and electrochemical properties. Altogether, the results presented herein confirm that a new generation of ICCMs can be explored for wearable electronics, paving the way for a New Era of the “Internet of things” revolution, with portability and low energy consumption.

5.2 LIGE from pineapple CNCs and CMC-based ink for flexible ZnO UV sensor

This study demonstrated that the developed LIGE can be applied to ZnO UV sensors fabricated from CMC-based ink with LIG synthesized from CNC extracted from PALFs. The LIGE_0.6 device proved to be ideal to form ZnO UV

sensors, reaching a responsivity value close to $1 \mu\text{A/W}$ and performance superior to that of some LIG sensors. In this context, the laser parameters (laser focus) and the amount of LIG used in the ink proved to be variables fundamental to develop the LIGE. In addition, the high crystallinity index of CNC may be another factor positively influencing the LIGE performance, since the LIG obtained from CNC presented sheet resistance values lower than those of all other cellulose samples. Furthermore, LIGE proved to be a better approach for ZnO UV sensors compared with DLIGE, with a performance gain almost 40-fold greater. This difference may be associated with the decreased porosity and better interface of the LIGE with other materials, as well as with the short-circuit problems between the carbon interdigital contacts of the DLIGE. The short-circuit problems were possibly caused by the ionic conductivity of the oxidized paper, the partial induction of graphene in the interdigital contacts and/or contamination by DLIGE powder dispersed in the electrode gap by the laser inert gas jet, or by the screen-printing technique. Finally, the ZnO UV sensors obtained from LIGE presented good performance in the bending test mode, with a slight reduction in responsivity, and similar performance in flat mode before and after the bending test.

Altogether, the results presented herein demonstrated the potential to obtain LIGE from CMC-based ink from LIG obtained from CNC extracted from PALFs for application in ZnO UV sensors. This approach opens new promising possibilities that consolidates cellulose as a precursor to electrodes, targeting electronic devices based on organic and sustainable materials.

6 SUGGESTIONS FOR FUTURE STUDIES

The following suggestions for works complementary to this doctoral project are presented:

- 1) Investigate the LIGE deposition and induction on ICCMs aimed at UV sensors and/or LIG-gated transistors on mats;
- 2) Assess the possibility of inducing LIG on CMC mat fibers introducing the CNCs functionalized;
- 3) Study the application of ICCMs for supercapacitors and storage energy systems aiming wearable applications;
- 4) Study on oxide deposition in cellulose acetate fibers obtained by SB-Spinning targeting electronic microdevices.

7 REFERENCES

- [1] BERGLUND, L. Cellulose-Based Nanocomposites. In: A. K. Mohanty; L. T. Drzal; F. Group (Orgs.); **Natural Fibers, Biopolymers, and Biocomposites**, 2005.
- [2] RINAUDO, M. Main properties and current applications of some polysaccharides as biomaterials. **Polymer International**, v. 57, n. 3, p. 397–430, 2008.
- [3] KAPLAN, D. L. Introduction to biopolymers from renewable resources. **Biopolymers from Renewable Resources**. p.1–29, 1998.
- [4] MOON, R. J.; MARTINI, A.; NAIRN, J.; et al. Cellulose nanomaterials review: structure, properties and nanocomposites. **Chemical Society Reviews**, v. 40, n. 7, p. 3941–3994, 2011.
- [5] KHALIL, H. P. S. A.; BHAT, A. H.; YUSRA, A. F. I. Green composites from sustainable cellulose nanofibrils: A review. **Carbohydrate Polymers**, v. 87, n. 2, p. 963–979, 2012
- [6] SIRÓ, I.; PLACKETT, D. Microfibrillated cellulose and new nanocomposite materials: a review. **Cellulose**, v. 17, n. 3, p. 459–494, 2010.
- [7] BARHOUM, A.; SAMYN, P.; ÖHLUND, T.; DUFRESNE, A. Review of recent research on flexible multifunctional nanopapers. **Nanoscale**, v. 9, n. 40, p. 15181–15205, 2017.
- [8] ZHANG, Y.; ZHANG, L.; CUI, K.; et al. Flexible electronics based on micro / nanostructured paper. **Advanced Materials**, v. 30, n. 51, p. 1801588, 2018.
- [9] GREY, P.; FERNANDES, S. N.; GASPAR, D.; et al. Field-effect transistors on photonic cellulose nanocrystal solid electrolyte for circular polarized light sensing. **Advanced Functional Materials**, v. 1805279, p. 1–8, 2018.
- [10] GREY, P.; FERNANDES, S. N.; GASPAR, D.; et al. Ionically modified cellulose nanocrystal self-assembled films with a mesoporous twisted superstructure: Polarizability and application in ion-gated transistors. **ACS Applied Electronic Materials**, v. 2, p. 426–436, 2020.

- [11] PEREIRA, L.; GASPAR, D.; GUERIN, D.; et al. The influence of fibril composition and dimension on the performance of paper gated oxide transistors. **Nanotechnology**, v. 25, n. 9, p. 094007, 2014.
- [12] REID, M. S.; VILLALOBOS, M.; CRANSTON, E. D. Benchmarking cellulose nanocrystals: From the laboratory to industrial production. **Langmuir**, v. 33, n. 7, p. 1583–1598, 2017.
- [13] FANG, Z.; ZHU, H.; PRESTON, C.; et al. Highly transparent and writable wood all-cellulose hybrid nanostructured paper. **Journal of Materials Chemistry C**, v. 1, n. 39, p. 6191–6197, 2013.
- [14] MISHRA, S.; MOHANTY, A. K.; DRZAL, L. T.; MISRA, M.; HINRICHSEN, G. A review on pineapple leaf fibers, sisal fibers and their biocomposites. **Macromolecular Materials and Engineering**, v. 289, n. 11, p. 955–974, 2004.
- [15] CORRÊA, A. C.; DE MORAIS TEIXEIRA, E.; PESSAN, L. A.; MATTOSO, L. H. C. Cellulose nanofibers from curaua fibers. **Cellulose**, v. 17, n. 6, p. 1183–1192, 2010.
- [16] CLARO, P.; DE CAMPOS, A.; CORRÊA, A.; et al. Curaua and eucalyptus nanofiber films by continuous casting : mixture of cellulose nanocrystals and nanofibrils. **Cellulose**, v. 26, n. 4, p. 2453–2470, 2019.
- [17] CLARO, P. I. C.; CORRÊA, A. C.; DE CAMPOS, A.; et al. Curaua and eucalyptus nanofibers films by continuous casting: Mechanical and thermal properties. **Carbohydrate polymers**, v. 181, p. 1093–1101, 2018.
- [18] CHERIAN, B. M.; LEÃO, A. L.; DE SOUZA, S. F.; et al. Cellulose nanocomposites with nanofibres isolated from pineapple leaf fibers for medical applications. **Carbohydrate Polymers**, v. 86, n. 4, p. 1790–1798, 2011.
- [19] MARCOS, R.; PIRES, W.; NETO, F.; et al. Cellulose nanocrystals from pineapple leaf , a new approach for the reuse of this agro-waste. **Industrial Crops & Products**, v. 50, p. 707–714, 2013.

- [20] D'EECKENBRUGGE, G. C.; LEAL, F.; BARTHOLOMEW, D. Morphology, anatomy and taxonomy. **The Pineapple: Botany, Production and Uses**. p.13–32, 2003.
- [21] KLOCK, U.; MUNIZ, G. I. B.; HERNANDEZ, J. A.; ANDRADE, A. S. **Química da Madeira**. Curitiba, 2005.
- [22] ROWELL, R. M. Characterization and factors effecting fiber properties. **Natural Polymers and Agrofibers Based Composites**, 2000.
- [23] CARVALHO, W.; CANILHA, L.; FERRAZ, A.; MILAGRES, A. M. F. Uma visão sobre a estrutura, composição e biodegradação da madeira. **Química Nova**, v. 32, n. 8, p. 2191–2195, 2014.
- [24] SATYANARAYANA, K. G.; ARIZAGA, G. G. C.; WYPYCH, F. Progress in Polymer Science Biodegradable composites based on lignocellulosic fibers — An overview. **Progress in Polymer Science**, v. 34, n. 9, p. 982–1021, 2009.
- [25] UEA. Pesquisas pretendem potencializar uso da fibra de curauá no Amazonas. **Correio da Amazônia**, 2017.
- [26] POSTEK, M. T.; MING, B.; WAGNER, R.; et al. Development of the metrology and imaging of cellulose nanocrystals. **Measurement Science and Technology**, v. 22, n. 2, p. 024005, 2010.
- [27] BUTCHOSA ROBLES, N. Tailoring Cellulose Nanofibrils for Advanced Materials, **Doctoral thesis, KTH Royal Institute of Technology**, 2014.
- [28] SILVA, R.; HARAGUCHI, S. K.; MUNIZ, E. C.; RUBIRA, A. F. Aplicações de fibras lignocelulósicas na química de polímeros e em compósitos. **Química Nova**, v. 32, n. 3, p. 661–671, 2009.
- [29] KLEMM, D.; KRAMER, F.; MORITZ, S.; et al. Nanocelluloses: A new family of nature-based materials. **Angewandte Chemie International Edition**, v. 50, n. 24, p. 5438–5466, 2011.
- [30] KALIA, S.; BOUFI, S.; CELLI, A.; KANGO, S. Nanofibrillated cellulose : surface modification and potential applications. **Colloid and Polymer Science**, v. 292, n. 1, p. 5–31, 2014.

- [31] THAKUR, V. K.; THAKUR, M. K.; RAGHAVAN, P.; KESSLER, M. R. Progress in green polymer composites from lignin for multifunctional applications: A review. **ACS Sustainable Chemistry & Engineering**, v. 2, n. 5, p. 1072–1092, 2014.
- [32] SILVA, M.; COLODETTE, J. L.; OLIVEIRA, R. C. DE. Calidad de las maderas de clones de eucalyptus de brasil para la producción de celulosa kraft. **International Colloquium on Eucalyptus Pulp**, p.24–26, 2007.
- [33] MARQUES, G.; GUTIÉRREZ, A.; DEL RÍO, J. C. Chemical characterization of lignin and lipophilic fractions from leaf fibers of curaua (*Ananas erectifolius*). **Journal of Agricultural and Food Chemistry**, v. 55, n. 4, p. 1327–36, 2007.
- [34] SCHELLER, H. V.; ULVSKOV, P. Hemicelluloses. **Annual Review of Plant Biology**, v. 61, 2010.
- [35] ROY, D.; SEMSARILAR, M.; GUTHRIE, J. T.; et al. Cellulose modification by polymer grafting : a review. **Chemical Society Reviews**, v. 38, n. 7, p. 2046–2064, 2009.
- [36] KALIA, S.; AVÉROUS, L. (ORGS.). Biopolymers: biomedical and environmental applications. **John Wiley & Sons**, 2011.
- [37] KLEMM, D.; HEUBLEIN, B.; FINK, H.-P. P.; BOHN, A. Cellulose: fascinating biopolymer and sustainable raw material. **Angewandte Chemie - International Edition**, v. 44, n. 22, p. 3358–93, 2005
- [38] ISHIKAWA, A.; OKANO, T.; SUGIYAMA, J. Fine structure and tensile properties of ramie fibres in the crystalline form of cellulose I, II, III and IV. **Polymer**, v. 38, n. 2, p. 463–468, 1997.
- [39] SULLIVAN, A. C. O. Cellulose : The structure slowly unravels. **Cellulose**, v. 4, n. 3, p. 173–207, 1997.
- [40] LINDGREN, T.; EDLUND, U.; IVERSEN, T. A multivariate characterization of crystal transformations of cellulose. **Cellulose**, v. 2, n. 4, p. 273–288, 1995.
- [41] FREY, M. W. Electrospinning cellulose and cellulose derivatives. **Polymer Reviews**, v. 48, n. 2, p. 378–391, 2008.

- [42] CANDIDO, R. G.; GONÇALVES, A. R. Synthesis of cellulose acetate and carboxymethylcellulose from sugarcane straw. **Carbohydrate Polymers**, v. 152, p. 679–686, 2016.
- [43] MALM, C. J.; TANGHE, L. J.; LAIRD, B. C. Preparation of cellulose acetate - Action of sulfuric acid. **Industrial & Engineering Chemistry**, v. 38, n. 1, p. 77–82, 1946.
- [44] CAO, J.; MA, X.; YANG, A.; XU, W. Preparation of cellulose acetate/nano-SiO₂ composites and their application in filtration of cigarette smoke. **Polymers and Polymer Composites**, v. 14, n. 1, p. 65–71, 2006.
- [45] ISOGAI, A.; HÄNNINEN, T.; FUJISAWA, S.; SAITO, T. Review: Catalytic oxidation of cellulose with nitroxyl radicals under aqueous conditions. **Progress in Polymer Science**, v. 86, p. 122–148, 2018.
- [46] CHEN, H. Lignocellulose biorefinery product engineering. **Lignocellulose Biorefinery Engineering**. p.125–165, 2015.
- [47] EL BARKANY, S.; JILAL, I.; EL IDRISSE, A.; et al. Homogenous synthesis of new C6 regioselective cellulose acetate butyl hexane-1, 6-diyldicarbamate based on esparto cellulose of morocco oriental. **Applied Journal of Environmental Engineering Science**, v. 3, n. 3, p. 3–3, 2017.
- [48] UNITED, N. F. AND AGRICULTURE ORGANIZATION. Production quantities of Pineapples by country.
- [49] CABRAL, J. R. S.; FERREIRA, F. R.; DE MATOS, A. P.; SANCHES, N. F. **Banco ativo de Germoplasma de Abacaxi da Embrapa Mandioca e Fruticultura**. 1998.
- [50] LEÃO, A. L.; MACHADO, I. S.; DE SOUZA, S. F.; SORIANO, L. Production of curauá (*Ananas Erectifolius*) fibers for industrial applications: characterization and micropropagation. **VI International Pineapple Symposium**, p.227–238, 2007.
- [51] MANETTI, L. M.; DEIAPORTE, R. H.; LAVERDE, A. Metabólitos secundários da família Bromeliaceae. **Quimica Nova**, v. 32, n. 7, p. 1885–1897, 2009.

- [52] ZHANG, R.; LIU, Y. High energy oxidation and organosolv solubilization for high yield isolation of cellulose nanocrystals (CNC) from Eucalyptus hardwood. **Scientific reports**, v. 8, n. 1, p. 1–11, 2018.
- [53] ROCES, M. Dress Status, and Identity in the philippines : pineapple fiber cloth and ilustrado fashion. **Fashion Theory**, v. 17, n. 3, p. 341–372, 2012.
- [54] MONTEIRO, S. N.; COELI, R.; AQUINO, M. P.; LOPES, F. P. D.; CARVALHO, E. A. DE. Mechanical behavior and structural characteristics of polymeric composites reinforced with continuous and aligned curaua fibers. **Matéria**, v. 11, n. 3, p. 197–203, 2006.
- [55] YUSOF, Y.; ASIA, S.; ADAM, A. Novel technology for sustainable pineapple leaf fibers productions. **Procedia CIRP**, v. 26, p. 756–760, 2015.
- [56] DE ARAUJO, M. A. M.; DE SENA NETO, A. R.; HAGE JR, E.; MATTOSO, L. H. C.; MARCONCINI, J. M. Curaua Leaf Fiber (*Ananas comosus var . erectifolius*) reinforcing poly(lactic acid) biocomposites : Formulation and performance. **Polymer Composites**, v. 36, n. 8, p. 1520–1530, 2015.
- [57] CORRÊA, A. C.; TEODORO, K. B. R.; SIMÃO, J. A.; et al. Cellulose nanocrystals from curaua fibers and poly[ethylene-co-(vinyl acetate)] nanocomposites: Effect of drying process of CNCs on thermal and mechanical properties. **Polymer Composites**, v. 41, p. 1736–1748, 2020.
- [58] OLIVEIRA, J. E.; MATTOSO, L. H. C.; ORTS, W. J.; MEDEIROS, E. S. Structural and morphological characterization of micro and nanofibers produced by electrospinning and solution blow spinning: A comparative study. **Advances in Materials Science and Engineering**, v. 2013, 2013.
- [59] MEDEIROS, E. S.; GLENN, G. M.; KLAMCZYNSKI, A. P.; ORTS, W. J.; MATTOSO, L. H. Solution blow spinning: A new method to produce micro-and nanofibers from polymer solutions. **Journal of Applied Polymer Science**, v. 134, n. 4, p. 2322–2330, 2009.

- [60] MEDEIROS, E. S.; GLENN, G. M.; KLAMCZYNSKI, A. P.; ORTS, W. J.; MATTOSO, L. H. Solution blow spinning. **U.S. Patent No 8,641,960**, 2014.
- [61] MEHL, E. L. Do Transistor ao microprocessador. Available in: https://social.stoa.usp.br/articles/0015/5705/historia_transistor.pdf.
- [62] MILLMAN, J.; HALKIAS, C. Integrated electronics: Analog digital circuits and systems. **McGraw-Hill, Inc**, 1972.
- [63] FORTUNATO, E.; BARQUINHA, P.; MARTINS, R. Oxide semiconductor thin-film transistors: A review of recent advances. **Advanced Materials**, v. 24, n. 22, p. 2945–2986, 2012.
- [64] FERREIRA, E. C. Transistores de efeito de campo (FETS). Available in: http://www.demic.fee.unicamp.br/~elnatan/ee640/aula_mosfet.pdf.
- [65] RAZAVI, B. Fundamentos de microeletrônica. **Grupo Gen-LTC.**, 2000.
- [66] GRAY, P. R.; HURST, P. J.; LEWIS, S. H.; MEYER, R. G. Analysis and design of analog integrated circuits. **John Wiley & Sons**, 2009.
- [67] TOBJÖRK, D.; ÖSTERBACKA, R. Paper electronics. **Advanced Materials**, v. 23, n. 12, p. 1935–1961, 2011.
- [68] NAGASHIMA, K.; KOGA, H.; CELANO, U.; et al. Cellulose nanofiber paper as an ultra flexible nonvolatile memory. **Scientific Reports**, v. 4, n. 1, p. 1–7, 2014.
- [69] ÁGUAS, H.; MATEUS, T.; VICENTE, A.; et al. Thin film silicon photovoltaic cells on paper for flexible indoor applications. **Advanced Functional Materials**, v. 25, n. 23, p. 3592–3598, 2015.
- [70] HUANG, J.; ZHU, H.; CHEN, Y.; et al. Highly transparent and flexible nanopaper transistors. **ACS Nano**, v. 7, n. 3, p. 2106–2113, 2013.
- [71] ZHANG, Y. Z.; WANG, Y.; CHENG, T.; et al. Flexible supercapacitors based on paper substrates: a new paradigm for low-cost energy storage. **Chemical Society Reviews**, v. 44, n. 15, p. 5181–5199, 2015.
- [72] GASPAR, D.; FERNANDES, S. N.; DE OLIVEIRA, A. G.; et al. Nanocrystalline cellulose applied simultaneously as the gate dielectric and the substrate in flexible field effect transistors. **Nanotechnology**, v. 25, n. 9, p. 094008, 2014.

- [73] GASPAR, D.; MARTINS, J.; BAHUBALINDRUNI, P.; et al. Planar dual-gate paper/oxide field effect transistors as universal logic gates. **Advanced Electronic Materials**, v. 4, n. 12, p. 1–8, 2018.
- [74] FORTUNATO, E.; CORREIA, N.; BARQUINHA, P.; et al. High-performance flexible hybrid field-effect transistors based on cellulose fiber paper. **IEEE Electron Device Letters**, v. 29, n. 9, p. 988–990, 2008.
- [75] MARTINS, R.; BARQUINHA, P.; PEREIRA, L.; et al. Write-erase and read paper memory transistor. **Applied Physics Letters**, v. 93, n. 20, 2008.
- [76] FERREIRA, I.; BRÁS, B.; CORREIA, N.; et al. Self-rechargeable paper thin-film batteries: performance and applications. **Journal of Display Technology**, v. 6, n. 8, p. 332–335, 2010.
- [77] MARTINS, R.; NATHAN, A.; BARROS, R.; et al. Complementary metal oxide semiconductor technology with and on paper. **Advanced Materials**, v. 23, n. 39, p. 4491–4496, 2011.
- [78] CHO, J. H.; LEE, J.; XIA, Y. U.; KIM, B.; HE, Y.; RENN, M. J.; .LODGE, T. P.; FRISBIE, C. D. Printable ion-gel gate dielectrics for low-voltage polymer thin-film transistors on plastic. *Nature materials*, v. 7, n. 11, p. 900-906, 2008.
- [79] GOULD, R. G. The LASER, light amplification by stimulated emission of radiation. **The Ann Arbor Conference on Optical Pumping**, University of Michigan, p.92, 1959.
- [80] MAIMAN, T. H. Stimulated optical radiation in ruby. **Nature**, v. 187, n. 4736, p. 493–494, 1960.
- [81] TOWNES, C. H. Theodore H. Maiman (1927 – 2007). **Nature**, v. 447, n. 7145, p. 654–654, 2007.
- [82] BACHMANN, F.; LOOSEN, P.; POPRAWA, R. (ORGS.). **High Power Diode Lasers: Technology and Applications**. Springer, 2017.
- [83] MEYER, G.; AMER, N. M. Erratum: Novel optical approach to atomic force microscopy. **Applied Physics Letters**, v. 53, n. 24, p. 2400–2402, 1988.

- [84] CHÉNAIS, S.; FORGET, S. Recent advances in solid-state organic lasers. **Polymer International**, v. 61, n. 3, p. 390-406, 2012.
- [85] JEONG, Y.; SAHU, J. K.; PAYNE, D. N.; NILSSON, J. Ytterbium-doped large-core fiber laser with 1.36 kW continuous-wave output power. **Optics Express**, v. 12, n. 25, p. 6088–6092, 2014.
- [86] PARK, H. G.; KIM, S. H.; KWON, S. H.; et al. Electrically driven single-cell photonic crystal laser. **Science**, v. 305, n. 5689, p. 1444–1447, 2004.
- [87] BECK, M.; HOFSTETTER, D.; AELLEN, T.; et al. Continuous wave operation of a mid-infrared semiconductor laser at room temperature. **Science**, v. 295, n. 5553, p. 301–305, 2002.
- [88] SCHÄFER, F. P.; SCHMIDT, W.; VOLZE, J. Organic dye solution laser. **Applied Physics Letters**, v. 9, n. 8, p. 306–309, 1966.
- [89] DEACON, D. A.; ELIAS, L. R.; MADEY, J. M.; et al. First operation of a free-electron laser. **Physical Review Letters**, v. 38, n. 16, p. 892, 1977.
- [90] MUNSON, C. A.; GOTTFRIED, J. L.; DE LUCIA, F. C.; MCNESBY, K. L.; MIZIOLEK, A. W. Laser-based detection methods of explosives. **Counter terrorist Detection Techniques of Explosives**. p.279–321, 2007.
- [91] PATEL, C. K. N. Continuous-wave laser action on vibrational-rotational transitions of CO₂. **Physical review**, v. 136, n. 5A, p. A1187, 1964.
- [92] CO₂ Lasers: The industrial workhorse. Available in: https://www.photonics.com/Articles/COSUB2_SUB_Lasers_The_Industrial_Workhorse/a25155.
- [93] ZHANG, Y.; KILLEEN, T. Gas Lasers: CO₂ Lasers—progressing from a varied past to an application-specific future. **Laser Focus World**, v. 4, 2016.
- [94] EL-KADY, M. F.; KANER, R. B. Scalable fabrication of high-power graphene micro-supercapacitors for flexible and on-chip energy storage. **Nature Communications**, v. 4, p. 1475–1479, 2013.
- [95] YE, R.; JAMES, D. K.; TOUR, J. M. Laser-induced graphene: From discovery to translation. **Advanced Materials**, v. 31, n. 1, p. 1803621, 2019.

- [96] LIN, J.; PENG, Z.; LIU, Y.; et al. Laser-induced porous graphene films from commercial polymers. **Nature Communications**, v. 5, n. 1, p. 5–12, 2014.
- [97] SAMOUCO, A.; MARQUES, A. C.; PIMENTEL, A.; MARTINS, R.; FORTUNATO, E. Laser induced electrodes towards low-cost flexible UV ZnO sensors. **Flexible and Printed Electronics**, v. 3, n. 4, p. 044002, 2018.
- [98] SINGH, SWATANTRA P; LI, Y.; BE, A.; et al. Laser-induced graphene layers and electrodes prevents microbial fouling and exerts antimicrobial action. **ACS Applied Materials & Interfaces**, v. 9, n. 21, p. 18238–18247, 2017.
- [99] RATHINAM, K.; SINGH, S. P.; LI, Y.; et al. Polyimide derived laser-induced graphene as adsorbent for cationic and anionic dyes. **Carbon**, v. 124, p. 515–524, 2017.
- [100] WU, A. D.; DENG, L.; MEI, X.; et al. Direct-write graphene resistors on aromatic polyimide for transparent heating glass. **Sensors & Actuators: A. Physical**, v. 267, p. 327–333, 2017.
- [101] LUO, S.; HOANG, P. T.; LIU, T. Direct laser writing for creating porous graphitic structures and their use for flexible and highly sensitive sensor and sensor arrays. **Carbon**, v. 96, p. 522–531, 2015
- [102] SINGH, S. P.; RAMANAN, S.; KAUFMAN, Y.; ARNUSCH, C. J. Laser-induced graphene biofilm inhibition: texture does matter. **ACS Applied Nano Materials**, v. 1, n. 4, p. 1713–1720, 2018.
- [103] SINGH, SWATANTRA PRATAP; LI, Y.; ZHANG, J.; TOUR, J. M.; ARNUSCH, C. J. Sulfur-doped laser-induced porous graphene derived from polysulfone-class polymers and membranes. **ACS Nano**, v. 12, n. 1, p. 289–297, 2017.
- [104] YE, R.; JAMES, D. K.; TOUR, J. M. Laser-induced graphene. **Accounts of Chemical Research**, v. 51, n. 7, p. 1609–1620, 2018.
- [105] LEE, S.; JEON, S. Laser-induced graphitization of cellulose nanofiber substrates under ambient conditions. **ACS Sustainable Chemistry & Engineering**, v. 7, n. 2, p. 2270–2275, 2018.

- [106] CHYAN, Y.; YE, R.; LI, Y.; et al. Laser-induced graphene by multiple lasing: toward electronics on cloth, paper and food. **ACS Nano**, v. 12, n. 3, p. 2176–2183, 2018.
- [107] LEE, M. E.; ARMANI, A. M. Flexible UV exposure sensor based on UV responsive polymer. **ACS Sensors**, v. 1, n. 10, p. 1251–1255, 2016.
- [108] JACOBS, C. B.; MA, A. B.; MUCKLEY, E. S.; et al. UV-activated ZnO films on a flexible substrate for room temperature O₂ and H₂O sensing. **Scientific Reports**, v. 7, p. 6053, 2017.
- [109] TANG, X.; TIAN, M.; QU, L.; et al. Functionalization of cotton fabric with graphene oxide nanosheet and polyaniline for conductive and UV blocking properties. **Synthetic Metals**, v. 202, p. 82–88, 2015.
- [110] FRAGA, M. A.; FURLAN, H.; PESSOA, R. S.; MASSI, M. Wide bandgap semiconductor thin films for piezoelectric and piezoresistive MEMS sensors applied at high temperatures: an overview. **Microsystem Technologies**, v. 20, n. 1, p. 9–21, 2014.
- [111] YOU, J.; MENG, L.; SONG, T.; et al. Improved air stability of perovskite solar cells via solution-processed metal oxide transport layers. **Nature Nanotechnology**, v. 11, n. 1, p. 75–81, 2015.
- [112] WILLANDER, M.; KHUN, K.; IBUPOTO, Z. H. ZnO based potentiometric and amperometric nanosensors. **Journal of Nanoscience and Nanotechnology**, v. 14, n. 9, p. 6497–6508, 2014.
- [113] WEI, A.; PAN, L.; HUANG, W. Recent progress in the ZnO nanostructure-based sensors. **Materials Science & Engineering B**, v. 176, n. 18, p. 1409–1421, 2011.
- [114] PIMENTEL, A.; NUNES, D.; DUARTE, P.; et al. Synthesis of long ZnO nanorods under microwave irradiation or conventional heating. **The Journal of Physical Chemistry C**, v. 118, n. 26, p. 14629–14639, 2014.
- [115] FORTUNATO, E.; GONÇALVES, A.; PIMENTEL, A.; et al. Zinc oxide, a multifunctional material: from material to device applications. **Applied Physics A**, v. 96, n. 1, p. 197–205, 2009.

- [116] PIMENTEL, A.; FERREIRA, S. H.; NUNES, D.; et al. Microwave synthesized ZnO nanorod arrays for UV sensors: a seed layer annealing temperature study. **Materials**, v. 9, n. 4, 2016.
- [117] PIMENTEL, A.; SAMOUCO, A.; NUNES, D.; et al. Ultra-fast microwave synthesis of ZnO nanorods on cellulose substrates for UV sensor applications. **Materials**, v. 10, n. 11, p. 1308, 2017.
- [118] ZHAI, T.; FANG, X.; LIAO, M.; et al. A comprehensive review of one-dimensional metal-oxide nanostructure photodetectors. **Sensors**, v. 9, n. 8, p. 6504–6529, 2009.
- [119] SANG, L.; LIAO, M.; SUMIYA, M. A comprehensive review of semiconductor ultraviolet photodetectors: from thin film to one-dimensional nanostructures. **Sensors**, v. 13, n. 8, p. 10482–10518, 2013.
- [120] CAMMI, D.; RONNING, C. Persistent photoconductivity in ZnO nanowires in different atmospheres. **Advances in Condensed Matter Physics**, v. 2014, p. 2–7, 2014.
- [121] TAKAHASHI, Y. et al. Photoconductivity of ultrathin zinc oxide films. **Japanese Journal of Applied Physics**, v. 33, n. 12R, p. 6611, 1994.
- [122] PAHARI, A. K.; DUBEY, B. K. **Waste From Electrical and Electronics Equipment**. Elsevier Inc., 2019.
- [123] İŞILDAR, A.; RENE, E. R.; VAN HULLEBUSCH, E. D.; LENS, P. N. Electronic waste as a secondary source of critical metals: management and recovery technologies. **Resources, Conservation and Recycling**, v. 135, p. 296–312, 2018.
- [124] ZHU, H.; LUO, W.; CIESIELSKI, P. N.; et al. Wood-derived materials for green electronics, biological devices, and energy applications. **Chemical Reviews**, v. 116, n. 16, p. 9305–9374, 2016.
- [125] XU, W.; WANG, H.; YE, L.; XU, J. The role of solution-processed high-k gate dielectrics in electrical performance of oxide thin-film transistors. **Journal of Materials Chemistry C**, v. 2, n. 27, p. 5389–5396, 2014.
- [126] IHALAINEN, P.; MÄÄTTÄNEN, A.; JÄRNSTRÖM, J.; et al. Influence of surface properties of coated papers on printed electronics. **Industrial & Engineering Chemistry Research**, v. 51, n. 17, p. 6025–6036, 2012.

- [127] NOLAN, K. E.; GUIBENE, W.; KELLY, M. Y. An evaluation of low power wide area network technologies for the internet of things. **2016 International Wireless Communications and Mobile Computing Conference (IWCMC)**, p. 439–444, 2016.
- [128] AL-SARAWI, S.; ANBAR, M.; ALIEYAN, K.; ALZUBAIDI, M. Internet of Things (IoT) communication protocols: review. **2017 8th International Conference on Information Technology (ICIT)**, p. 685–690, 2017.
- [129] DAI, S.; CHU, Y.; LIU, D.; et al. Intrinsically ionic conductive cellulose nanopapers applied as all solid dielectrics for low voltage organic transistors. **Nature Communications**, v. 9, n. 1, p. 1–10, 2018.
- [130] GAO, M.; LI, L.; SONG, Y. Inkjet printing wearable electronic devices. **Journal of Materials Chemistry C**, v. 5, n. 12, p. 2971–2993, 2017.
- [131] HU, G. H.; FENG, L. F. Extruder processing for nanoblends and nanocomposites. **Macromolecular Symposia**, v. 8, p. 303–308, 2003.
- [132] SHARMA, S.; NAIR, S. S.; ZHANG, Z.; RAGAUSKAS, A. J.; DENG, Y. Characterization of micro fibrillation process of cellulose and mercerized cellulose pulp. **RSC Advances**, v. 5, n. 77, p. 63111–63122, 2015.
- [133] NELSON, K.; RETSINA, T.; IAKOVLEV, M.; et al. American process: production of low cost nanocellulose for renewable. **Advanced Materials Applications**, p.267–302, 2016.
- [134] HOFMANN, E.; KRÜGER, K.; HAYNL, C.; et al. Microfluidic nozzle device for ultrafine fiber solution blow spinning with precise diameter control. **Lab on a Chip**, v. 18, n. 15, p. 2225–2234, 2018.
- [135] PASCHOALIN, R. T.; TRALDI, B.; AYDIN, G.; et al. Solution blow spinning fibres: New immunologically inert substrates for the analysis of cell adhesion and motility. **Acta Biomaterialia**, v. 51, p. 161–174, 2017.
- [136] PARIZE, D. D. DA S.; OLIVEIRA, J. E. DE; WILLIAMS, T.; et al. Solution blow spun nanocomposites of poly(lactic acid)/cellulose nanocrystals from eucalyptus Kraft pulp. **Carbohydrate Polymers**, v. 174, p. 923–932, 2017

- [137] MERCANTE, L. A.; SANFELICE, R. C.; CORREA, D. S.; et al. Solution blow spun PMMA nanofibers wrapped with reduced graphene oxide as an efficient dye adsorbent. **New Journal of Chemistry**, v. 41, n. 17, p. 9087–9094, 2017.
- [138] CHEN, C.; TOWNSEND, A. D.; SELL, S. A.; MARTIN, R. S. Microchip-based 3D-cell culture using polymer nanofibers generated by solution blow spinning. **Analytical Methods**, v. 9, n. 22, p. 3274–3283, 2017.
- [139] GAO, Y.; XIANG, H. F.; WANG, X. X.; et al. A portable solution blow spinning device for minimally invasive surgery hemostasis. **Chemical Engineering Journal**, v. 387, p. 124052, 2020.
- [140] DADOL, G. C.; LIM, K. J. A.; CABATINGAN, K. L.; TAN, N. P. B. Solution blow spinning (SBS)–polyacrylonitrile (PAN)–assisted cellulose acetate nanofiber membrane. **Nanotechnology**, v. 31, p. 345602, 2018.
- [141] BAPTISTA, A. C.; MARTINS, J. I.; FORTUNATO, E.; MARTINS, R.; BORGES, J. P.; FERREIRA, I. Thin and flexible bio-batteries made of electrospun cellulose-based membranes. **Biosens. Bioelectron**, v. 26, p. 2742–2745 2011.
- [142] KONWARH, R.; KARAK, N.; MISRA, M. Electrospun cellulose acetate nanofibers: The present status and gamut of biotechnological applications. **Biotechnology Advances**, v. 31, n. 4, p. 421–437, 2013.
- [143] CHRISTOFOROU, T.; DOUMANIDIS, C. Biodegradable cellulose acetate nanofiber fabrication via electrospinning. **Journal of Nanoscience and Nanotechnology**, v. 10, n. 9, p. 6226–6233, 2010.
- [144] ROJANARATA, T.; PLIANWONG, S.; SU-UTA, K.; OPANASOPIT, P.; NGAWHIRUNPAT, T. Electrospun cellulose acetate nanofibers as thin layer chromatographic media for eco-friendly screening of steroids adulterated in traditional medicine and nutraceutical products. **Talanta**, v. 115, p. 208–213, 2013.
- [145] WU, S.; QIN, X.; LI, M. The structure and properties of cellulose acetate materials: A comparative study on electrospun membranes and casted films. **Journal of Industrial Textiles**, v. 44, n. 1, p. 85–98, 2014.

- [146] ZHIJIANG, C.; YI, X.; HAIZHENG, Y.; JIA, J.; LIU, Y. Poly(hydroxybutyrate)/cellulose acetate blend nanofiber scaffolds: Preparation, characterization and cytocompatibility. **Materials Science and Engineering C**, v. 58, p. 757–767, 2016.
- [147] CHEN, S.; SCHUENEMAN, G.; PIPES, R. B.; YOUNGBLOOD, J.; MOON, R. J. Effects of crystal orientation on cellulose nanocrystals-cellulose acetate nanocomposite fibers prepared by dry spinning. **Biomacromolecules**, v. 15, n. 10, p. 3827–3835, 2014.
- [148] TANG, D.; ZHUANG, X.; ZHANG, C.; CHENG, B.; LI, X. Generation of nanofibers via electrostatic-Induction-assisted solution blow spinning. **Journal of Applied Polymer Science**, v. 132, n. 31, p. 1–8, 2015.
- [149] MA, Z.; KOTAKI, M.; RAMAKRISHNA, S. Electrospun cellulose nanofiber as affinity membrane. **Journal of Membrane Science**, v. 265, n. 1–2, p. 115–123, 2005.
- [150] LAURENCIN, C.; KUMBAR, S.; NUKAVARAPU, S.; JAMES, R.; HOGAN, M. Recent patents on electrospun biomedical nanostructures: an overview. **Recent Patents on Biomedical Engineering**, v. 1, n. 1, p. 68–78, 2010.
- [151] YUDANOVA, T. N.; FILATOV, I. Y.; AFANASOV, I. M. Production of Ultrafine Cellulose Acetate Fibers. **Theoretical Foundations of Chemical Engineering**, v. 50, n. 4, p. 508–512, 2016.
- [152] LEI, T.; GUAN, M.; LIU, J.; et al. Biocompatible and totally disintegrable semiconducting polymer for ultrathin and ultralightweight transient electronics. **Proceedings of the National Academy of Sciences**, v. 114, n. 20, p. 5107–5112, 2017.
- [153] YOU, R.; LIU, Y. Q.; HAO, Y. L.; et al. Laser fabrication of graphene-based flexible electronics. **Advanced Materials**, v. 32, n. 15, p. 1–22, 2020.
- [154] WANG, F.; WANG, K.; ZHENG, B.; et al. Laser-induced graphene: preparation, functionalization and applications. **Materials Technology**, v. 33, n. 55, p. 340–356, 2018.

- [155] CLERICI, F.; FONTANA, M.; BIANCO, S.; et al. In situ MoS₂-decoration of laser induced graphene as flexible supercapacitor electrodes. **ACS Applied Materials & Interfaces**, v. 8, n. 16, p. 10459- 10465., 2016.
- [156] ZHANG, Z.; SONG, M.; HAO, J.; et al. Visible light laser-induced graphene from phenolic resin: A new approach for directly writing graphene-based electrochemical devices on various substrates. **Carbon**, v. 127, p. 287–296, 2018.
- [157] SONG, W.; ZHU, J.; GAN, B.; et al. Flexible, stretchable, and transparent planar microsupercapacitors based on 3D porous laser-induced graphene. **Small**, v. 14, n. 1, p. 1702249, 2017.
- [158] LI, X.; CUI, Y.; QI, M.; et al. A 1000-Volt planar micro-supercapacitor by direct-write laser engraving of polymers. **2017 IEEE 30th International Conference on Micro Electro Mechanical Systems (MEMS)**, p.821–824, 2017.
- [159] YE, R.; LI, Y.; KITTRELL, C.; et al. Laser-induced graphene formation on wood. **Advanced Materials**, v. 29, n. 37, p. 1702211, 2017.
- [160] YE, R.; PENG, Z.; WANG, T.; et al. In situ formation of metal oxide nanocrystals embedded in laser-induced. **ACS Nano**, v. 9, n. 9, p. 9244–9251, 2015.
- [161] TAN, K. W.; JUNG, B.; WERNER, J. G.; et al. Transient laser heating induced hierarchical porous structures from block copolymer – directed self-assembly. **Science**, v. 349, n. 6243, p. 54–59, 2015.
- [162] KARAKURT, I.; ELWOOD, J.; LI, X.; et al. Membraneless microfluidic redox battery for wearable electronics applications. **2017 19th International Conference on Solid-State Sensors, Actuators and Microsystems**, p.1820–1823, 2017.
- [163] HOMSY, A.; KOSTER, S.; EIJKEL, J. C. T.; et al. A high current density DC magnetohydrodynamic (MHD) micropump. **Lab on a Chip**, v. 5, n. 4, p. 466–471, 2005.
- [164] AN, J.; LE, T. S. D.; LIM, C. H. J.; et al. Single-step selective laser writing of flexible photodetectors for wearable optoelectronics. **Advanced Science**, v. 5, n. 8, p. 1–9, 2018.

- [165] MARQUES, A. C.; CARDOSO, A. R.; MARTINS, R.; SALES, M. G. F.; FORTUNATO, E. Laser-induced graphene-based platforms for dual biorecognition of molecules. **ACS Applied Nano Materials**, v. 3, n. 3, p. 2795–2803, 2020.
- [166] CARDOSO, A. R.; MARQUES, A. C.; SANTOS, L.; et al. Molecularly-imprinted chloramphenicol sensor with laser-induced graphene electrodes. **Biosensors and Bioelectronics**, v. 124, p. 167–175, 2019.
- [167] RAHIMI, R.; OCHOA, M.; YU, W.; ZIAIE, B. Highly stretchable and sensitive unidirectional strain sensor via laser carbonization. **ACS applied materials & interfaces**, v. 7, n. 8, p. 4463–4470, 2015.
- [168] FENZL, C.; NAYAK, P.; HIRSCH, T.; et al. Laser-scribed graphene electrodes for aptamer-based biosensing. **ACS Sensors**, v. 2, n. 5, p. 616–620, 2017.
- [169] TAO, L.; TIAN, H.; LIU, Y.; et al. An intelligent artificial throat with sound-sensing ability based on laser induced graphene. **Nature Communications**, v. 8, n. 1, p. 1–8, 2017.
- [170] ZHANG, CHENG; XIE, Y.; DENG, H.; et al. Monolithic and flexible ZnS / SnO₂ ultraviolet photodetectors with lateral graphene electrodes. **Small**, v. 13, n. 18, p. 1604197, 2017.
- [171] TAO, L.; LIU, Y.; JU, Z.; et al. A flexible 360-degree thermal sound source based on laser induced graphene. **Nanomaterials**, v. 6, n. 6, p. 112, 2016.
- [172] NAG, A.; MUKHOPADHYAY, S. C.; KOSEL, J. Sensing system for salinity testing using laser-induced graphene sensors. **Sensors & Actuators: A. Physical**, v. 264, p. 107-116, 2017.
- [173] REYNOLDS, M.; DUARTE, L. M.; COLTRO, W. K. T.; et al. Laser-engraved ammonia sensor integrating a natural deep eutectic solvent. **Microchemical Journal**, v. 157, p. 105067, 2020.
- [174] CARVALHO, A. F.; FERNANDES, A. J. S.; LEITÃO, C.; et al. Laser-Induced graphene strain sensors produced by ultraviolet irradiation of polyimide. **Advanced Functional Materials**, v. 28, n. 52, p. 1–8, 2018.

- [175] FIGUEIRA, J.; GASPAR, C.; CARVALHO, J. T.; et al. Sustainable fully printed UV sensors on cork using zinc oxide/ethylcellulose inks. **Micromachines**, v. 10, n. 9, p. 601, 2019.
- [176] WANG, Z. L.; XU, D.; WANG, H. G.; WU, Z.; ZHANG, X. B. In situ fabrication of porous graphene electrodes for high-performance. **ACS Nano**, v. 7, n. 3, p. 2422- 2430., 2013.
- [177] JIANG, L.; FAN, Z. Design of advanced porous graphene materials: from graphene nanomesh to 3D architectures. **Nanoscale**, v. 6, n. 4, p. 1922–1945, 2014.
- [178] GHORANI, B.; RUSSELL, S. J.; GOSWAMI, P. Controlled morphology and mechanical characterisation of electrospun cellulose acetate fibre webs. **International Journal of Polymer Science**, v. 2013 2013.
- [179] SEGAL, L.; CREELY, J. J.; MARTIN, A. E. J.; CONRAD, M. Empirical method for estimating the degree of crystallinity of native cellulose using the X-ray diffractometer. **Textile Research Journal**, v. 29, n. 10, p. 786–794, 1958.
- [180] SAITO, T.; KIMURA, S.; NISHIYAMA, Y.; ISOGAI, A. Cellulose nanofibers prepared by TEMPO-mediated oxidation of native cellulose. **Biomacromolecules**, v. 8, n. 8, p. 2485–2491, 2007.
- [181] VINAYAN, B. P.; NAGAR, R.; RAMAN, V.; et al. Synthesis of graphene-multiwalled carbon nanotubes hybrid nanostructure by strengthened electrostatic interaction and its lithium ion battery application. **Journal of Materials Chemistry**, v. 22, n. 19, p. 9949–9956, 2012.
- [182] DIMIEV, A. M.; CERIOTTI, G.; BEHABTU, N.; et al. Direct real-time monitoring of stage transitions in graphite intercalation compounds. **ACS Nano**, v. 7, n. 3, p. 2773–2780, 2013.
- [183] ZHANG, B.; SONG, J.; YANG, G.; HAN, B. Large-scale production of high-quality graphene using glucose and ferric chloride. **Chemical Science**, v. 5, n. 12, p. 4656–4660, 2014.
- [184] REINA, A.; JIA, X.; HO, J.; et al. Large area, few-layer graphene films on arbitrary substrates by chemical vapor deposition. **Nano letters**, v. 9, n. 1, p. 30–35, 2008.

- [185] JUN, J. H.; SEONG, H.; CHO, K.; MOON, B.; KIM, S. Ultraviolet photodetectors based on ZnO nanoparticles. **Ceramics International**, v. 35, p. 2797–2801, 2009.
- [186] CHEN, Z.; MO, X.; HE, C.; WANG, H. Intermolecular interactions in electrospun collagen – chitosan complex nanofibers. **Carbohydrate Polymers**, v. 72, p. 410–418, 2008.
- [187] BIRD, ROBERT BYRON; ARMSTRONG, ROBERT C.; HASSAGER, O. **Dynamics of Polymeric Liquids. Vol. 1: Fluid Mechanics**. Wiley, 1987.
- [188] DARISTOTLE, J. L.; BEHRENS, A. M.; SANDLER, A. D.; KOFINAS, P. A review of the fundamental principles and applications of solution blow spinning. **ACS Applied Materials & Interfaces**, v. 8, n. 51, p. 34951–34963, 2016.
- [189] DOSHI, J.; RENEKER, D. H. Electrospinning process and applications of electrospun fibers. **Conference Record of the 1993 IEEE Industry Applications Conference Twenty-Eighth IAS Annual Meeting**, v. 35, p. 151–160, 1995.
- [190] MCKEE, M. G.; ELKINS, C. L.; LONG, T. E. Influence of self-complementary hydrogen bonding on solution rheology/electrospinning relationships. **Polymer**, v. 45, p. 8705–8715, 2004.
- [191] YARIN, A. L.; POURDEYHIMI, B.; RAMAKRISHNA, S. **Fundamentals and Applications of Micro- and Nanofibers**. Cambridge University Press, 2014.
- [192] DUARTE, M. L.; FERREIRA, M. C.; MAR, M. R. An optimised method to determine the degree of acetylation of chitin and chitosan by FTIR spectroscopy. **Biological Molecular**, v. 31, p. 1–8, 2002.
- [193] WYATT, T. P.; CHIEN, A.; KUMAR, S.; YAO, D. Development of a gel spinning process for high-strength poly(ethylene oxide) fibers. **Polymer Engineering & Science**, v. 54, n. 12, p. 2839–2847, 2014.
- [194] CONCEIÇÃO, M.; LUCENA, C.; ALENCAR, A. E. V. DE; MAZZETO, S. E.; SOARES, S. D. A. The effect of additives on the thermal degradation of cellulose acetate. **Polymer Degradation and Stability**, v. 80, n. 1, p. 149–155, 2003.

- [195] FRENCH, A. D. Idealized powder diffraction patterns for cellulose polymorphs. **Cellulose**, v. 21, n. 2, p. 885–896, 2014.
- [196] CHEN, H.; WANG, N.; LIU, L. Regenerated cellulose membrane prepared with ionic liquid 1-butyl-3-methylimidazolium chloride as solvent using wheat straw. **Journal of Chemical Technology & Biotechnology**, v. 87, n. 12, p. 1634–1640, 2012.
- [197] KJELLANDER, R.; FLORIN, E. Water structure and changes in thermal stability of the system poly (ethylene oxide)-water. **Journal of the Chemical Society, Faraday Transactions 1: Physical Chemistry in Condensed Phases**, v. 77, n. 9, p. 2053–2077, 1981.
- [198] MCCORMICK, C. L.; CALLAIS, P. A.; HUTCHINSON, B. H. Solution studies of cellulose in lithium chloride and n,n-dimethylacetamide. **Macromolecules**, v. 18, n. 12, p. 2394–2401, 1985.
- [199] ZHENG, Z.; JIANG, J.; GUO, J.; SUN, J.; YANG, J. Chitosan-gated low-voltage transparent indium-free aluminum-doped zinc oxide thin-film transistors. **Organic Electronics**, v. 33, p. 311–315, 2016.
- [200] SANTOS, L.; NUNES, D.; CALMEIRO, T.; et al. Solvothermal synthesis of gallium-indium-zinc-oxide nanoparticles for electrolyte-gated transistors. **ACS Applied Materials and Interfaces**, v. 7, n. 1, p. 638–646, 2015.
- [201] DOU, W.; QIANG ZHU, L.; JIANG, J.; WAN, Q. Flexible protonic/electronic coupled neuron transistors self-assembled on paper substrates for logic applications. **Applied Physics Letters**, v. 102, n. 9, p. 093509, 2013.
- [202] DASGUPTA, S.; STOESSER, G.; SCHWEIKERT, N.; et al. Printed and electrochemically gated, high-mobility, inorganic oxide nanoparticle FETs and their suitability for high-frequency applications. **Advanced Functional Materials**, v. 22, n. 23, p. 4909–4919, 2012.
- [203] YANG, J.; GE, C.; DU, J.; et al. Artificial synapses emulated by an electrolyte-gated tungsten-oxide transistor. **Advanced Materials**, v. 30, n. 34, p. 1801548, 2018.

- [204] INUI, T.; KOGA, H.; NOGI, M.; KOMODA, N.; SUGANUMA, K. High-dielectric paper composite consisting of cellulose nanofiber and silver nanowire. **14th IEEE international conference on nanotechnology**, p. 470–473, 2014.
- [205] MÜNZENRIEDER, N.; PETTI, L.; ZYSSET, C.; et al. Investigation of gate material ductility enables flexible a-IGZO TFTs bendable to a radius of 1.7 mm. **2013 Proceedings of the European Solid-State Device Research Conference (ESSDERC)**, p. 362–365, 2013.
- [206] PARK, S.; LEE, S.; KIM, C.; et al. Sub-0.5 V highly stable aqueous salt gated metal oxide electronics. **Nature Publishing Group**, v. 5, p. 13088, 2015.
- [207] VIDANO, R. P.; FISHBACH, D. B.; WILLIS, L. J.; LOEHR, T. M. Observation of Raman band shifting with excitation wavelength for carbons and graphites. **Solid State Communications**, v. 39, n. 2, p. 341–344, 1981.
- [208] MUHAMMAD HAFIZ, S.; RITIKOS, R.; WHITCHER, T. J.; et al. A practical carbon dioxide gas sensor using room-temperature hydrogen plasma reduced graphene oxide. **Sensors and Actuators, B: Chemical**, v. 193, p. 692–700, 2014.
- [209] CANÇADO, L. G.; TAKAI, K.; ENOKI, T.; et al. General equation for the determination of the crystallite size L_a of nanographite by Raman spectroscopy. **Applied Physics Letters**, v. 88, n. 16, p. 163106, 2006.
- [210] YE, R.; XIANG, C.; LIN, J.; et al. Coal as an abundant source of graphene quantum dots. **Nature Communications**, v. 4, n. 1, p. 2–7, 2013.
- [211] SUN, Z.; RAJI, A. R. O.; ZHU, Y.; et al. Large-area bernal-stacked bi-, tri-, and tetralayer graphene. **ACS Nano**, v. 6, n. 11, p. 9790–9796, 2012.
- [212] PENG, Z.; YE, R.; MANN, J. A.; et al. Flexible boron-doped laser induced graphene microsupercapacitors. **ACS Nano**, v. 9, n. 6, p. 5868–5875, 2015.
- [213] XU, X.; CHEN, J.; CAI, S.; et al. A real-time wearable UV-radiation monitor based on a high-performance p-CuZnS/n-TiO₂ photodetector. **Advanced Materials**, v. 30, n. 43, p. 1803165, 2018.

APPENDIX A

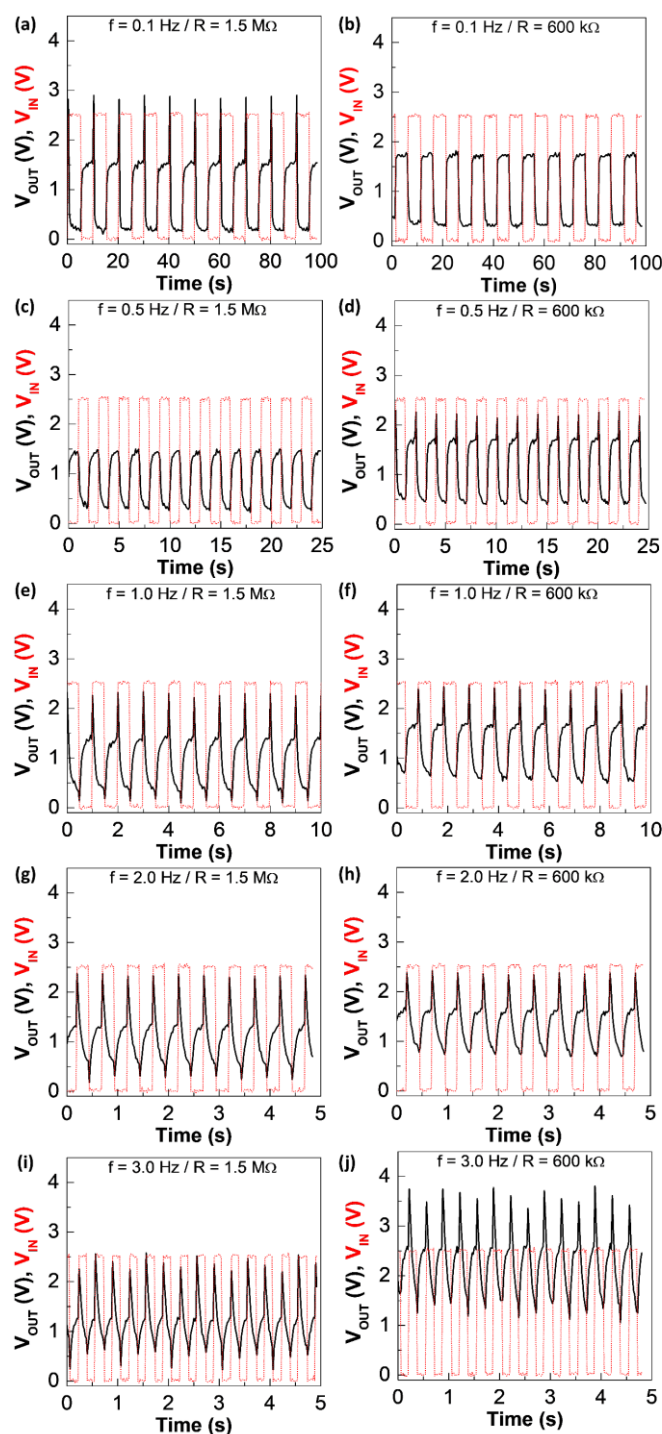


Figure A.1 - Dynamic response of the ICCM inverter, varying the frequency and resistance: (a) $f = 0.1 \text{ Hz} / R = 1.5 \text{ M}\Omega$; (b) $f = 0.1 \text{ Hz} / R = 600 \text{ k}\Omega$; (c) $f = 0.5 \text{ Hz} / R = 1.5 \text{ M}\Omega$; (d) $f = 0.5 \text{ Hz} / R = 600 \text{ k}\Omega$; (e) $f = 1.0 \text{ Hz} / R = 1.5 \text{ M}\Omega$; (f) $f = 1.0 \text{ Hz} / R = 600 \text{ k}\Omega$; (g) $f = 2.0 \text{ Hz} / R = 1.5 \text{ M}\Omega$; (h) $f = 2.0 \text{ Hz} / R = 600 \text{ k}\Omega$; (i) $f = 3.0 \text{ Hz} / R = 1.5 \text{ M}\Omega$ and (j) $f = 3.0 \text{ Hz} / R = 600 \text{ k}\Omega$.

APPENDIX B

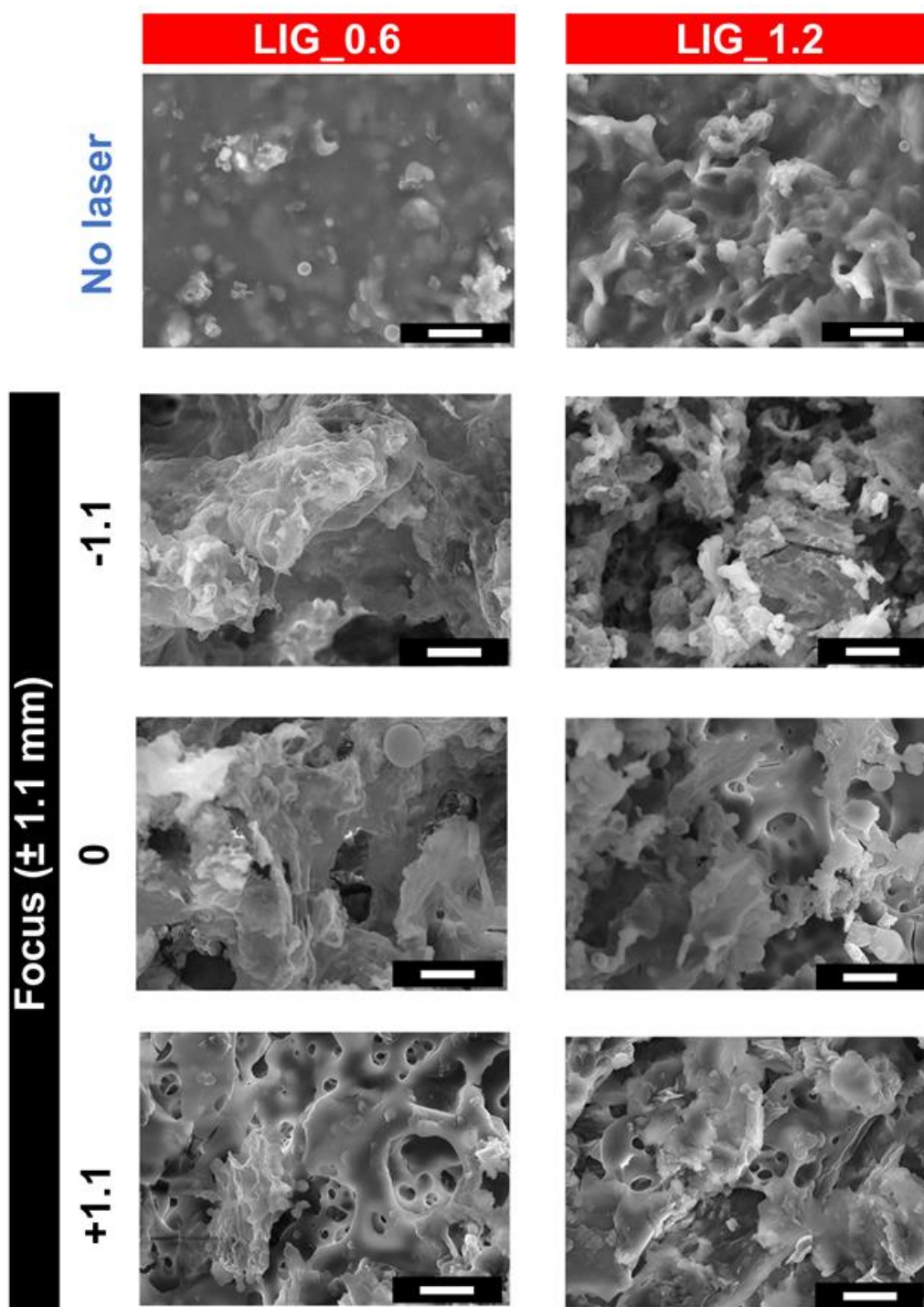


Figure B.1 - Photomicrographs of CMC-based ink microstructure formulated with LIG from CNC (LIG_0.6 and LIG_1.2) before and after laser passing, varying laser focus at 8.2 cm/s laser speed and 2.4 W laser power (white scale bar of 15 μ m).